NASA CR - 134905

15 CM MERCURY ION THRUSTER RESEARCH - 1975

PREPARED FOR

LEWIS RESEARCH CENTER

NATIONAL AERONAUTICS AND SPACE ADMINISTRATION

GRANT NGR-06-002-112

Annual Report

December 1975

Paul J. Wilbur
Department of Mechanical Engineering
Colorado State University
Fort Collins, Colorado

1. Report No.	2. Government Accession No.	3. Recipient's Catalog No.
NASA CR-134905		

4. Title and Subtitle	5. Report Date
15 CM MERCURY ION THRUSTER RESEARCH - 1975	December 1975
	6. Performing Organization Code
7. Author(s)	8. Performing Organization Report No.
Paul J. Wilbur	
9. Performing Organization Name and Address	10. Work Unit No.
Department of Mechanical Engineering Colorado State University Fort Collins, Colorado 80523	11. Contract or Grant No.
	NGR-06-002-112
12. Sponsoring Agency Name and Address	13. Type of Report and Period Covered
National Aeronautics and Space Administration Washington, D. C. 20546	Dec. 1, 1974 - Dec. 1, 1975
	14. Sponsoring Agency Code

15. Supplementary Notes

Grant Monitor, William Kerslake
Spacecraft Technology Div.
NASA Lewis Research Center
Cleveland, Ohio 44135

16. Abstract

Doubly charged ion current measurements in the beam of a SERT II thruster are shown to introduce corrections which bring its calculated thrust into close agreement with that measured during flight testing. A theoretical model of doubly charged ion production and loss in mercury electron bombardment thrusters is discussed and is shown to yield doubly-to-singly charged ion density ratios that agree with experimental measurements obtained on a 15 cm diameter thruster over a range of operating conditions. Single cusp magnetic field thruster operation is discussed and measured ion beam profiles, performance data, doubly charged ion densities, and discharge plasma characteristics are presented for a range of operating conditions and thruster geometries. Variations in the characteristics of this thruster are compared to those observed in the divergent field thruster and the cusped field thruster is shown to yield flatter ion beam profiles at about the same discharge power and propellant utilization operating point. An ion optics test program is described and the measured effects of grid system dimensions on ion beamlet half angle and diameter are examined. Results are compared to published theoretical data. Hollow cathode startup using a thermionically emitting filament within the cathode is shown to be an effective means of achieving rapid startup. The effectiveness of this approach is examined over a range of mercury flow rates and compared to results obtained with a high voltage tickler startup technique. Photographs and temperature measurements of the interior of an operating cathode taken over a period of time when the cathode is being depleted of low work function emissive mix are presented. Results of cathode plasma property measurement tests conducted within the cathode are presented.

17. Key Words (Suggested by Author(s))	18. Distribution Statement
Electrostatic Thruster Hollow Cathode	Unclassified - Unlimited

19. Security Classif. (of this report)	20. Security Classif. (of this page)	21. No. of Pages	22. Price*
Unclassified	Unclassified	120	$3.00

* For sale by the National Technical Information Service, Springfield, Virginia 22161

NASA-C-168 (Rev. 10-75)

TABLE OF CONTENTS

SERT II THRUST CORRECTION FOR DOUBLY CHARGED IONS

Ralph R. Peters

The thrust of the SERT II thruster measured in space has been shown to be slightly less than that calculated from electrical measurements on the thruster.[1] Since the electrically based thrust was corrected for ion beam divergence one would expect this thrust difference to be due to doubly charged ions. In order to verify this postulate the ion beam of a SERT II thruster was probed using a mass spectrometer suitable for double and single ion discrimination and the thrust error due to the double ions present was determined.

Procedure

A SERT II thruster was installed within the Colorado State University vacuum test facility and operated at the design 100% thrust level. The thruster had been modified in that it had electromagnets and independent main and cathode flow systems, but these were controlled in such a way that in-flight operating data were reproduced to the extent indicated in Table I.

Table I - SERT II Operating Conditions

	In-flight	Current Test
Arc Current	1.7 A	1.7 A
Arc Voltage	37 V	37 V
Beam Current	253 mA	258 mA
Mass Flow Rate	313 mA	307 mA
Screen Voltage	3000 V	3000 V
Accel Voltage	-1500 V	-1500 V

While operating at the test conditions indicated the ion beam was probed with an E x B momentum analyzer[2] and the resultant data were analyzed in the manner described in Appendix A to obtain the double and single ion current contributions to the measured beam current.

Results and Conclusion

The double-to-single beam ion current ratio (I^{++}/I^{+}) determined for the SERT II thruster at the Table I operating conditions was 7.8%. The ratio of true thrust to that which would be calculated assuming only singly charged ions and operation at the measured beam current is given by:

$$\text{Double Ion Thrust Correction Factor} = \frac{\left(1 + \frac{I^{++}}{I^{+}\sqrt{2}}\right)}{\left(1 + I^{++}/I^{+}\right)} \qquad (1)$$

Substitution of the measured double-to-single current ratio into this expression yields a double ion thrust correction factor of 0.98. The SERT II thrust level as determined from miniature electrostatic accelerometer measurements in space was 27.4 mN ± 1%.[1] The thrust calculated from electrical measurements and corrected for ion beam divergence was 28.2 mN ± 2.2%.[1] Multiplying this calculated thrust by the double ion correction factor yields a thrust of 27.6 mN which agrees with the measured thrust to well within the accuracies involved.

DOUBLY CHARGED ION PRODUCTION IN ELECTRON BOMBARDMENT THRUSTERS

Ralph R. Peters

Doubly charged ions are generally considered an undesirable component of an electron bombardment thruster plasma because of the sputtering damage they cause. In order to select design and operating constraints which minimize doubly charged ion concentrations it is desirable to have an accurate model describing the mechanisms by which they are produced and lost. This work describes such a model and its verification through tests on the 15 cm diameter SERT II mercury ion thruster. Although this particular work is applicable to mercury discharges only, the procedure should apply equally well to other propellants.

Theoretical Model

The reactions which are considered important in the production and loss of ions in mercury, electron bombardment ion thrusters are illustrated in Figure 1. The symbols used in the figure represent the following species:

Hg^{o} - neutral ground state mercury

Hg^{m} - metastable neutral mercury (6^3P_0 and 6^3P_2 states)

Hg^{r} - resonance state mercury (6^1P_1 and 6^3P_1 states)

Hg^{+} - singly ionized ground state mercury

Hg^{m+} - singly ionized metastable mercury ($6^2D_{3/2}$ and $6^2D_{5/2}$ states)

Hg^{++} - doubly ionized ground state mercury

The arrows in Figure 1 indicate the various interaction routes considered in this analysis. They show for example that ground state singly charged ions can be produced from neutral ground state, resonance state, and metastable state atoms and that they can be lost as a result of single ion migration to the plasma boundary and production of metastable double

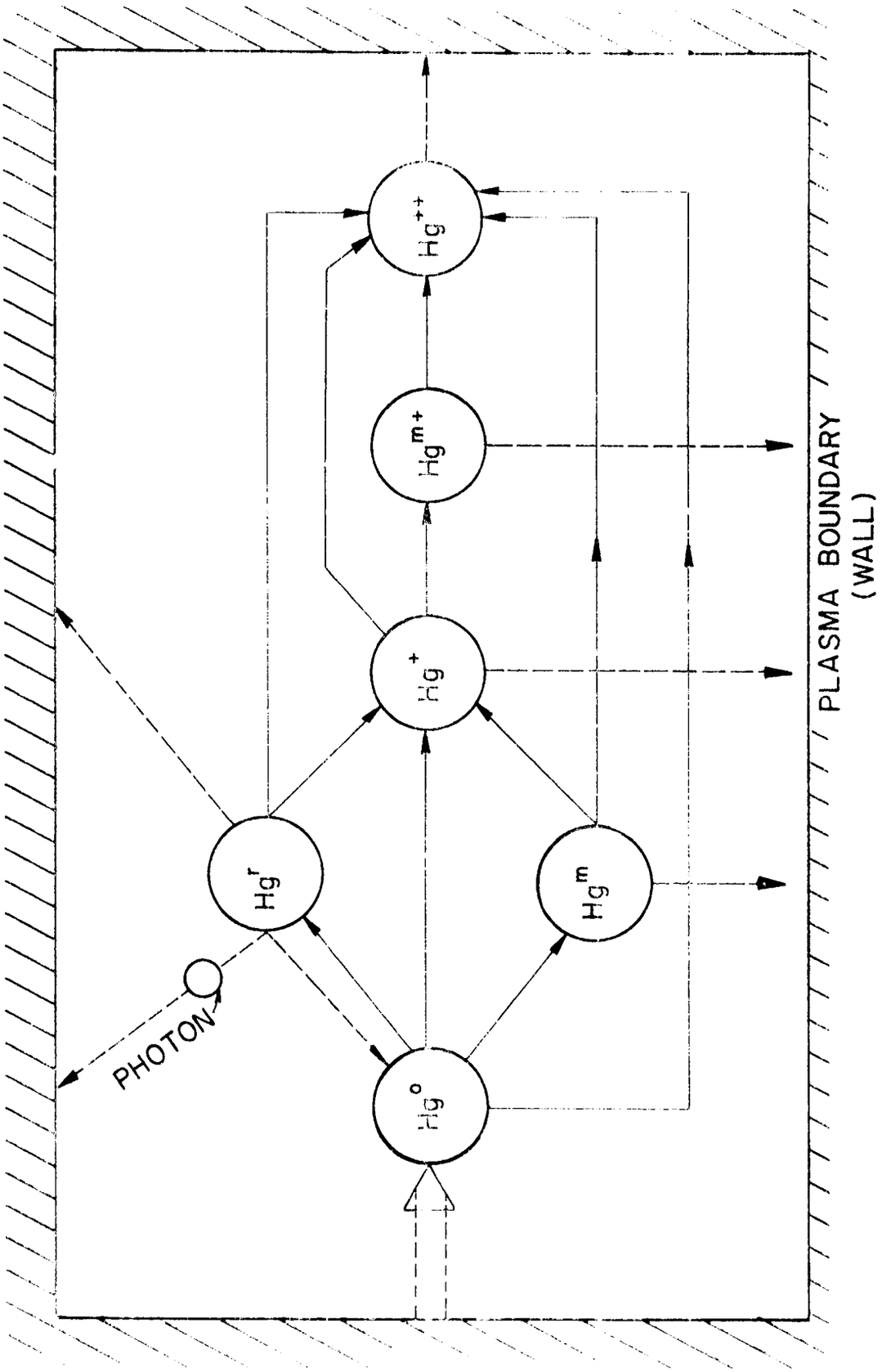

ION PRODUCTION AND LOSS SCHEMATIC

ions and double ions by electron bombardment. The intermediate resonance and metastable states used in the analysis were selected because they have significant electron impact cross sections of formation over the electron energy range of interest and sufficiently long effective lifetimes so that they can enter into ion production processes before they decay. In going to the plasma boundary an excited atom or an ion could be going to a discharge chamber wall where it would be neutralized and returned to the discharge as a neutral ground state atom or it could be going through a grid aperture in which case it would be extracted from the discharge region and replaced by a neutral atom from the propellant feed system. In either case this process represents a loss rate for any of the excited states. These losses to the boundary are indicated in Figure 1 by the dotted lines to the wall of the chamber and then a large arrow back to the neutral ground state. As suggested by Figure 1 resonance state atoms can also be lost by photon diffusion. These atoms have short lifetimes for spontaneous photon emission but the emitted photon is readily absorbed by an adjacent ground state atom thereby producing another resonance state atom. Since the transport time of the photon is small compared to the excited state lifetime the excited state can be considered to exist continuously. The photon can however eventually diffuse to a boundary where it will be lost. This is equivalent to the loss of a resonance state atom; a loss mechanism represented in Figure 1 by a dotted line conveying a photon to the wall and a branching line going from the resonance atom to the ground state atom.

The determination of the various specie densities requires the equating of production and loss rates for each specie in accordance with the above model and as outlined in Reference [3]. Where possible, cross sections for the reactions implied by Figure 1 were selected from published

experimental data.[4, 5, 6] If experimental cross sections were not available, theoretical cross sections were either obtained from the literature[7] or calculated using the Gryzinski approximation.[8] All reactions except those occurring at the plasma boundary were considered to be induced by electron bombardment. The bombarding electron group was assumed to consist of a Maxwellian component (defined by a density and temperature) and a monoenergetic or primary component (defined by a density and energy).

The model assumes electron induced reactions occur only within the primary electron region of the thruster defined by the surface of revolution of the critical field line and screen grid because of the higher electron energies and densities that exist in this region. Diffusion loss effects are on the other hand dependent on the conditions at the surface of this region. In order to obtain accurate results from this model it was necessary to input to the computer program appropriately weighted volume and surface area averaged electron properties. The equations used in the model are described in detail in Reference [3].

Procedures and Results

Verification of this theoretical model of double ion production and loss mechanisms requires essentially simultaneous measurement of the plasma properties within an operating thruster and the single and double ion content of the ion beam. These measurements were made on a SERT II thruster operating at three different arc voltage conditions and with two different sets of grids (SERT II and high perveance dished grids). The plasma properties were measured using the movable Langmuir probe and recording system described in Reference [9]. The associated Langmuir probe traces were collected with the probe at sixteen different points in the discharge chamber.

and the data were then analyzed using the numerical method described in Reference [10].

An E x B momentum analyzer was used to measure the total double and single ion currents in the beam in accordance with the procedure for data acquisition and analysis described in Appendix A. The integrated double-to-single ion current ratios obtained using this procedure are listed under the measured operating data section in Table I.

A typical set of plasma property profiles obtained with the standard SERT II grids and during operation at a 37V arc voltage is presented as Figure 2. Also identified is the critical field line determined from iron filings maps for this thruster. Volume and surface area averaging of these properties over the primary electron region defined by this field line yields the values designated as computer program input parameters in the second row of Table I. These measurement, analysis and averaging procedures were repeated for each grid and operating condition investigated. The resultant averaged plasma properties, which are listed in Table I together with the geometrical properties of the primary electron region and the grids were then used as input to the computer model which has been described. The densities of the ionic and excited atomic species considered in the analysis were computed, these densities were normalized with the total heavy particle density in the thruster and they are listed as calculated normalized densities in Table I. The results of Table I show for example that the thruster operating with flat grids at 37V arc voltage would be predicted to have 68% neutral ground state atoms, 18% neutral resonance state atoms, 6.8% singly charged ground state ions and 0.2% doubly charged ground state ions.

TABLE I

SERT II Thruster Operating with Mercury

		Flat Grids			Dished Grids		
Measured Thruster Parameters	Arc Current	4. A	4.7 A	5.05 A	3.87 A	4.06 A	4.13 A
	Arc Voltage	33 V	37. V	41.6 V	32.2 V	38. V	40.4 V
	Beam Current	.389 A	.456 A	.472 A	.499 A	.654 A	.6[illegible] A
	Mass Flow Rate	.318 A	.307 A	.305 A	.745 A	.725 A	.650 A
Derived Parameters	Measured Double-to-Single Ion Current Ratio (Thrust Correction Factor)	.024 (.99)	.073 (.93)	.12 (.97)	.036 (.99)	.081 (.98)	.183 (.95)
	Plasma Volume to Surface Area Ratio	1.40 cm	1.40 cm	1.39 cm	1.40 cm	1.40 cm	1.40 cm
	Volume Averaged Maxwellian Electron Temperature (eV)	4.2 eV	9.1 eV	12.2 eV	4.3 eV	7.0 eV	10.2 eV
	Volume Averaged Primary to Maxwellian Electron Density Ratio	.034	.034	.165	.018	.043	.134
	Volume Averaged Primary Electron Energy	27.5 eV	29.5 eV	33.3 eV	21.5 eV	23.5 eV	31. eV
	Volume Averaged Electron Density x 10^{-10}	9.8 cm^{-3}	9.03 cm^{-3}	8.05 cm^{-3}	36.3 cm^{-3}	24.3 cm^{-3}	18.2 cm^{-3}
	Surface Area Averaged Electron Density x 10^{-10}	4.7 cm^{-3}	4.3 cm^{-3}	3.6 cm^{-3}	21.4 cm^{-3}	13.7 cm^{-3}	11.0 cm^{-3}
Calculated Normalized Densities	Neutral Ground State Atoms	.62	.68	.74	.40	.50	.58
	Neutral Metastable Atoms	.12	.063	.04	.14	.036	.049
	Neutral Resonance Atoms	.22	.18	.13	.37	.29	.24
	Singly Charged Ground State Ions	.033	.068	.032	.085	.11	.12
	Singly Charged Metastable Ions	.002	.002	.002	.011	.009	.005
	Doubly Charged Ions	.000	.002	.005	.001	.004	.006
Calculated Ion Production Fractions of Single Ion Type	Neutral Ground State	.42 (.39)*	.60 (.23)	.71 (.[illegible])	.24 (.18)	.40 (.15)	.53 (.29)
	Neutral Metastable State	.21 (.[illegible])	.13 (.19)	.0[illegible] (.[illegible])	.[illegible] (.10)	.19 (.11)	.10 (.25)
	Neutral Resonance State	.[illegible] (.[illegible])	.27 (.21)	.21 (.[illegible])	.44 (.14)	.41 (.13)	.37 (.28)
Calculated Ion Production Fractions of Double Ion Type	Neutral Ground State	.[illegible] (.[illegible]	[illegible]	.23 (.31)	.013 (0.)	.043 (0.)	.10 (.14)
	Neutral Metastable State	.967 (.76)	.013 (.[illegible]	[illegible] (.1)	.004 (0.)	.008 (0.)	.003 (.12)
	Neutral Resonance State	.017 (.20)	.[illegible]	[illegible] (.31)	.011 (0.)	.027 (0.)	.042 (.12)
	Singly Charged Ionic State	.[illegible] (.[illegible])	.[illegible]	[illegible]	.96 (.34)	.89 (.20)	.83 (.33)
	Singly Charged Meta-Table Ionic State	.[illegible]	[illegible]	[illegible]	.0[illegible] (.11)	.024 (.07)	.019 (.31)

* Numbers given in parentheses are the fractions for indicated interaction with the [illegible] per ion electron.

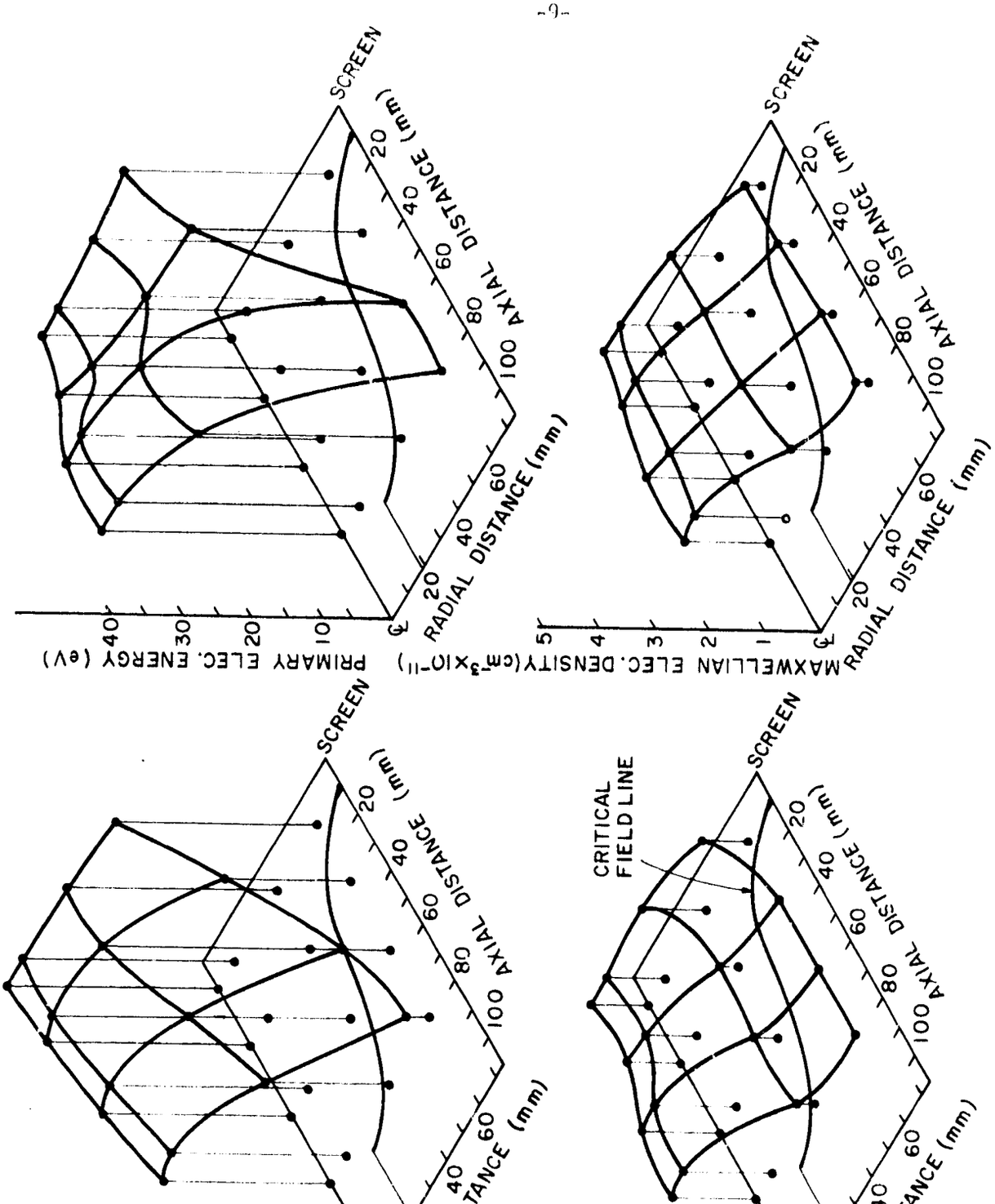

PLASMA PROPERTY PROFILES

SERT II GRIDS - 37v ARC

FIGURE 2

Finally the calculated production rates for singly and doubly charged ions produced through the various intermediate states and normalized by the total production rate for the specie are indicated in Table I along with the fraction of the associated interactions effected by primary electron (in parenthesis). For example at the 37V, flat grid operating point 60% of the single ions were produced as a result of electron interaction with neutral ground state atoms. These neutral ground state-to-single ionic interactions were induced by primary electrons 22% of the time and by Maxwellian electrons the remainder (78%) of the time.

The data of Table I show the resonance and metastable atom states are important intermediate states for the production of single ions. They also show that while the singly charged ionic ground state is the most important intermediate state in the double ion production chain, its importance drops off at higher arc voltages where electron temperatures and energies become sufficient to ionize ground state neutral mercury directly.

The measured double-to-single ion current ratio given in Table I divided by the quantity ($2\sqrt{2}$) is equal to the double-to-single ion density ratio prevailing in the discharge region. The value of this density ratio is compared to that calculated using plasma properties in Figures 3 and 4 for the operating configurations identified in Table I. The double-to-single ion density has been plotted against both propellant utilization and arc voltage in these figures and the figures show the most consistent correlation occurs with propellant utilization. The agreement between theory and experiment is observed to be within 25%.

Because the dished grid thruster operates at higher flow rates and beam currents the absolute magnitude of the double ion density is also significantly higher in this thruster. The extent of the difference in

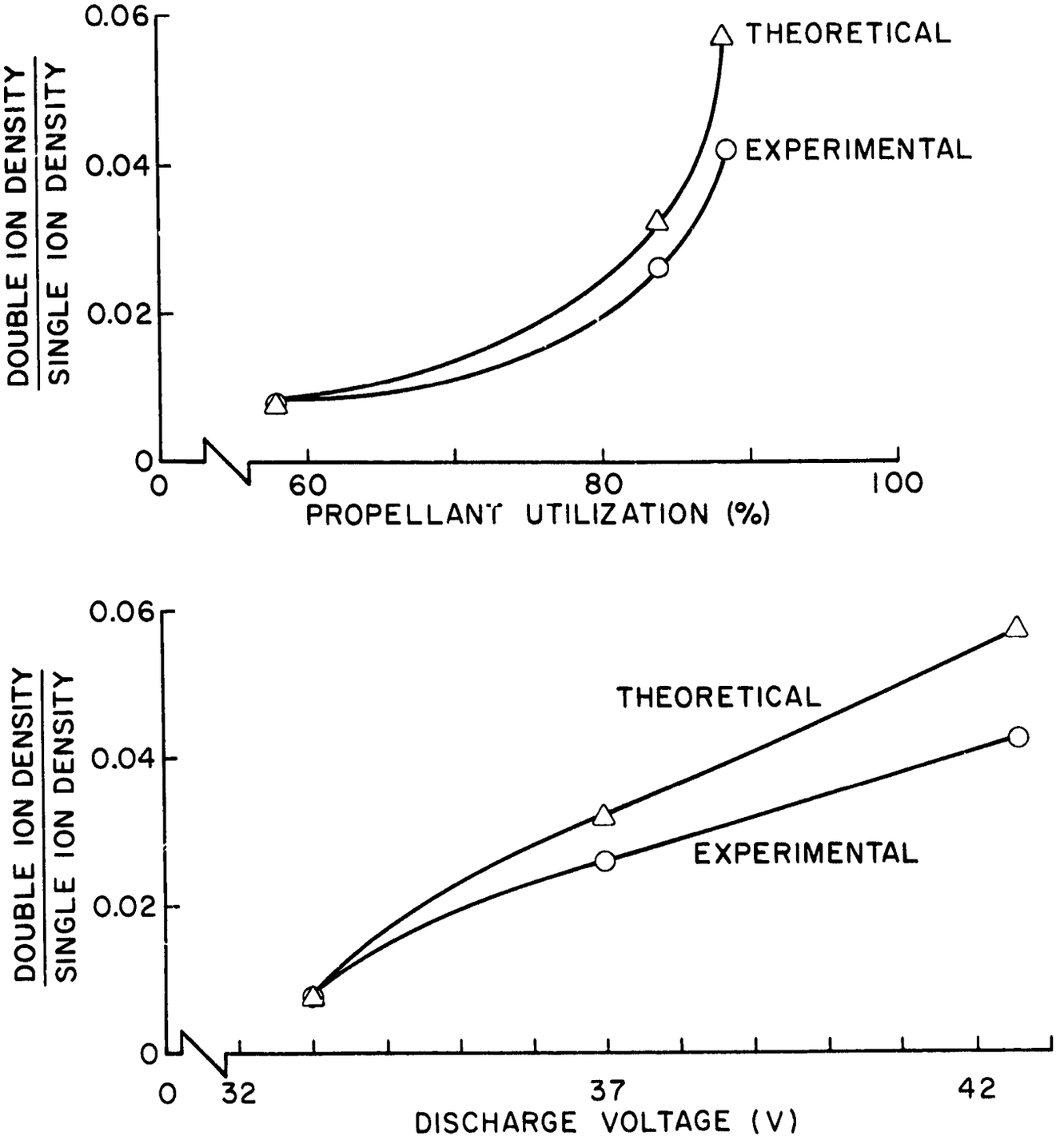

DOUBLE-TO-SINGLE ION DENSITY RATIO
SERT II GRIDS

FIGURE 3

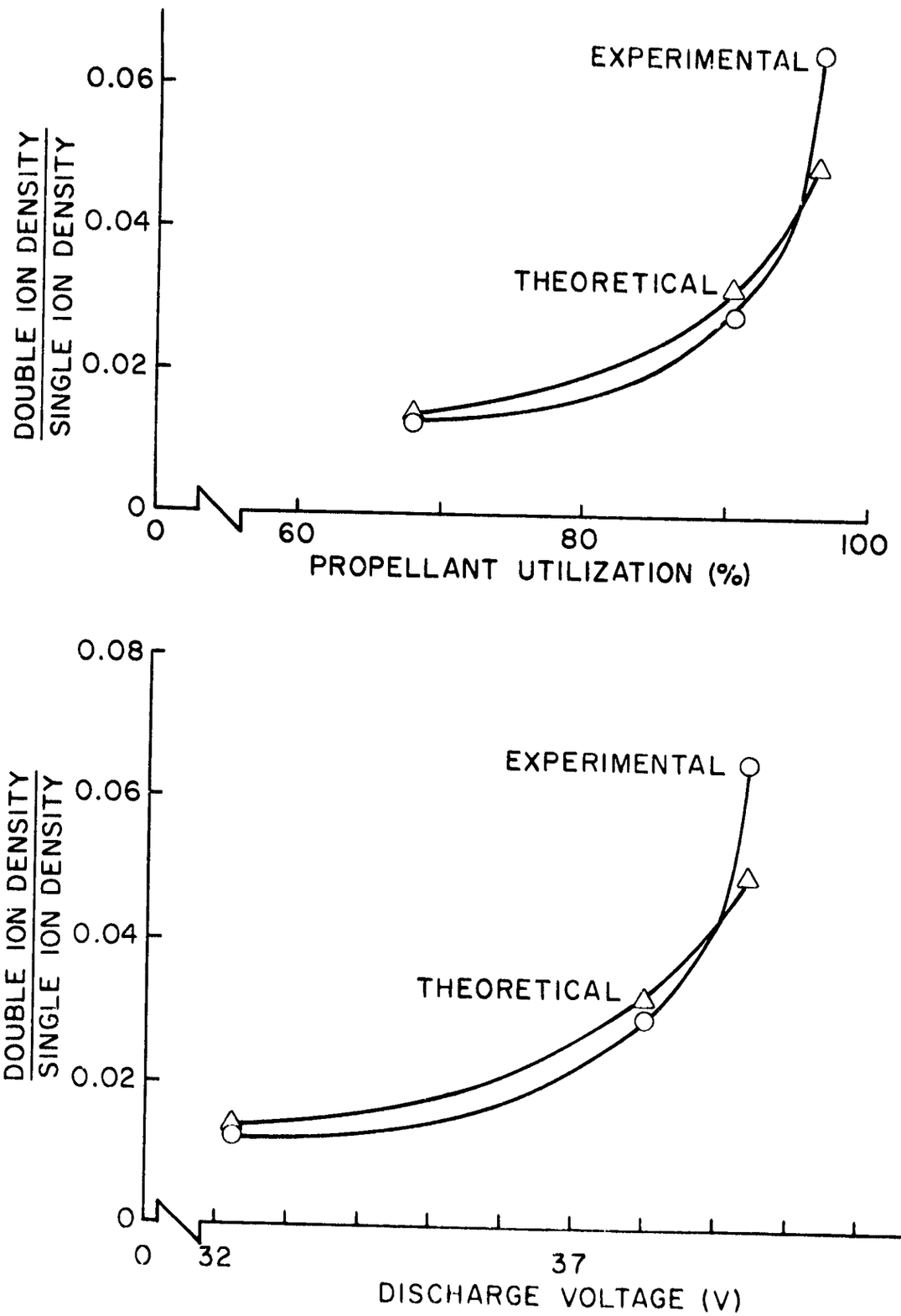

DOUBLE-TO-SINGLE ION DENSITY RATIO
HIGH PERVEANCE DISHED GRIDS

FIGURE 4

double ion density predicted by the computer model for the two thruster grid systems is shown in Figure 5 and is seen to be 2 to 5 times higher in the dished grid thruster.

Conclusion

The mercury discharge model and analysis presented yield double-to-single ion density ratios which agree with experimental measurements to within 25%. The analysis shows that doubly charged mercury ions are produced predominantly via the singly ionized ground state with direct ground state neutral-to-double ion production becoming more significant at high propellant utilizations. Singly charged ions are produced in significant numbers from intermediate metastable and resonance states in addition to direct ionization from ground state neutrals.

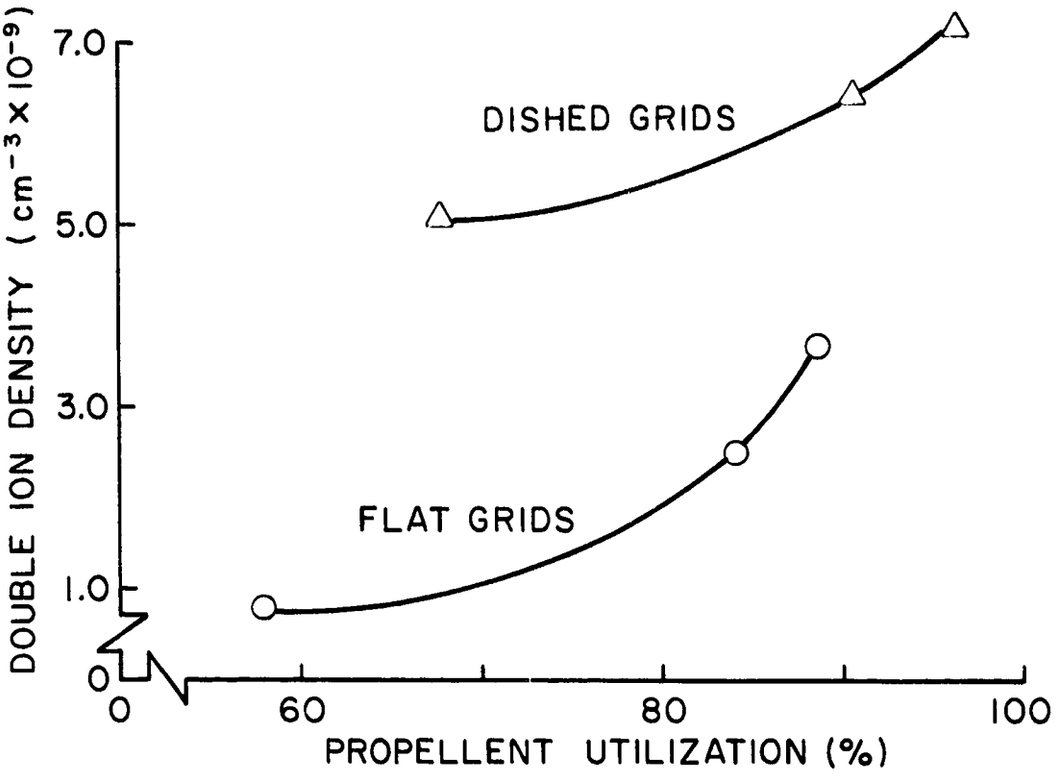

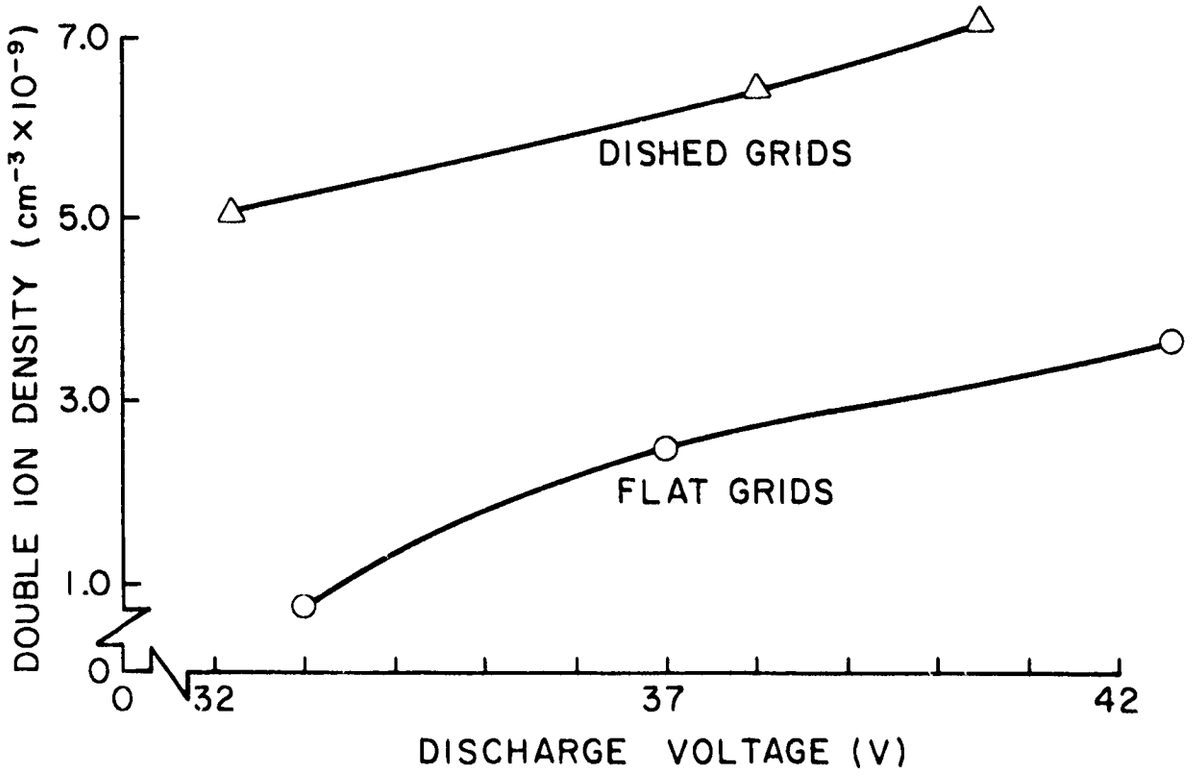

THEORETICAL DOUBLY CHARGED ION DENSITIES

FIGURE 5

SINGLE CUSP MAGNETIC FIELD THRUSTER

John R. Beattie

The single cusp magnetic field (CMF) discharge chamber geometry has been investigated as a viable approach to achieving a uniform current density in the exhaust beam of an electron-bombardment ion thruster. The importance of achieving a uniform profile and the single cusp magnetic field concept are discussed in detail in References [11 and 12].

The cusped magnetic field geometry was chosen on the basis of applying a neutral residence time criterion to a divergent magnetic field geometry. This approach suggested the beam profile of a divergent field chamber could be made more uniform by increasing the ionization probability at the thruster periphery and by confining the axial magnetic field to the chamber wall. This would result in a uniform ion density in the vicinity of the screen grid and, as a result, a uniform ion beam profile.

The effectiveness of the uniform ion density approach to achieving a uniform beam profile has been demonstrated in the past by the radial field thruster[13] and more recently by the multipole thruster.[14] The beam profile flatness parameter F (defined as the ratio of average to maximum beam current density) of the radial field design was 0.67 using mercury as the propellant while the multipole design was in the 0.70 to 0.75 range using argon and xenon as the propellants. Typical values for the SERT II divergent field thruster are 0.40 to 0.49. Faraday probe data presented in this report will show the cusped field discharge chamber has a beam flatness parameter in the 0.70 to 0.82 range.

Apparatus

A SERT II discharge chamber was modified to produce the cusped magnetic field geometry illustrated in Figure 6. The changes consisted

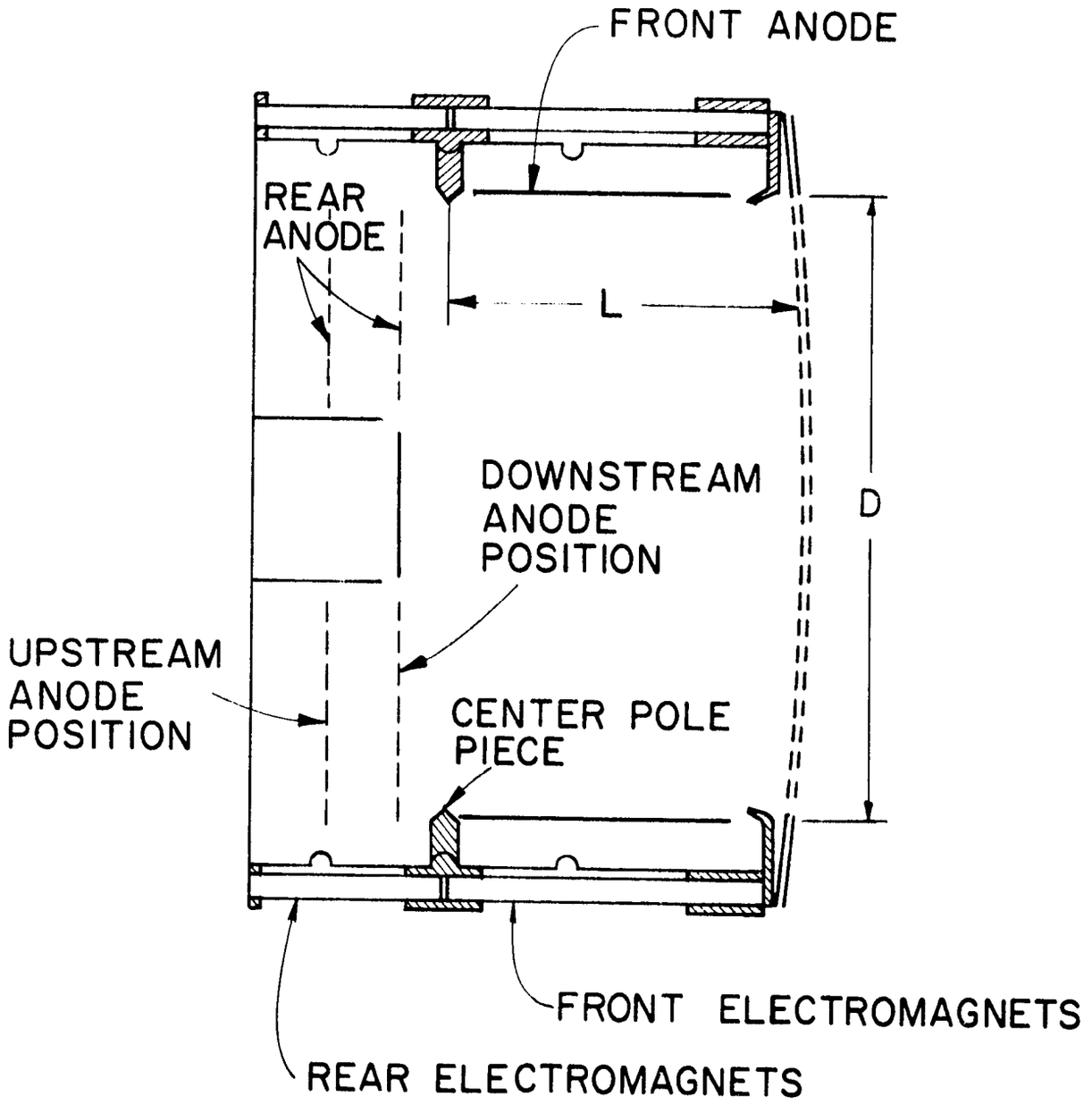

CUSPED MAGNETIC FIELD THRUSTER SCHEMATIC

FIGURE 6

of the addition of a center magnet pole piece and the installation of a movable rear anode in the upstream end of the discharge chamber. The thruster length-to-diameter ratio (L/D) could be varied by replacing the downstream section of the chamber. Additional modifications included the replacement of the SERT II permanent magnets with independent front and rear electromagnets and the installation of a variable magnetic baffle. By reversing the polarity of the magnet power supplies, the cusped magnetic field geometry could be converted to a divergent field geometry. Iron filings maps of the cusped and divergent fields are presented in Figure 7 for a chamber length-to-diameter ratio of 0.53.* The SERT II accelerator system was replaced with a compensated dished grid optical system and the propellant feed system was modified to permit independent control of the main and cathode flow rates. The main and neutralizer cathodes were replaced with 0.5 mm diameter orifice cathodes to facilitate sustained thruster operation at high beam currents.

A movable Langmuir probe was installed inside the discharge chamber to obtain plasma diagnostic information. In addition, a Faraday cup probe which could be swept through the ion beam at any desired axial location was installed to obtain beam current density profiles. An $\vec{E} \times \vec{B}$ momentum analyzer[2] was installed in the vacuum facility to measure the charge-to-mass composition of the ion beam. The analyzer installation was designed to permit the instrument to be swept through the ion beam with the probe

---

* The length-to-diameter ratios referred to in this report are 0.23, 0.30, and 0.53. These differ slightly from the previously reported values of 0.3, 0.4, and 0.6. The difference is due to a slightly different definition of the length L and does not imply a geometrical difference.

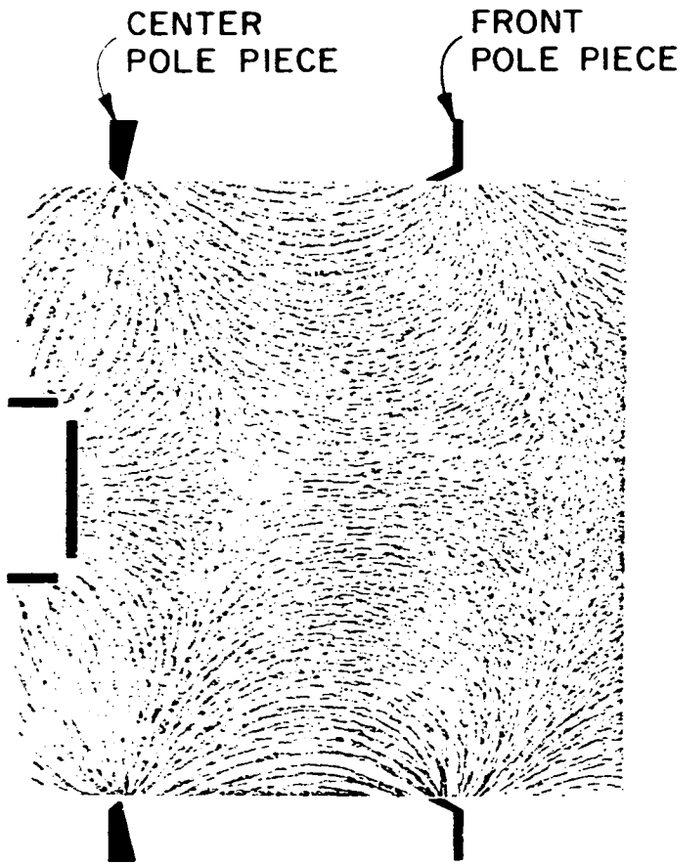

A. CUSPED FIELD GEOMETRY

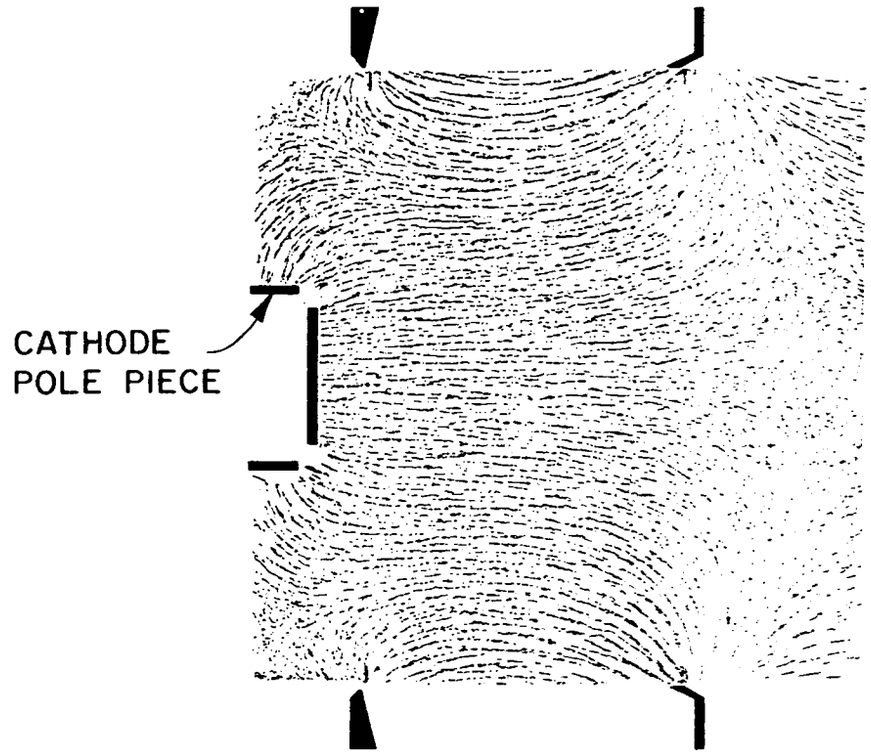

B. DIVERGENT FIELD GEOMETRY

IRON FILINGS MAPS (1/2 0.53)

FIGURE 7

pitched at various angles. This permitted the single and double ion dispersion profiles to be determined as a function of thruster radius.

All data presented were obtained at 1kV and -0.5kV screen and accelerator grid potentials and 0.3A keeper current. Solid symbols have been used on performance curves to indicate the 37V arc voltage condition. Discharge power calculations include the keeper losses and the total propellant flow rate was 730 mA unless indicated otherwise.

Langmuir probe data presented herein were analyzed by the numerical procedure of Reference [10]. $\vec{E} \times \vec{B}$ momentum analyzer data were recorded and analyzed using the procedure outlined in Appendix A. Details of the Langmuir and Faraday probe installations are given in References [9 and 15]. A schematic diagram of the $\vec{E} \times \vec{B}$ momentum analyzer circuit is presented in Reference [14].

Beam Profile

The beam profile flatness parameter measured at a distance of 6 mm downstream of the accelerator system is presented as a function of chamber length-to-diameter ratio in Figure 8. Beam profile data reported in Reference [11] which were obtained at a distance of 50 mm downstream of the grids are also presented. The trends are seen to be the same for both probe locations and the two curves are shifted by almost a constant amount. The data recorded close to the accelerator grid indicate a 10% increase in the beam flatness parameter was realized with the shorter discharge chamber.

Ion beam current density profiles measured 6 mm downstream of the accelerator grid are presented in Figure 9 for the SERT II and cusped field thrusters. These data were normalized such that the integrated beam current is the same for each profile. When normalized in this manner,

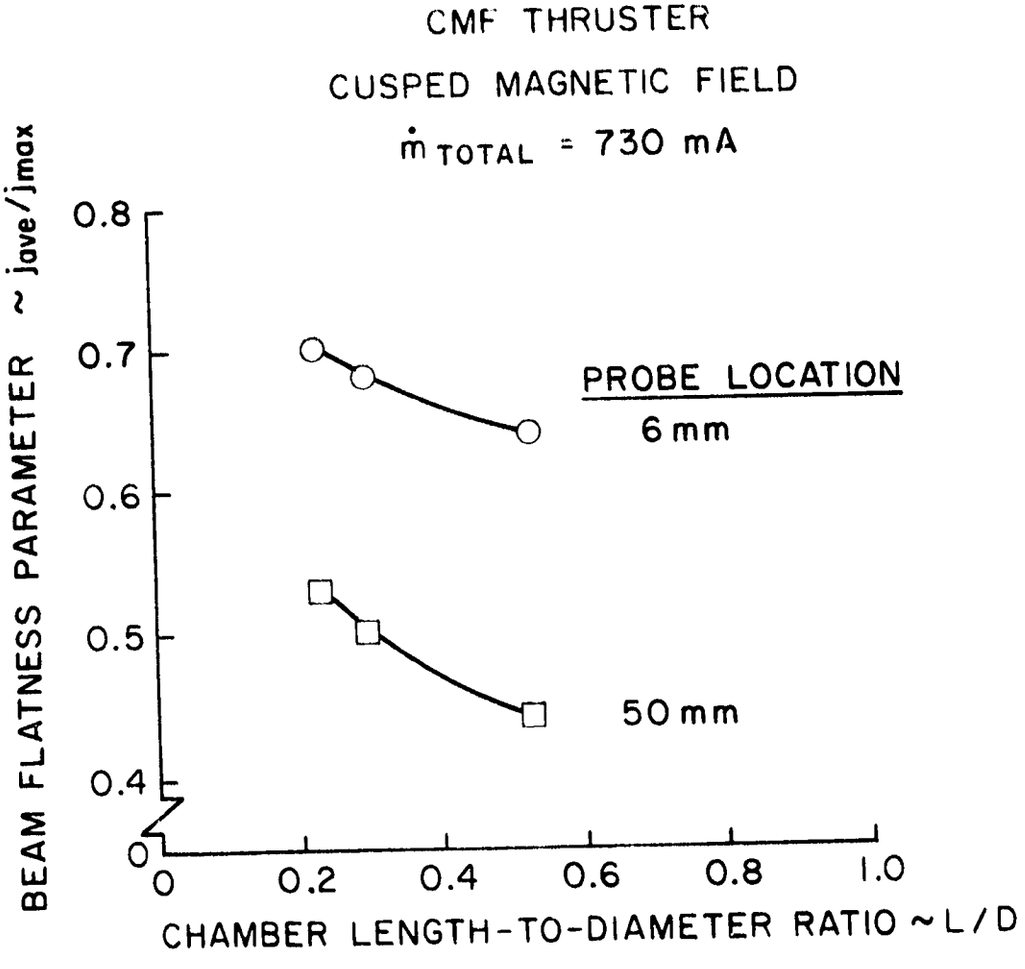

EFFECT OF CHAMBER LENGTH-TO-DIAMETER RATIO ON BEAM FLATNESS PARAMETER

FIGURE 8

CMF THRUSTER

CUSPED MAGNETIC FIELD

$\dot{m}_{TOTAL.}$ = 730 mA

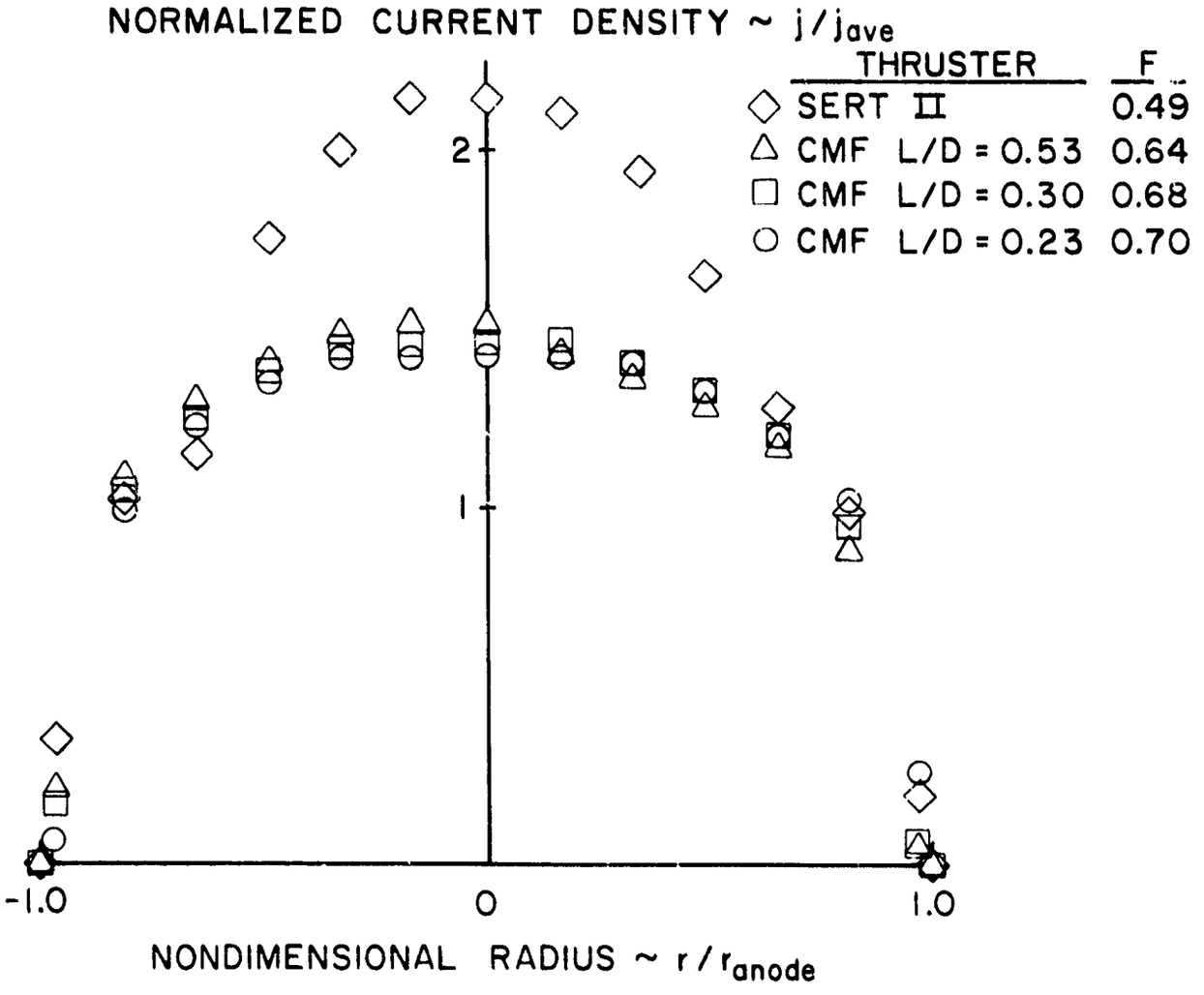

NORMALIZED BEAM CURRENT DENSITY PROFILES

FIGURE 9

the reciprocal of the peak normalized density is numerically equal to the flatness parameter. The data of Figure 9 indicate a significant improvement in beam profile flatness parameter has been realized with the cusped field discharge chamber design. The beam flatness parameter for the cusped field thruster having a length-to-diameter ratio of 0.23 is seen to be 40% greater than the SERT II value at the same operating conditions.

The effect of magnetic field geometry on beam profile is illustrated in Figure 10. These data are presented for the cusped and divergent magnetic field geometries with a discharge chamber length-to-diameter ratio of 0.23. The effectiveness of the cusped field design in achieving a more uniform beam current density is evident when comparing these profiles. The divergent field data of Figure 10 and the SERT II data of Figure 9 indicate the short chamber divergent field geometry has a flatness parameter which is 27% greater than the SERT II value. Beam profile comparisons for the cusped and divergent field geometries were found to have the same trend as shown in Figure 10 for the intermediate and long chamber lengths. The effect was less pronounced for the long chamber (100% of SERT II length) as one might expect. This occurs because the magnetic field is largely axial over the entire chamber cross section for both configurations as illustrated in Figure 7. As the cusped field chamber length is reduced however the axial component of the field is significant only near the chamber wall. This results in a uniform plasma density over much of the downstream region of the discharge chamber.

The axial location of the movable rear anode was found to have little effect on the beam profiles of either the cusped or divergent field geometries for all length-to-diameter ratios investigated. This is to be

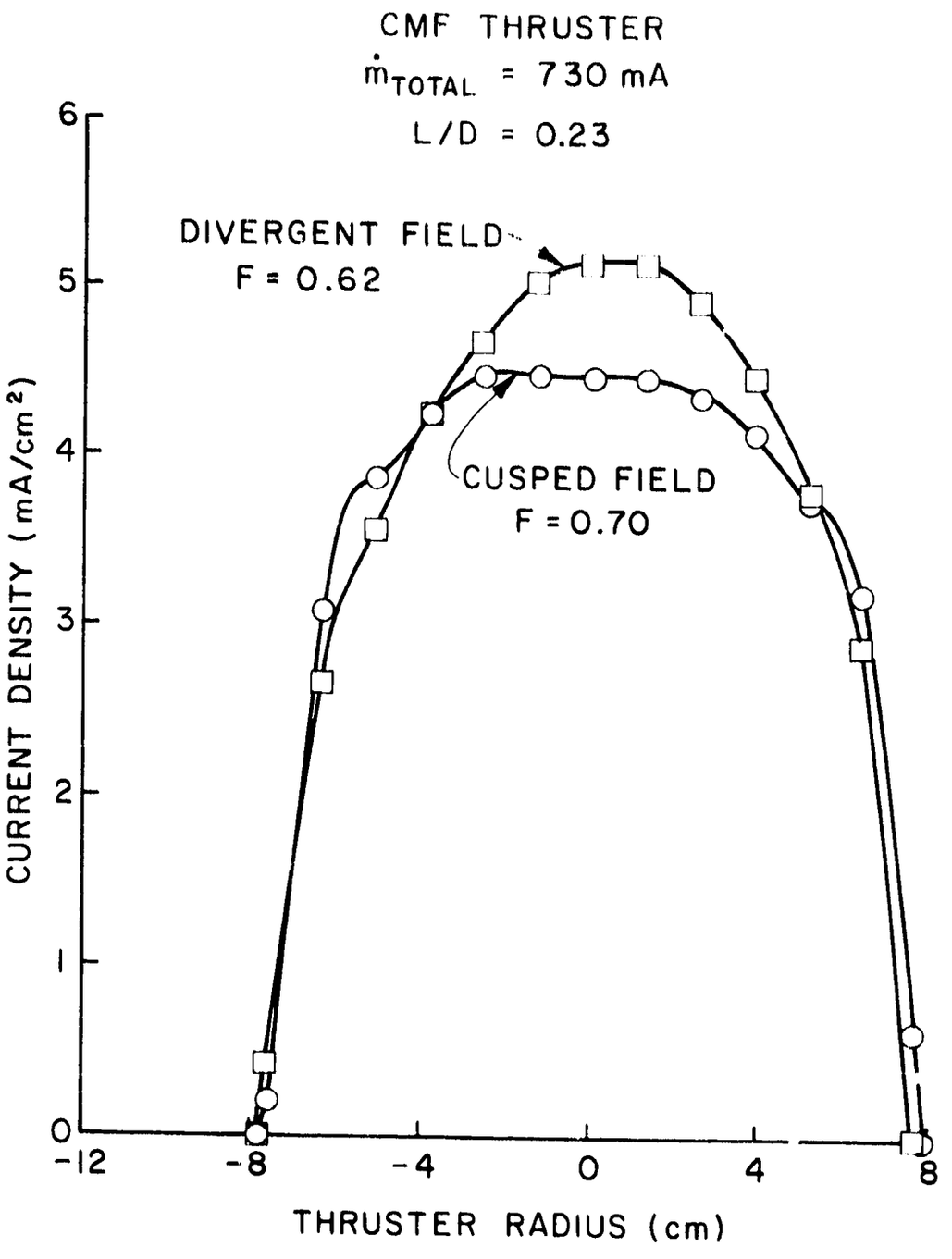

EFFECT OF MAGNETIC FIELD GEOMETRY ON BEAM PROFILE

FIGURE 10

expected since the anode position primarily determines the chamber volume-to-area ratio and had little effect on the plasma density profile at the screen grid.

The effect of throttling on the beam current density profile is seen by comparing Figures 10 and 11 for the cusped field geometry having a length-to-diameter ratio of 0.23. The improvement in the beam flatness at the throttled flow condition is thought to be due to the presence of fewer double ions at the lower ion beam current. Since double ions are produced mostly from single ions, the double ions are preferentially produced near the center of the discharge chamber where the plasma density is highest. This condition combined with the larger Bohm velocity near the chamber wall suggests the double ion density profile would be more peaked than the single ion profile. Experimental measurements of the double and single ion current density profiles indicate that this is in fact the case. The argument presented above would also explain the dependence of the cusped field thruster beam flatness on propellant utilization at a fixed propellant flow rate. The effects of throttling and propellant utilization on double ion content have not been studied experimentally to verify this theory however.

Performance

The cusped magnetic field thruster was operated initially using an uncompensated dished grid accelerator system having the dimensions listed in Table II. Performance data for this thruster configuration were reported in Reference [11] and are reproduced in Figure 12 for comparison with data obtained during the current reporting period. Figure 13 presents performance data obtained with a set of compensated dished grids having the dimensions listed in Table II. Both Figures 12 and 13 indicate a substantial improvement

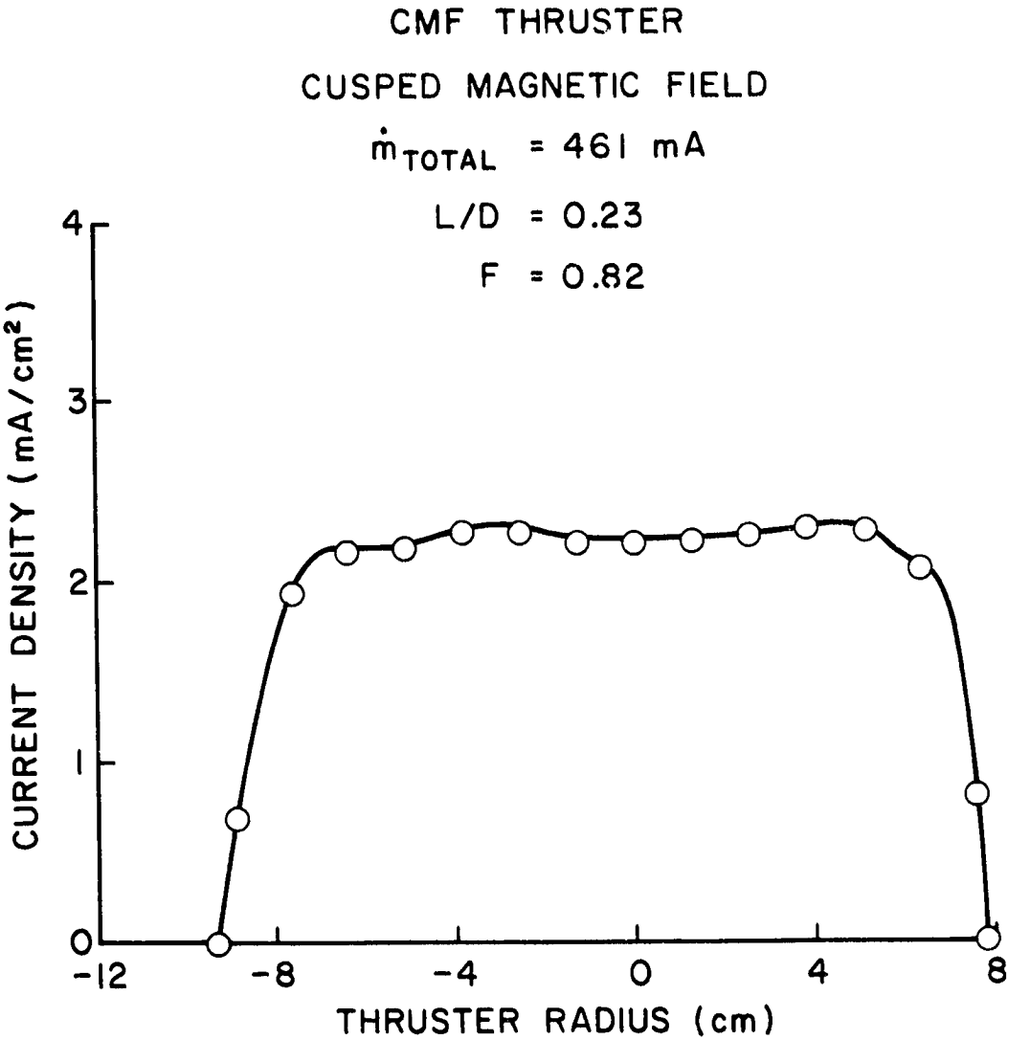

BEAM CURRENT DENSITY PROFILE - THROTTLED FLOW CONDITION

FIGURE 11

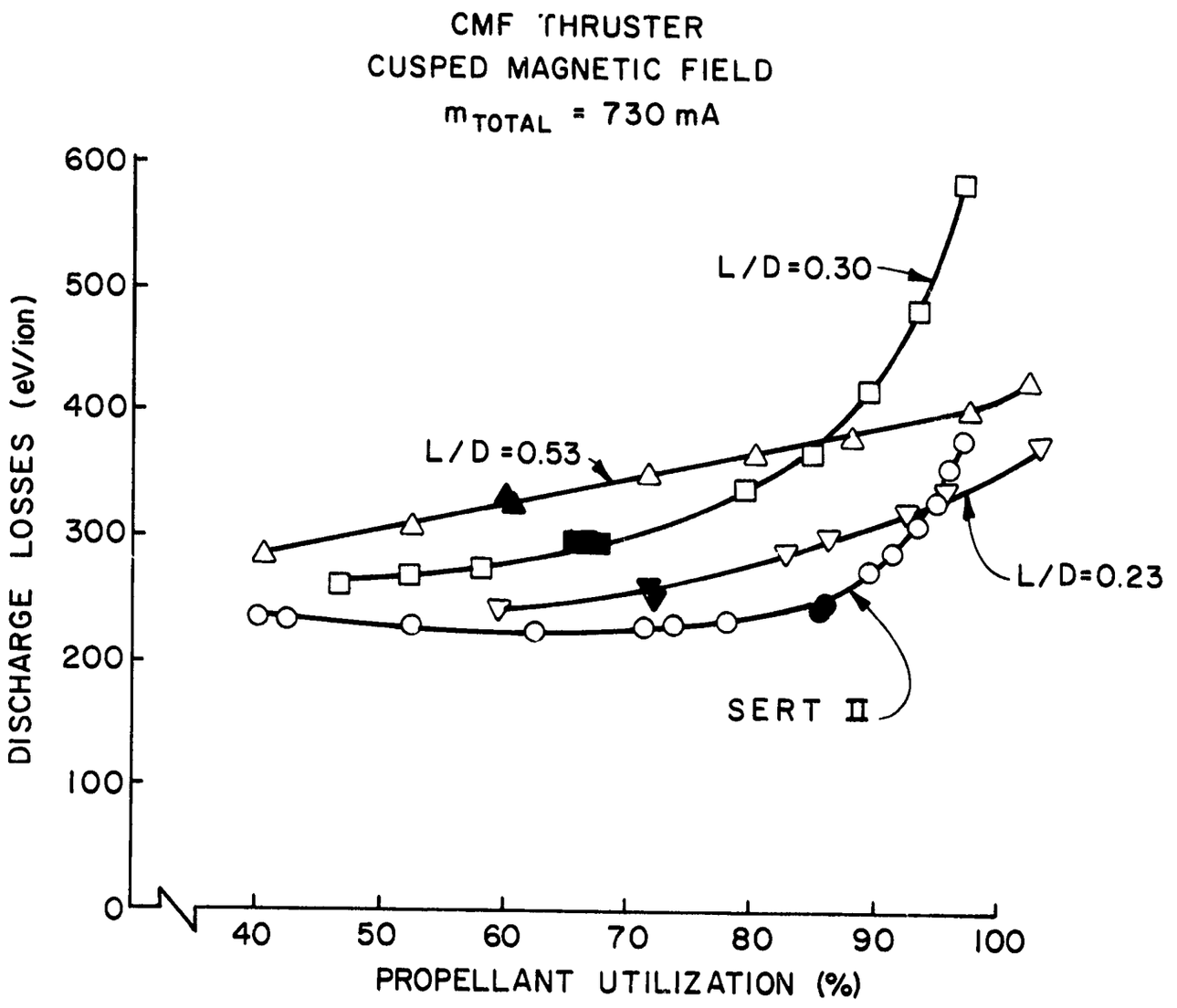

THRUSTER PERFORMANCE COMPARISON - CUSPED MAGNETIC FIELD GEOMETRY

FIGURE 12

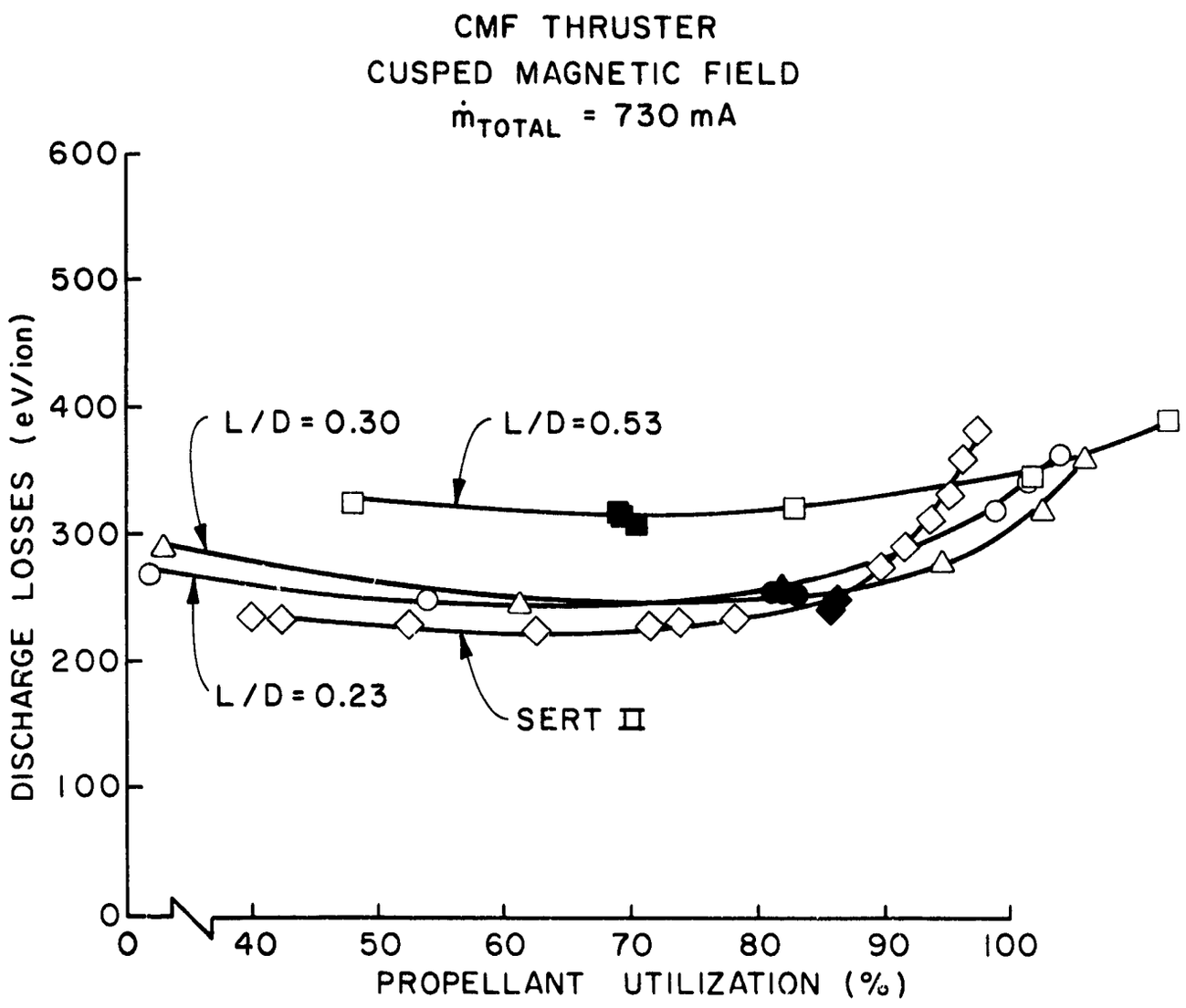

THRUSTER PERFORMANCE COMPARISON - CUSPED MAGNETIC FIELD GEOMETRY

FIGURE 13

TABLE II. ACCELERATOR SYSTEM DIMENSIONS

	Uncompensated		Compensated	
	Screen	Accelerator	Screen	Accelerator
Thickness	0.46 mm	0.46 mm	0.38 mm	0.51 mm
Hole Spacing	2.5 mm	2.5 mm	2.08 mm	2.08 mm
Hole Diameter	2.0 mm	2.0 mm	1.91 mm	1.6 mm
Open Area	58%	58%	76%	54%

in thruster performance was realized as a result of reductions in the discharge chamber length. A comparison of Figures 12 and 13 reveals significant reductions in baseline discharge losses were realized with the compensated grid set which has a thicker accelerator grid with smaller hole diameters and the larger open area screen grid. Also, the performance data for the chamber having a length-to-diameter ratio of 0.30 indicates a marked difference in the shape of the curves at high propellant utilization. The reason for this apparent discrepancy is not known. Since the data of Figure 13 exhibit a more consistent trend with discharge chamber length reductions, the data of Figure 12 are felt to be the source of this discrepancy. The apparent error in Figure 12 could be due to an error in the flow rate data for the chamber length-to-diameter ratio of 0.30. If the measured flow rate was high the calculated propellant utilization would be less than the true value and the performance curve would be shifted to lower utilizations. This would explain both the presence of the "knee" in the data of Figure 12 and the difference in baseline losses for the short and intermediate chamber lengths.

The effect of discharge chamber length on performance for the divergent magnetic field geometry is illustrated in Figure 14. The baseline

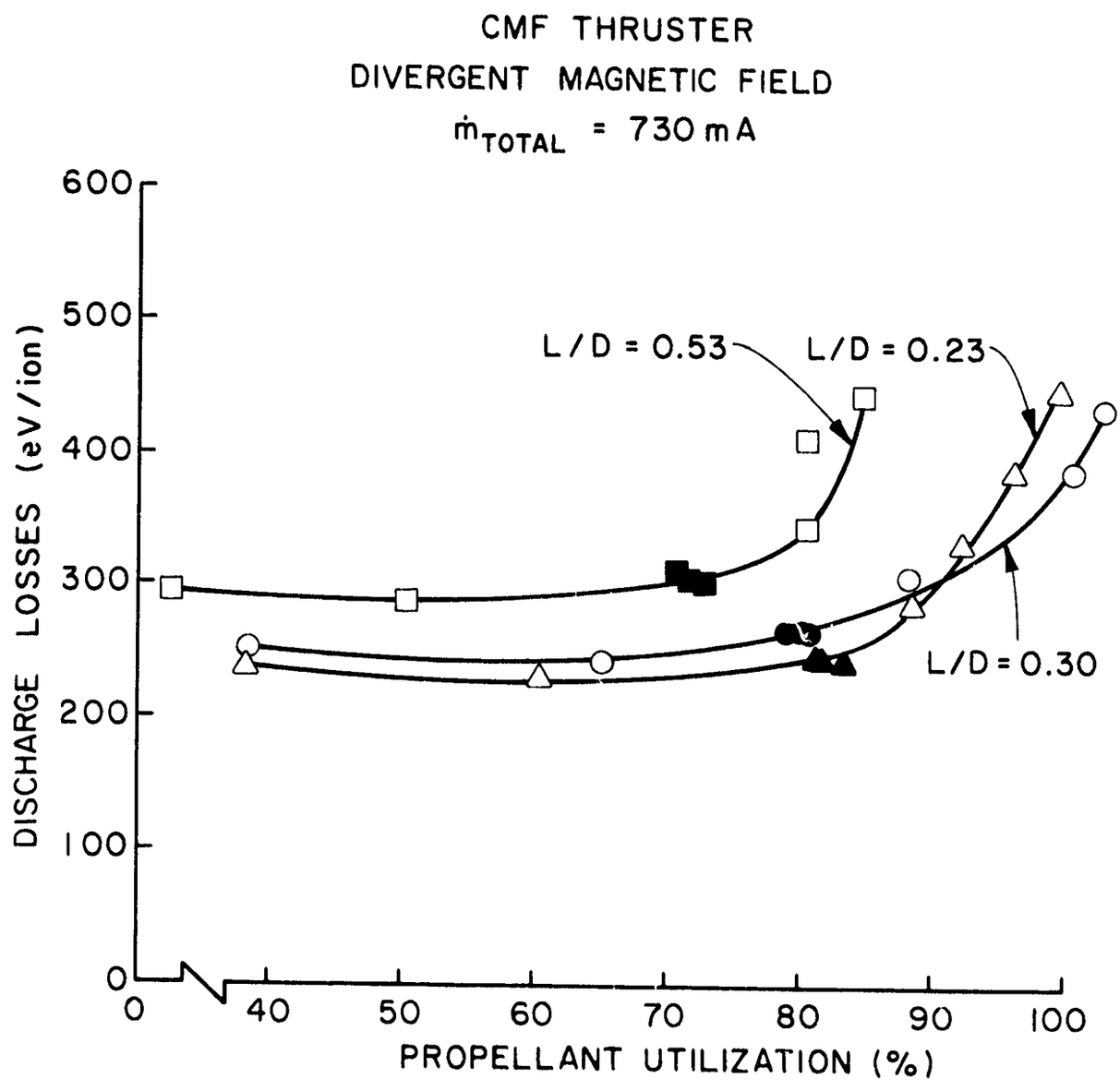

THRUSTER PERFORMANCE COMPARISON - DIVERGENT MAGNETIC FIELD GEOMETRY

FIGURE 14

discharge losses are seen to decrease with a reduction in chamber length as was observed with the cusped magnetic field geometry. The increase in propellant utilization observed with the shorter discharge chamber appears anomalous at first glance, but is in agreement with both neutral loss rate[16] and double ion production[3] theories when the volume-to-surface area ratios of the three configurations are taken into account. Iron filings maps of the magnetic field existing in the three configurations indicate the primary electron region volume-to-surface area ratio increases as the chamber length is reduced. Since theory predicts an increase in double-to-single ion density ratio and a decrease in neutral loss rate with increasing volume-to-area ratio, the shifting of the performance curve to higher propellant utilizations is expected. The volume-to-area ratio of the short and intermediate chambers was found to be about the same and the crossover of the two curves is probably due to differences in the plasma properties existing in the two chambers.

Perhaps the most notable difference between the cusped field and divergent field performance data is the presence of a "knee" in the divergent field data and the lack of one in the cusped field data. This is illustrated in Figure 15 which is a comparison of the cusped and divergent field performance for a chamber length-to-diameter ratio of 0.53. The cusped field data suggest a significant double ion population exists in this chamber at the high utilization conditions. The flattening of the performance curve illustrated in Figure 15 for the long discharge chamber is also apparent for the shorter chambers as can be seen by comparison of Figures 13 and 14.

The effect of rear anode position on thruster performance was found to be the same for all three discharge chamber lengths and both magnetic

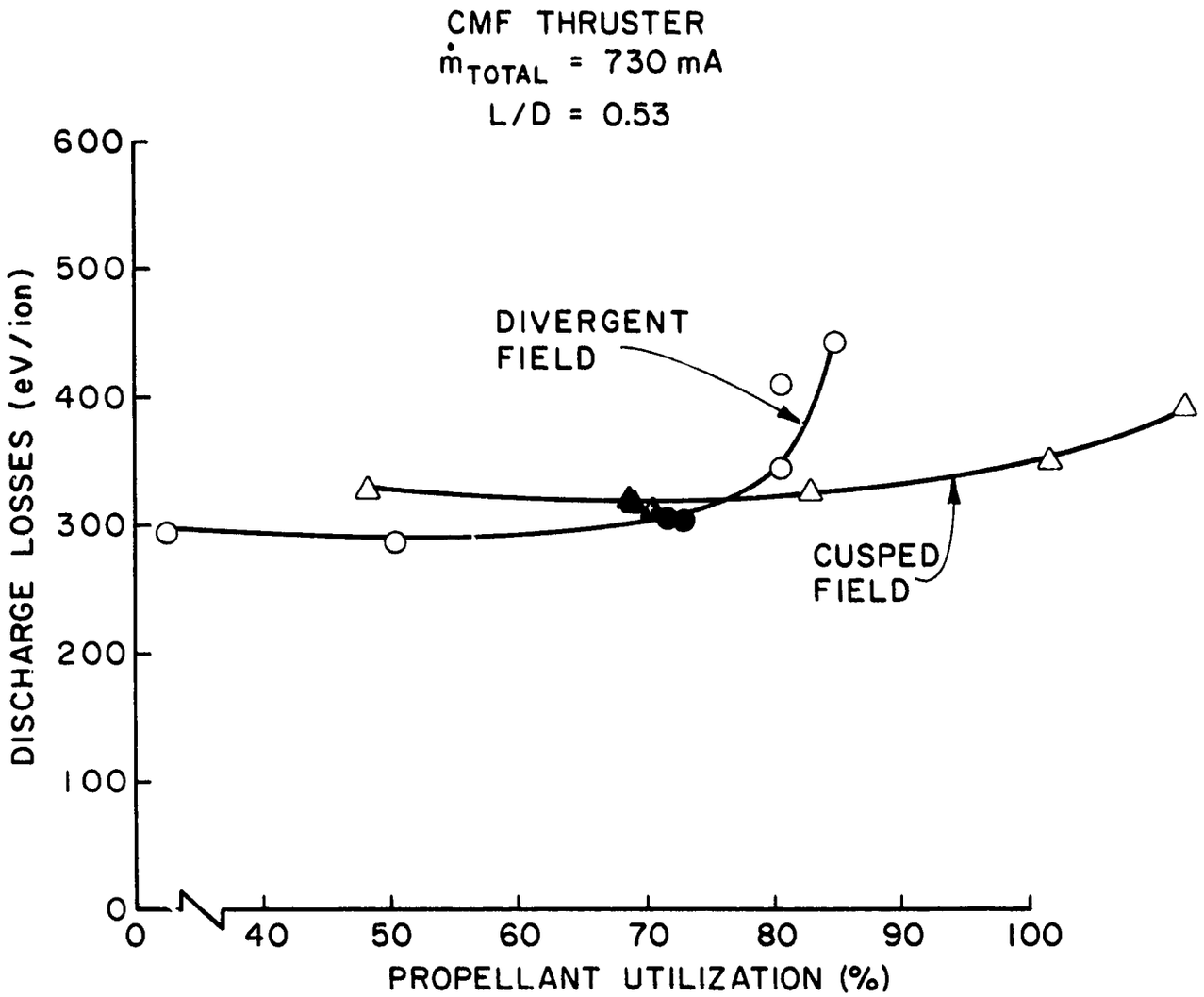

EFFECT OF MAGNETIC FIELD GEOMETRY ON THRUSTER PERFORMANCE

FIGURE 15

field geometries. In each case the downstream movement of the rear anode resulted in a decrease in beam current for the same power input. This effect has the tendency to shift performance data to lower propellant utilization and higher discharge losses. The reason for the performance degradation is due to a reduction in both the primary electron energy and Maxwellian electron temperature as will be shown in the section on plasma properties.

Double Ionization

Double and single ion beam currents were obtained by the use of an articulating $\vec{E} \times \vec{B}$ momentum analyzer.[2] Details of the data acquisition and reduction procedures are presented in Appendix A. The double-to-single ion current ratios presented in this section were measured at the thruster conditions indicated by solid symbols on the corresponding performance curves. Figure 16 presents the double-to-single ion beam current ratio as a function of chamber length-to-diameter ratio for the cusped magnetic field geometry. Since the double-to-single ion density ratio is equal to $1/(2\sqrt{2})$ times this current ratio these data suggest a chamber length exists which results in a minimum double-to-single ion density ratio. Double ion production theory[3] predicts a linear dependence of the double-to-single ion density ratio on the chamber volume-to-surface area ratio. The nonlinear nature of Figure 16 suggests the plasma properties also vary with chamber length. The variation of the plasma properties with discharge chamber geometry and magnetic field configuration will be discussed in the next section.

Figure 17 presents the double-to-single ion beam current ratio as a function of chamber length-to-diameter ratio for the divergent magnetic field geometry. Here the effect of chamber length on the double ion

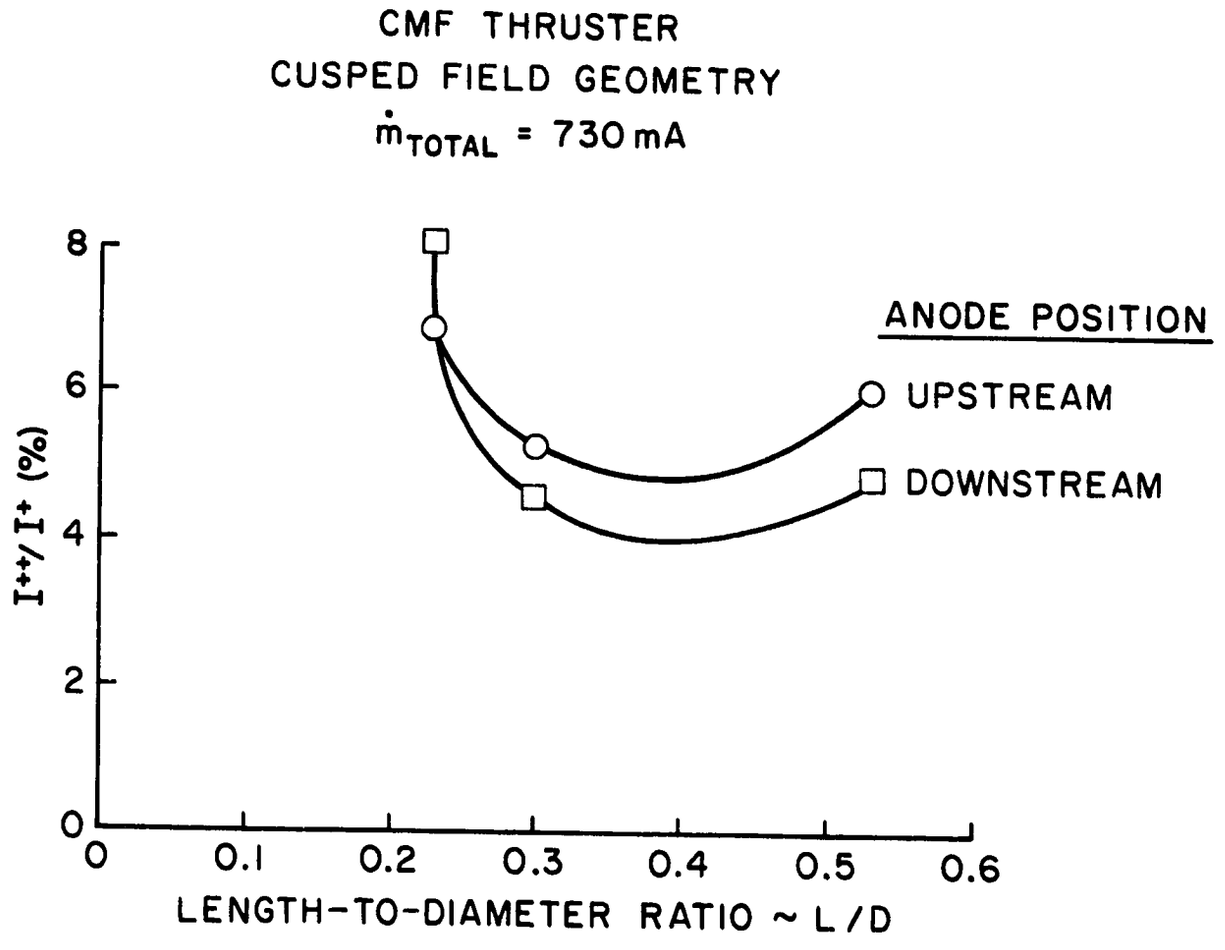

EFFECT OF CHAMBER LENGTH-TO-DIAMETER RATIO

ON DOUBLE-TO-SINGLE ION CURRENT RATIO

(CUSPED FIELD GEOMETRY)

FIGURE 16

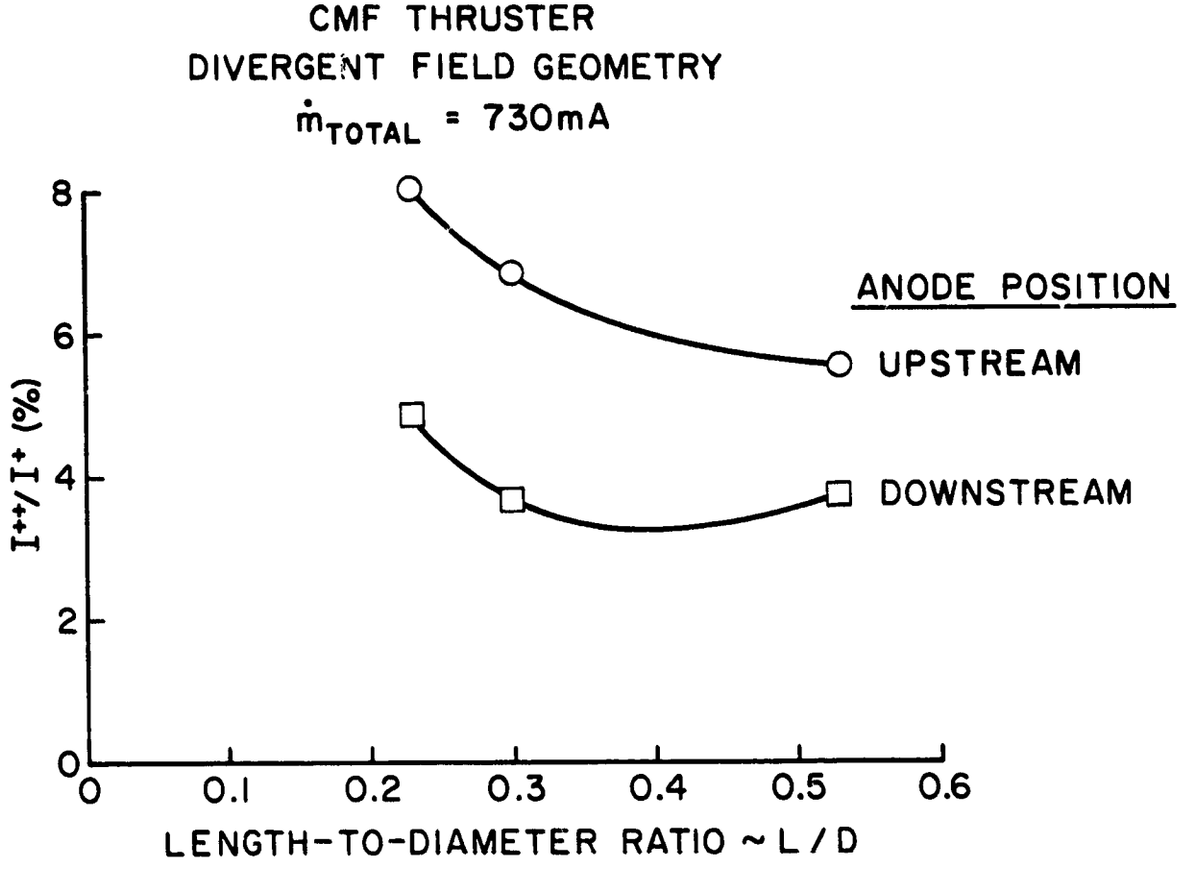

EFFECT OF CHAMBER LENGTH-TO-DIAMETER RATIO

ON DOUBLE-TO-SINGLE ION CURRENT RATIO

(DIVERGENT FIELD GEOMETRY)

FIGURE 17

population agrees fairly well with the theoretical dependence on volume-to-area ratio which generally decreases with chamber length. The nonlinear nature of the data of Figure 17 again suggests however a slight variation in the plasma properties with discharge chamber length.

The effect of the rear anode location on the double-to-single ion density ratio is seen from Figures 16 and 17 to be essentially the same for each chamber length and magnetic field geometry. The reduction in the double-to-single ion density ratio associated with the downstream anode position is consistent with the reduction in the volume-to-surface area ratio caused by the anode movement. However, the effect illustrated in Figures 16 and 17 is not due entirely to volume-to-surface area ratio changes. Langmuir probe data presented in the next section indicate the downstream movement of the rear anode had a large effect on the Maxwellian electron temperature and primary electron energy.

Plasma Properties

The cusped field thruster discharge chamber theory[11, 12] has suggested electrons have the tendency to be trapped in a magnetic bottle region which exists in the upstream end of the chamber. This theory was verified for the three different discharge chamber lengths by Langmuir probe measurements. The variation of the plasma electron density with axial distance is presented in Figure 18 for each discharge chamber length and both the cusped and divergent magnetic field geometries. The parameter r/r_{anode} shown on these curves is the nondimensional radius at which the probe sweep was made. Comparison of the cusped and divergent field data clearly indicates the axial density profile of the divergent field geometry is quite uniform while the cusped field profile is highly nonuniform. The

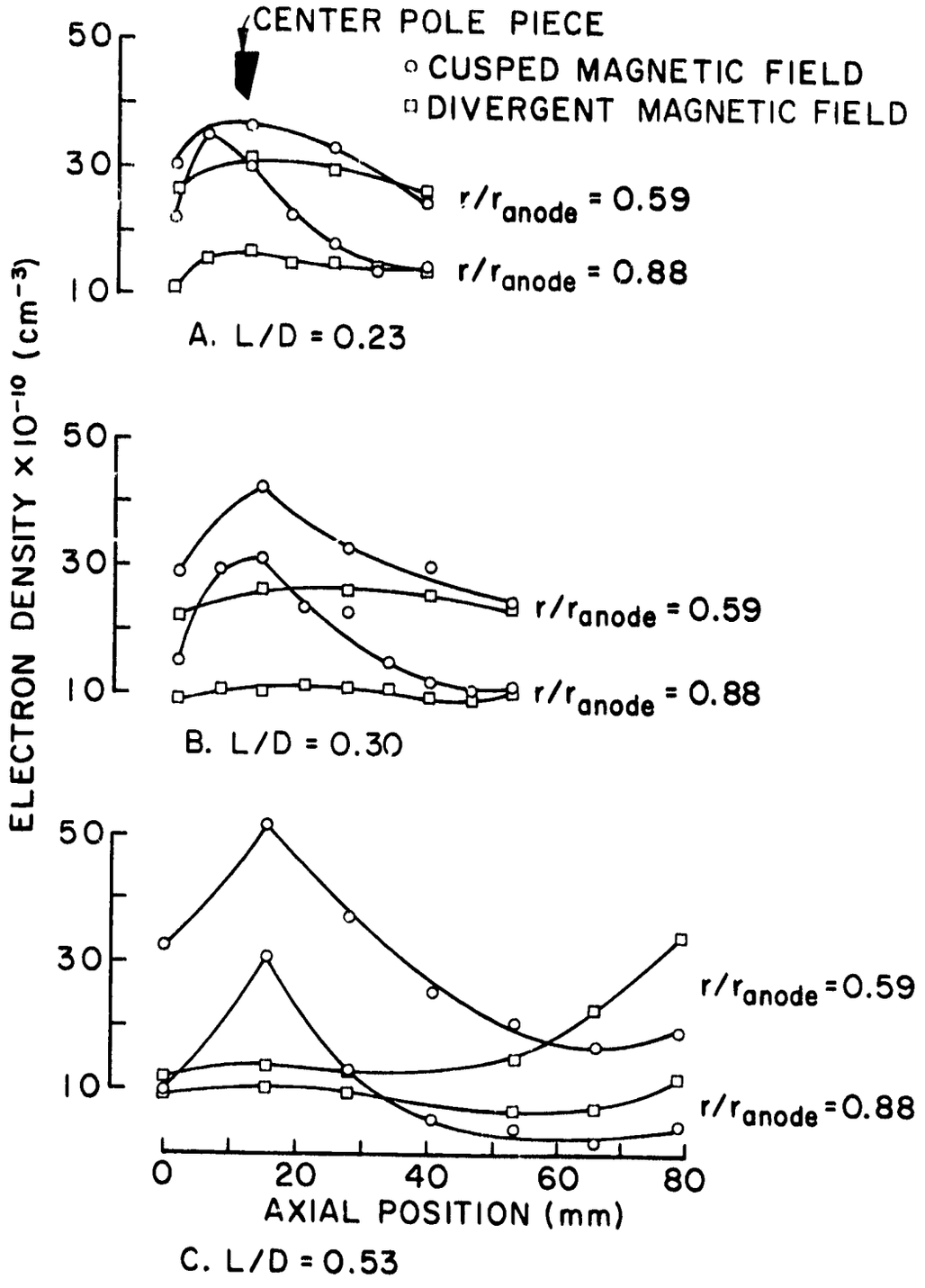

PLASMA PROPERTY VARIATIONS

FIGURE 18

cusped field profiles indicate the presence of a localized region where the electron density is as much as ten times the value near the screen grid. The axial location of this localized region of high electron density corresponds to the position of the center magnet pole piece. Figure 18C indicates an increase in the plasma electron density near the screen grid for the divergent magnetic field geometry. This increase occurs because the probe crosses the critical field line and enters into the primary electron region as it moves downstream. This can be visualized by considering the iron filings map of Figure 7B. The Maxwellian electron temperature and primary electron energy were found to exhibit trends similar to those illustrated in Figure 18.

Plasma property surfaces are presented in Figure 19 for the cusped and divergent magnetic field geometries with a discharge chamber length-to-diameter ratio of 0.23. Comparison of the cusped field and divergent field surfaces indicates the cusped field geometry generally results in much more uniform plasma properties than the divergent field geometry. The reduction in the radial plasma density gradient is clearly evident in the cusped field design and this is reflected in the more uniform beam profile of this thruster. The magnetic bottle effect is apparent when considering the plasma property variations near the center magnet pole piece of the cusped field geometry. The general trends evident in Figure 19 were also observed when comparing the surfaces for the intermediate and long discharge chambers.

The effect of the rear anode position on Maxwellian electron temperature and primary electron energy is presented in Figure 20 for the cusped field geometry with a length-to-diameter ratio of 0.23. These data indicate

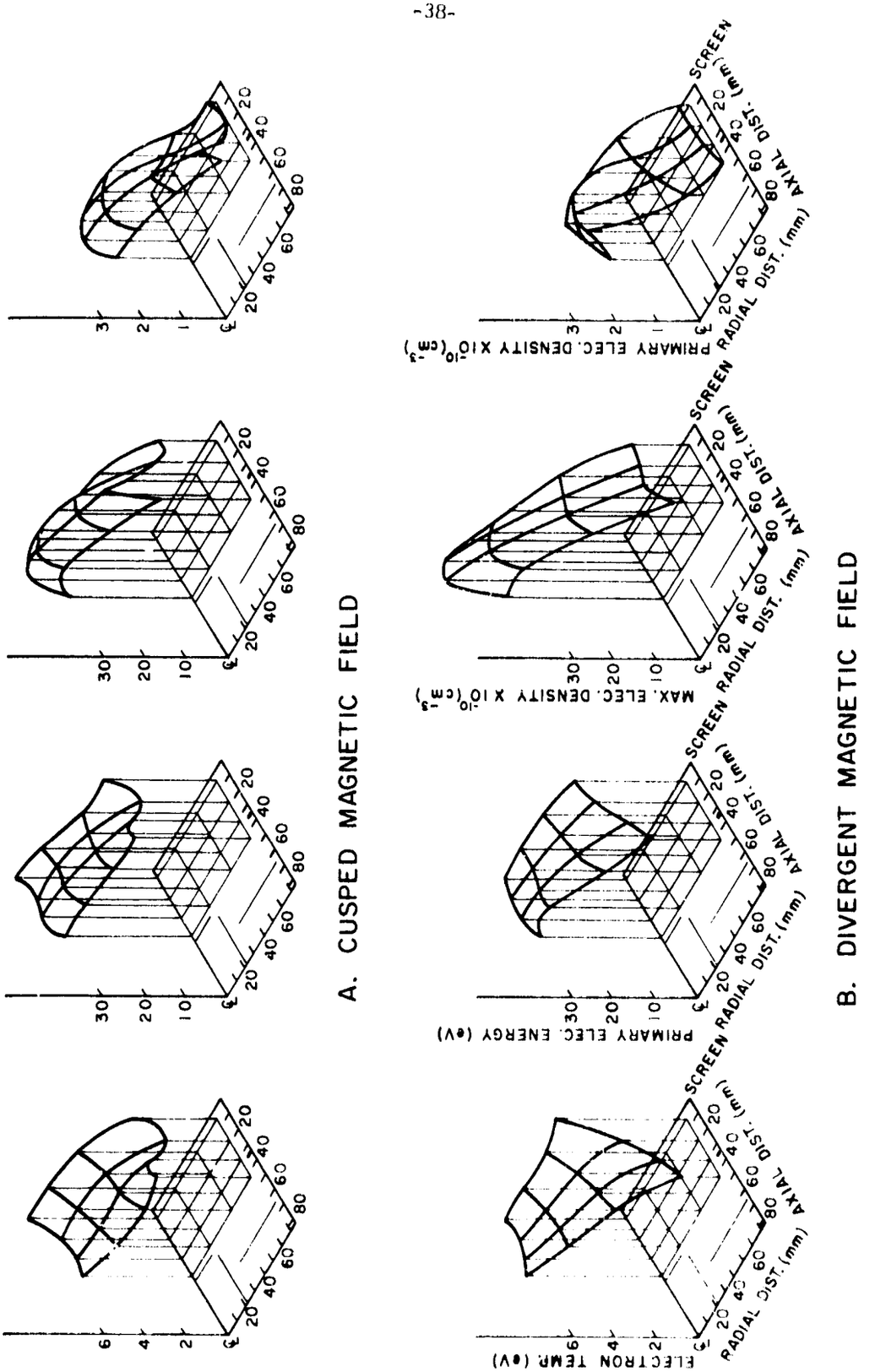

EFFECT OF MAGNETIC FIELD GEOMETRY ON PLASMA PROPERTIES (L/D = 0.23)

FIGURE 19

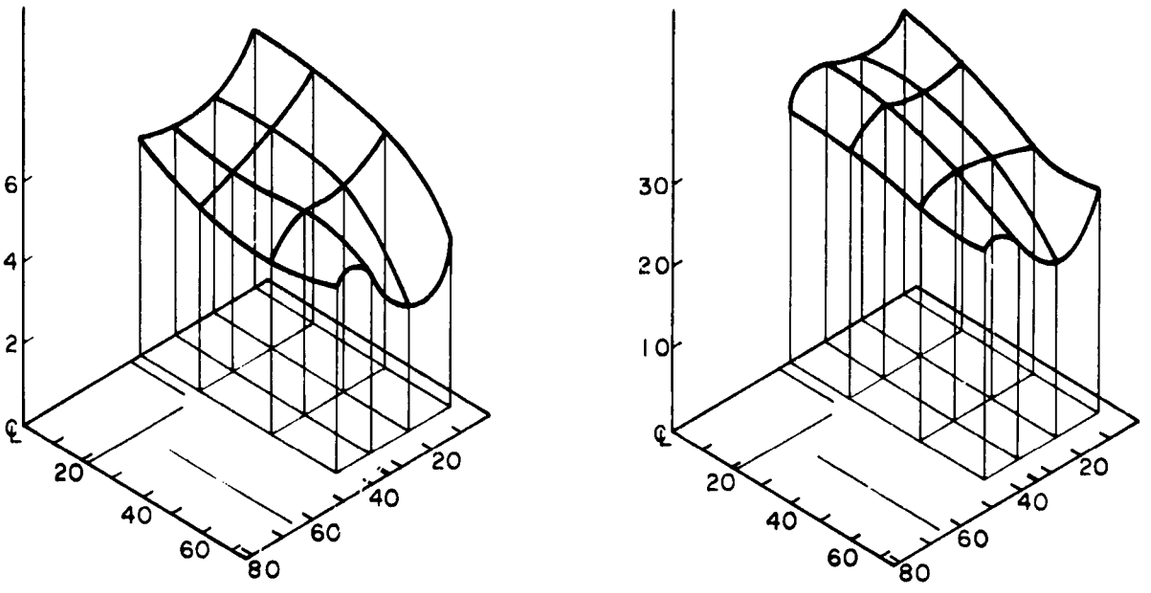

A. UPSTREAM ANODE POSITION

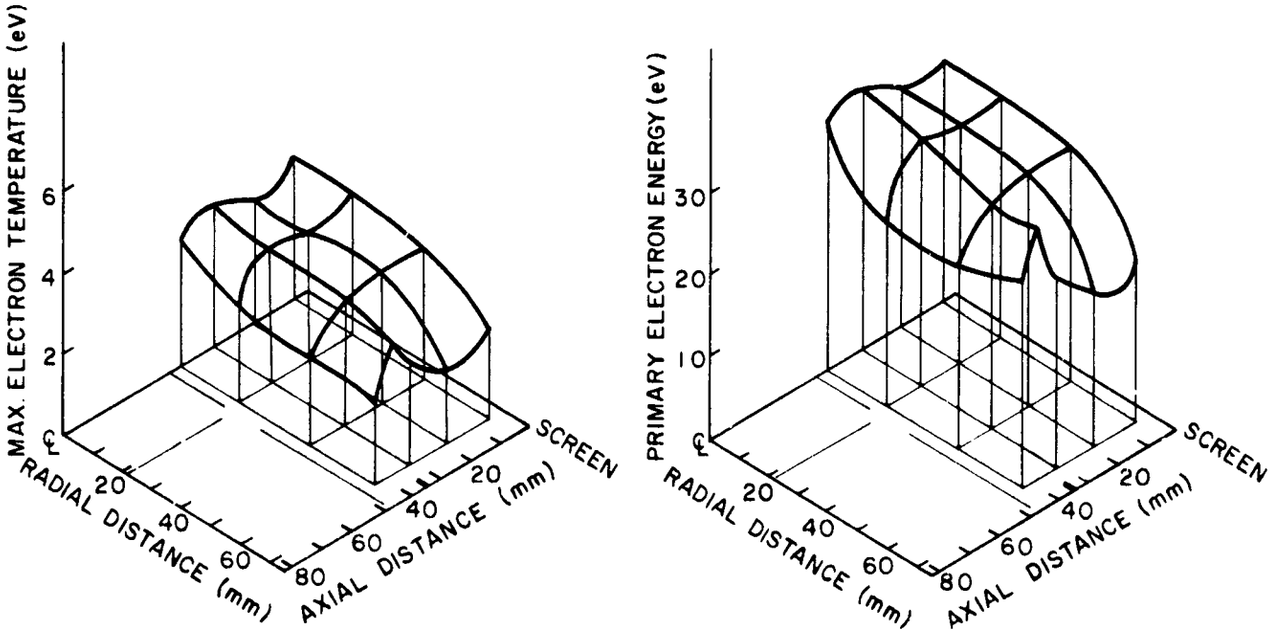

B. DOWNSTREAM ANODE POSITION

EFFECT OF REAR ANODE LOCATION

ON ELECTRON TEMPERATURE AND ENERGY (L/D = 0.23)

FIGURE 20

a large reduction in the electron temperature occurred throughout the discharge chamber as a result of moving the rear anode to the downstream location. The reduction in electron temperature is thought to be due to a depletion of the high energy (large cyclotron radius) electrons in the Maxwellian tail as the anode is moved close to the magnetic field lines in the upstream end of the discharge chamber. The downstream movement of the anode also caused a reduction in the primary electron energy level. The primary energy effect appears to be more localized than the temperature effect probably due to the longer path length of the primary electrons for Coulomb collisions. The effect of anode position on the electron temperature and energy as described above was found to be the same for all chamber length-to-diameter ratios and both magnetic field geometries.

Langmuir probe data were used to calculate the volume averaged plasma properties in the manner suggested in the Doubly Charged Ion Production section of this report. The results are presented in Table III for all three chamber lengths, both magnetic field geometries, and both rear anode positions. The average plasma properties can be used to explain most of the double-to-single ion density ratio trends of Figures 16 and 17. For instance, the Maxwellian electron temperature, primary electron energy, and volume-to-surface area ratio are almost invariably decreased as the anode is moved to the downstream position. This should result in a reduction in the double-to-single ion density ratio and the experimental results of Figures 16 and 17 confirm this for all cases except the short chamber cusped field configuration. The variation of the experimentally determined double-to-single ion density ratio with discharge chamber length and magnetic field geometry is not as easily correlated with the average quantities presented in Table III. Those cases which seem inconsistent are probably due to differences

TABLE III. VOLUME AVERAGED PLASMA PROPERTIES

		Cusped Magnetic Field		Divergent Magnetic Field	
		Anode Position		Anode Position	
L/D	Property*	Upstream	Downstream	Upstream	Downstream
0.23	T_m (eV)	4.7	3.05	4.9	3.8
"	ε_p (eV)	29.4	28.0	29.7	27.6
"	$n_p x10^{-10} (cm^{-3})$	0.94	0.76	1.03	0.92
"	$n_m x10^{-10} (cm^{-3})$	26.8	28.1	26.8	31.7
"	V/A (cm)	1.65	1.35	1.51	1.0
0.30	T_m (eV)	4.8	3.3	5.6	3.9
"	ε_p (eV)	28.7	27.1	28.9	26.7
"	$n_p x10^{-10} (cm^{-3})$	0.62	0.77	0.83	0.99
"	$n_m x10^{-10} (cm^{-3})$	26.2	32.7	24.3	29.4
"	V/A (cm)	1.82	1.63	1.48	1.36
0.53	T_m (eV)	3.1	3.1	3.5	3.4
"	ε_p (eV)	22.5	24.1	27.0	19.8
"	$n_p x10^{-10} (cm^{-3})$	0.56	0.47	0.57	0.58
"	$n_m x10^{-10} (cm^{-3})$	28.6	27.2	27.7	33.5
"	V/A (cm)	1.93	1.93	1.14	0.81

* T_m - Maxwellian Electron Temperature

ε_p - Primary Electron Energy

n_p - Primary Electron Density

n_m - Maxwellian Electron Density

V/A - Volume-to-Surface Area Ratio of Primary Electron Region

in the plasma density existing near the screen grid. The data of Table III also show a general tendency for primary electron energies and densities to increase as the length-to-diameter ratio is decreased.

Double Ion Correlation

Double-to-single ion current ratios have not been measured at high propellant utilization due to thermal expansion and subsequent shorting of the grids which occurs when the thruster is operated for extended periods at high power conditions. The double-to-single ion current ratios which have been measured were obtained at a propellant utilization of about 85% and were found to be less than 8%. Performance measurements at higher power conditions suggest the ratio may go as high as 30% at a relatively modest discharge power loss of 600 eV/ion. This large apparent double ion ratio observed at the higher power conditions is observed with the cusped magnetic field geometry but not the divergent field geometry (see Figure 15).

Some justification of the assumption that the cusped field thruster produces a large fraction of double ions at the higher power and beam current conditions can be made on the following basis. The shifts in the performance curve observed with the typical cusped field thruster as propellant flow rate is increased is illustrated in Figure 21. The performance curve at low flow rate resembles that of a properly designed discharge chamber. That is, the discharge losses are fairly constant until the "knee" of the curve is reached whereupon the losses rise suddenly and a maximum propellant utilization is reached at a high power condition. Increasing the propellant flow rate causes the performance curve to shift toward a higher maximum propellant utilization. As the flow rate is increased even further the steep portion of the curve begins to flatten out and propellant utilizations

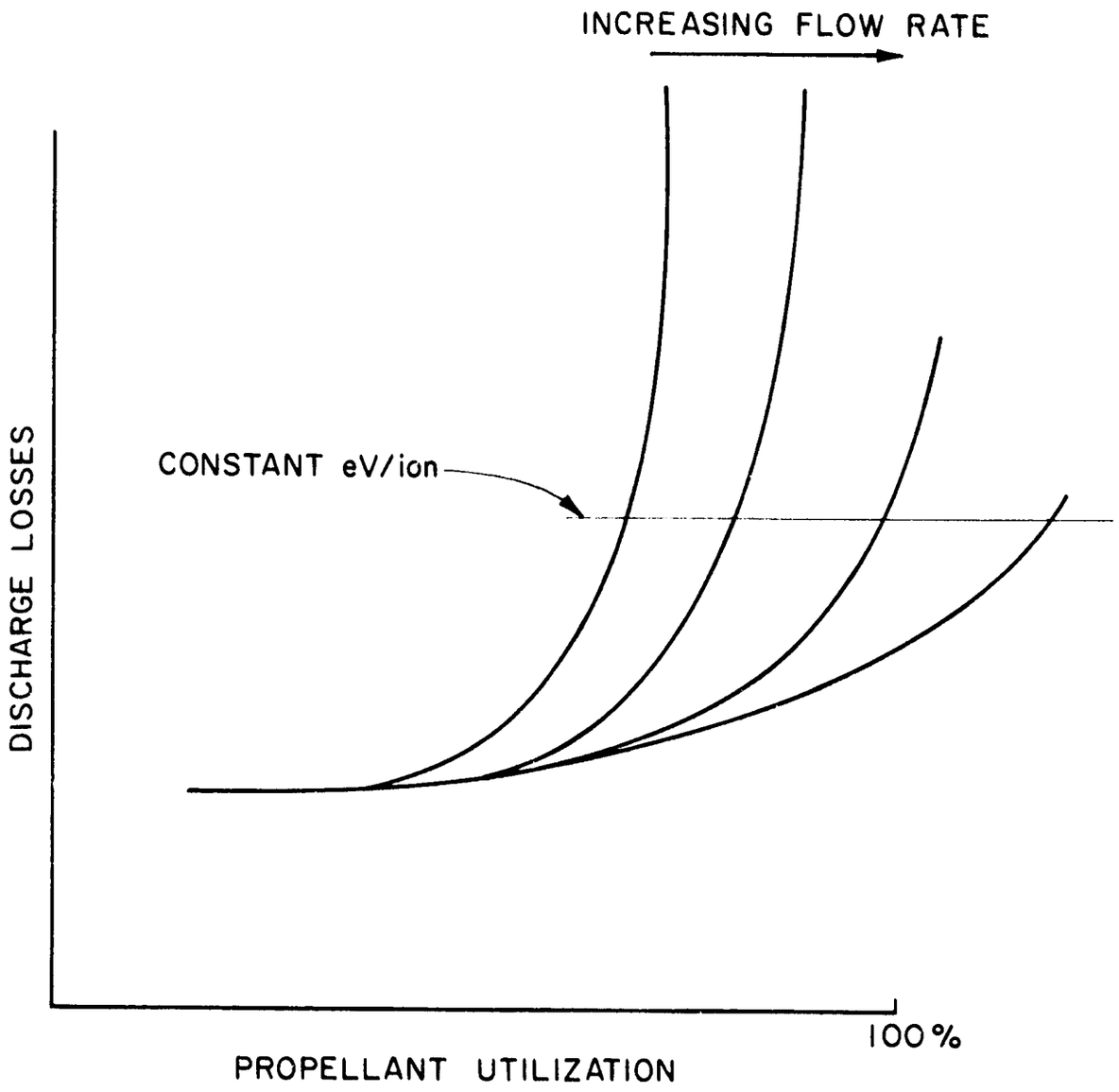

TYPICAL CUSPED FIELD THRUSTER PERFORMANCE CURVES

FIGURE 21

of over 100% are calculated at the high flow rate conditions.

At a given discharge power one can evaluate the neutral loss rate from a performance curve obtained at a low propellant flow rate where the double ion density is assumed to be negligible. Then assuming a constant neutral loss rate at this discharge power in accordance with Kaufman's model[16], the maximum propellant utilization can be calculated for each flow rate by the expression

$$\eta_{max} = 1 - \dot{m}_{loss}/\dot{m} \tag{2}$$

where η is the propellant utilization, $\dot{m}$ the total propellant flow rate, and $\dot{m}_{loss}$ the neutral loss rate. From this maximum propellant utilization and the measured utilization, one can calculate a double-to-single ion density ratio assuming the difference in utilizations is due to the presence of double ions. The double-to-single ion density ratio can be expressed in terms of the measured and maximum utilizations by the expression

$$\frac{n^{++}}{n^{+}} = \frac{1 - \eta_{max}/\eta}{\sqrt{2}(2\eta_{max}/\eta - 1)} \tag{3}$$

If the double ion ratios calculated in this manner correlate well with the theoretical dependence on beam current, one can argue that the assumptions made in arriving at the density ratio are valid and that the excessive measured propellant utilizations are due to double ions.

The double-to-single ion density ratio can be shown[11] to a good approximation to be proportional to the electron number density. The electron density n_e is related to the single and double ion densities

n^+ and n^{++} by the conservation of charge and thus one can write the following relationship

$$\frac{n^{++}}{n^+} \propto n_e = n^+ + 2n^{++} . \qquad (4)$$

The beam current can be expressed in terms of the ion densities by the expression

$$I_B \propto n^+ + 2\sqrt{2}\, n^{++} . \qquad (5)$$

For double-to-single ion density ratios less than about 12% the quantities $n^+ + 2n^{++}$ and $n^+ + 2\sqrt{2}\, n^{++}$ differ by less than about 6% and to a good approximation one can write

$$\frac{n^{++}}{n^+} \propto I_B . \qquad (6)$$

That is, the double-to-single ion density ratio should vary almost linearly with beam current at a given discharge power (eV/ion) as one varies mass flow rate.

Double-to-single ion density ratios were calculated from performance data obtained at various flow rates by the use of Equations 2 and 3. The calculations were made for discharge chamber length-to-diameter ratios of 0.23 and 0.50 at a discharge power level of 600 eV/ion. The double-to-single ion density ratios obtained in this manner are presented as a function of beam current in Figure 22. The linear variation of the double-to-single ion density ratio with beam current suggests the assumptions made in arriving

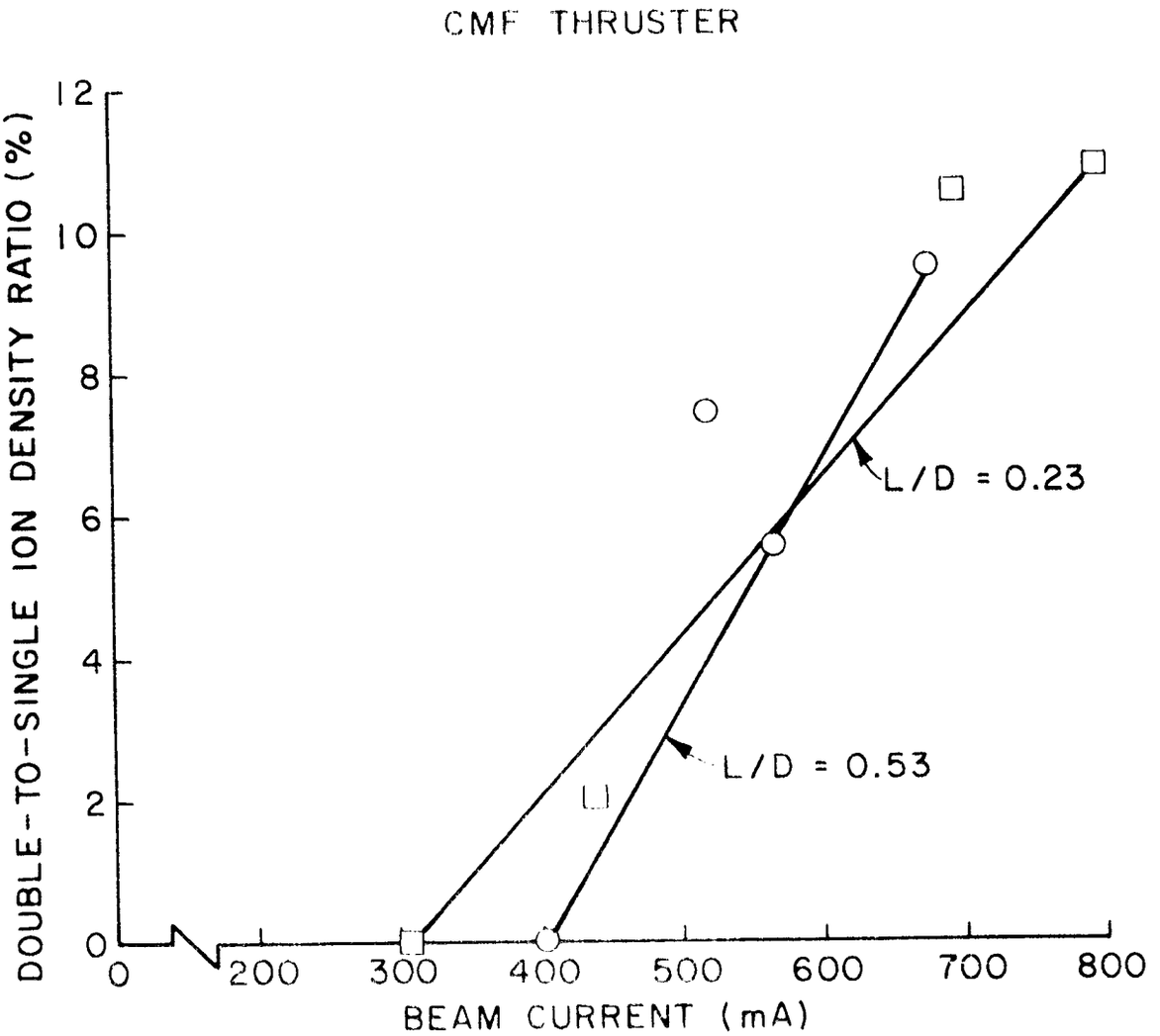

CALCULATED DOUBLE-TO-SINGLE ION DENSITY RATIO

FIGURE 22

at these results were valid and that the excessive propellant utilizations measured at the high beam currents are due to the existence of significant double ion populations in the cusped field discharge chamber.

Conclusions

Both the beam profile flatness and thruster performance are improved as the discharge chamber of the single cusp magnetic field thruster is reduced to 63% of the SERT II thruster length. The beam profile flatness parameter of this short discharge chamber is 0.70 when operating at 85% propellant utilization (730 mA total flow) and a discharge loss of 250 eV/ion. This represents a 40% increase in beam flatness over the SERT II thruster at approximately the same propellant utilization and discharge power level (eV/ion). Throttling the thruster to a 460 mA flow rate results in an increase in the beam profile flatness parameter to a value of 0.82.

The measured double-to-single ion density ratio for the short chamber cusped magnetic field geometry is 2.4% which is slightly less than the value obtained for the SERT II thruster at comparable operating conditions. The double-to-single ion density ratio is thought to increase to much higher values at higher power conditions, but measurements to support this theory have not been made at the present time.

The divergent magnetic field geometry was found to have a less uniform beam profile than the cusped field geometry for all three chamber lengths. However, the beam profile of the divergent field geometry was considerably more uniform than the SERT II thruster profile.

The position of the rear anode was found to have a significant effect on the Maxwellian electron temperature. Movement of the rear anode in the downstream direction resulted in a significant reduction in the double-to-

single ion density ratio due to reductions in the chamber volume-to-surface area ratio, the Maxwellian electron temperature and the primary electron energy.

ION OPTICS STUDY

Graeme Aston

An accurate knowledge of the ion beam half angle (α_{max}) is of considerable importance when applying ion propulsion devices to actual mission situations. This angle, which defines the cone confining the expelled ions, should be small to maximize the thrust at a given beam current. It would be advantageous to know, not only what accelerator geometries produce the lowest half angles, but also how the half angle could be expected to vary as the perveance of a grid system varied due to power variations during a mission.

Computer solutions are available, which predict ion optical trends as a function of grid and accelerating voltage parameters, for a single hole geometry.[17] This experimental ion optics study was instigated to verify the accuracy of these solutions by comparing them with results obtained from actual single hole grid sets. Performance expected with typical multiaperture grids was then investigated by using a nineteen hole hexagonal array of approximately one cm^2 area. This was assumed adequate to model the adjacent hole interactions found in full size grid systems.

Parameter Definitions

Throughout this report the geometrical grid parameters and symbols used are consistent with those employed by Kaufman[17] and illustrated in Figure 23.

These are listed below:

t_g = separation between screen and accelerator grids

d_a = diameter of accelerator aperture(s)

d_s = diameter of screen aperture(s)

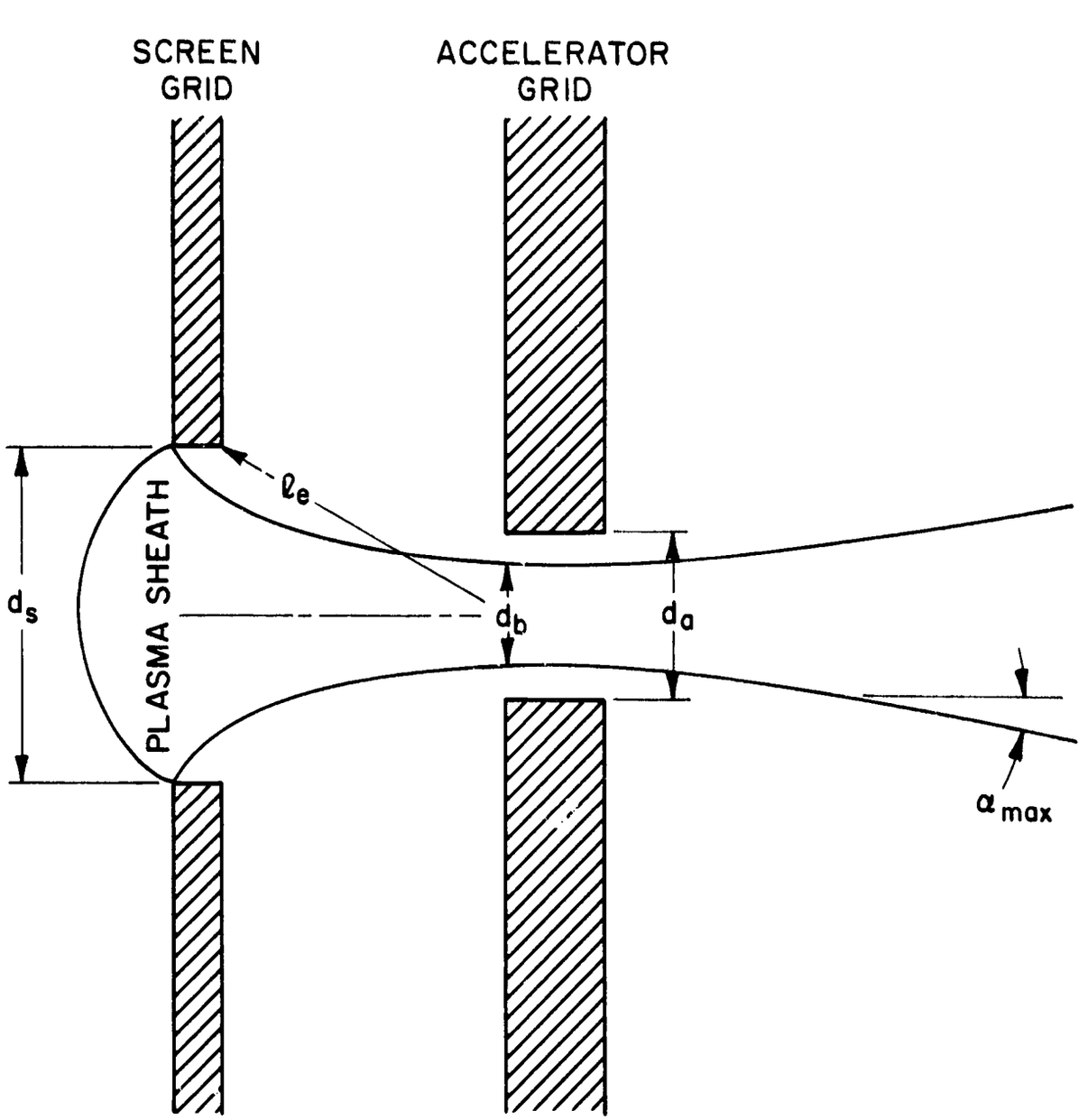

GRID SYSTEM PARAMETERS

FIGURE 23

t_a = thickness of accelerator grid

t_s = thickness of screen grid

z_e = Kaufman effective acceleration length

defined by:

$$z_e^2 = z_g^2 + \left(\frac{d_s}{2}\right)^2$$

α_{max} = maximum ion beam half angle.

Throughout this section perveance calculations were normalized by multiplying with the ratio $\left(\frac{z_e}{d_s}\right)^2$ and grid parameters were nondimensionalized with the screen aperture diameter (d_s).

Apparatus

A simple, mildly divergent field, 8 cm electron bombardment ion source was constructed and operated on argon propellant for these tests. Tungsten wire filaments were used as both the main and neutralizer cathode emitters. The magnetic field was derived from a long solenoidal winding extending the length of the discharge chamber, with a single Helmholtz coil winding positioned at the chamber's rear. The geometry was such that the field at the front of the discharge chamber was 60% that of the rear. A cylindrical anode was employed and stainless steel construction was used throughout.

The screen and accelerator grids used were fabricated from thin sheet graphite. This material was easy to machine and was available as a stock item in the desired thicknesses. Five centimeter square plates containing the grid patterns were positioned on a masking plate which covered most of the downstream end of the discharge chamber. The calculated variation in ion density across the area of these grid patterns was less than 5 . Variable separation of the grids was achieved by using thin mica washers which were replaced after each data run to avoid electrical breakdown and

large leakage currents.

All tests were conducted in a 30 cm diameter pyrex bell jar pumped by a mechanical pump in series with a 10 cm diameter oil diffusion pump. The power supplies and associated volt meters and ammeters were connected to the source in the manner shown on Figure 24A. The argon flow rate into the source was sensed by a Hastings flow meter and displayed on a digital readout.

Ion current density profiles were measured in the ion beam using a movable probe rake composed of twenty 0.70 cm x 1.43 cm stainless steel Faraday probe sensors whose output was sensed by the system shown in Figure 24B. The probe rake position relative to the thruster and the details of its construction are illustrated in Figure 25. Once the source had reached stable operating conditions, the rake was moved through the ion beam and brought to rest at that location where the current sensed by one of the central probes peaked out. Current to each of the twenty probes was then measured to determine the ion beam profile.

Operating Conditions

In order that as few variables as possible entered into the final results, the ion source was operated at the following conditions for all tests:

Arc Voltage	40 V
Magnet Current	7 A
Neutralizer Coupling Voltage	0 V
Probe Bias Voltage	-30 V
Propellant Flow Rate	0.50 mA - single aperture tests 5.94 mA - multiaperture tests

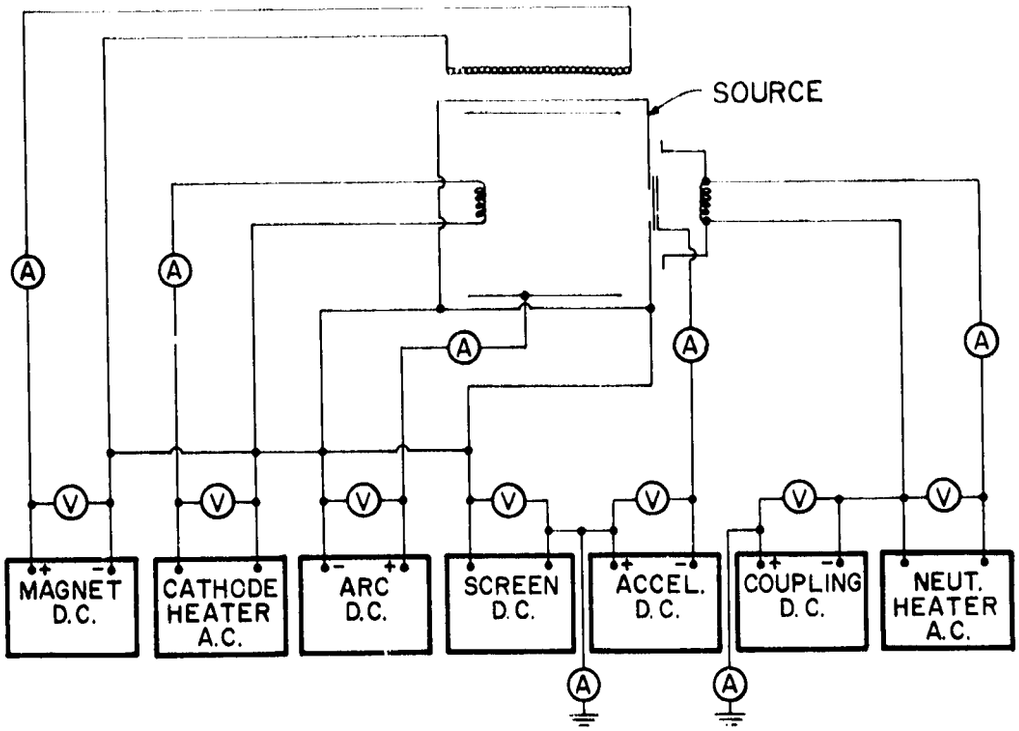

A. POWER SYSTEM SCHEMATIC

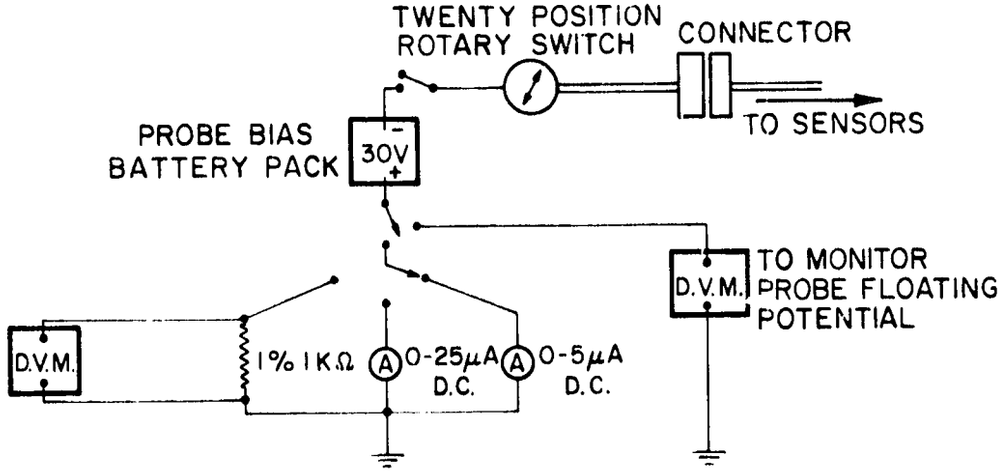

B. FARADAY PROBE CURRENT MEASUREMENT SYSTEM

ION OPTICS STUDY

POWER AND MEASUREMENT SYSTEMS

FIGURE 24

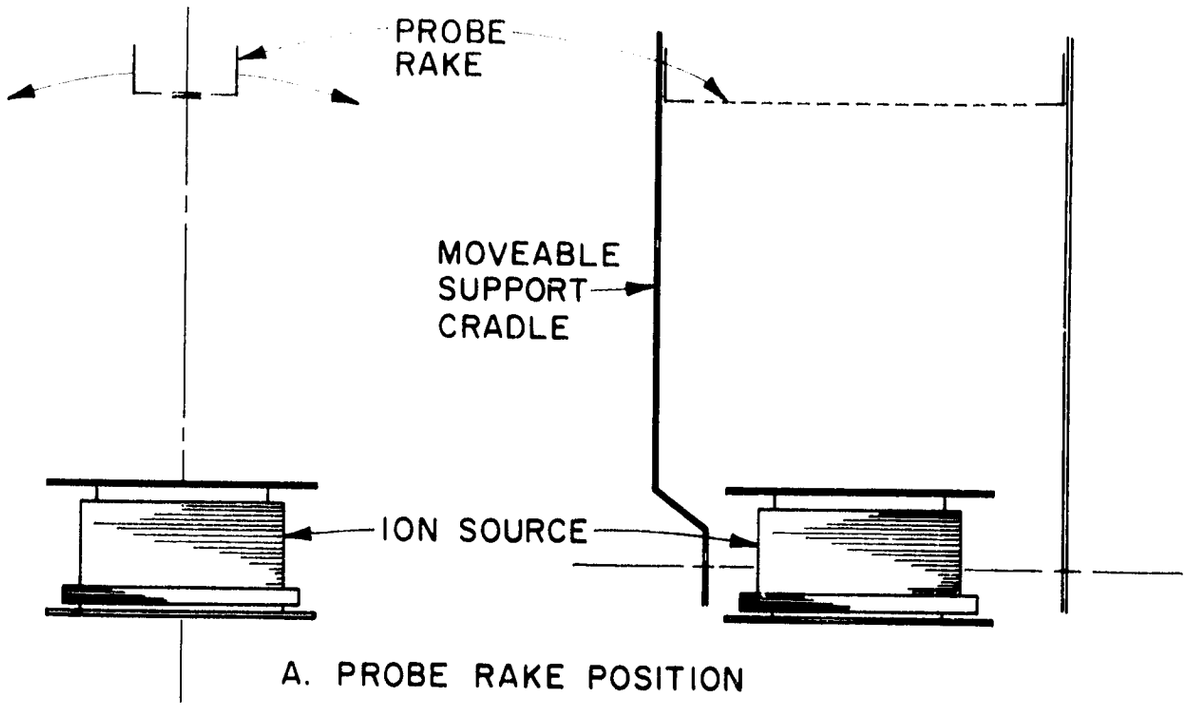

A. PROBE RAKE POSITION

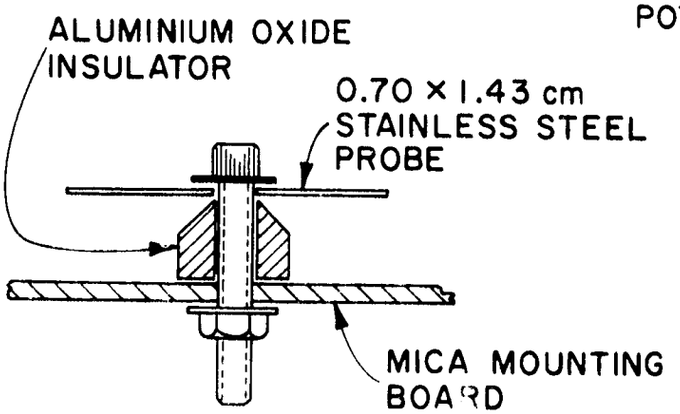

B. PROBE CONSTRUCTION

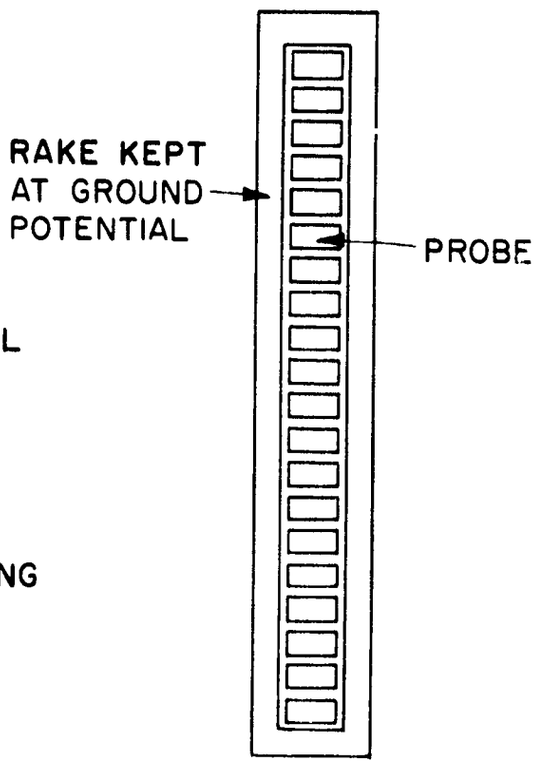

C. PROBE POSITION ON RAKE

FARADAY PROBE RAKE CONSTRUCTION

FIGURE 25

Grid Voltages

Single Aperture Tests					Multiaperture Tests				
V_{screen}	$\|V_{accel}\|$	V_{net}	V_{tot}	$R = \frac{V_{net}}{V_{tot}}$	V_{screen}	$\|V_{accel}\|$	V_{net}	V_{tot}	$R = \frac{V_{net}}{V_{tot}}$
530	270	575	845	0.680	255	300	555	600	0.500
600	257	645	902	0.715	375	180	555	600	0.700
710	190	755	945	0.798	495	60	555	600	0.900

where $V_{net} = V_{screen} + V_{sheath} + V_{arc}$, $V_{tot} = V_{net} + |V_{accel}|$ and V_{sheath} was assumed to be 5 volts. Beam current was controlled for the tests by adjusting the cathode current and hence its emission. From this beam current and the acceleration voltage and grid geometrical factors the normalized perveance was calculated. Through the course of the data collection the average bell jar pressure was in the low 10^{-5} torr range for the single aperture grid tests and the middle to high 10^{-5} torr range with the multiple aperture ones.

Ion Beam Measurements

Ion beam profiles measured with the Faraday probe rake show two ion populations are present in the beam--high velocity beam ions and charge exchange or background ions. These two populations overlap producing an ion beam profile like the one shown in Figure 20A and it is necessary to separate them so the beam ion trajectories can be defined. Once the true beam ion profile has been identified, the half angle of the beam can be determined. In the present case the object was to select this half angle in such a way that it defined a conic frustrum, originating at the grids and terminating at the probe rake, which enclosed 99% of the beam current.

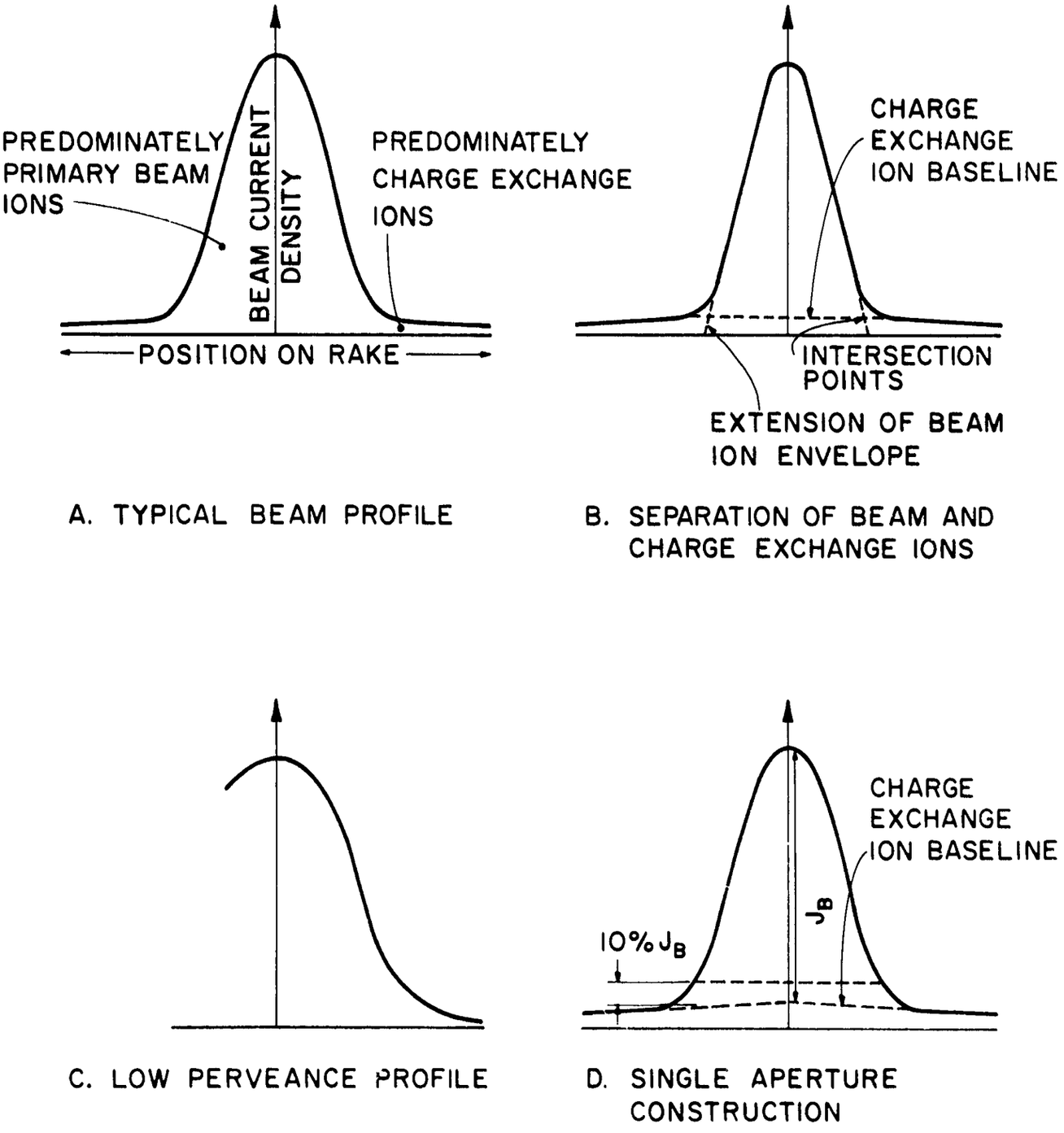

A. TYPICAL BEAM PROFILE

B. SEPARATION OF BEAM AND CHARGE EXCHANGE IONS

C. LOW PERVEANCE PROFILE

D. SINGLE APERTURE CONSTRUCTION

ION BEAM PROFILE INTERPRETATION

FIGURE 26

Separation of the beam and charge exchange ion currents was accomplished by calculating the charge exchange current to each probe and subtracting it from the measured current to that same probe. The charge exchange ion current density was calculated as twice the product of the ion charge, Bohm velocity[18] and charge exchange ion density determined from Kaufman's model.[19] The factor of two was incorporated into this calculation because it yielded a current density equal to the measured charge exchange current density at locations far from the ion beam centerline. The beam ion envelope line was then extended in the manner suggested by Figure 26B to intersect the charge exchange baseline and define points at the probe rake location which were used to calculate the desired half angle. As a check on this procedure several current density profiles were integrated along the charge exchange baseline out to these intersection points and this yielded a current that was 90% of the measured beam current. This technique for half angle determination was applied to all of the multi-aperture data. Consistent results were obtained over the middle to high perveance range of operation, however at the lower perveance conditions some scatter was evident. In this operating regime a linear extrapolation did not satisfactorily define the primary ion beam region because of the poor focusing of the accelerator system at the low perveances. As a result the corresponding beam profile took on a pronounced bowed appearance, like that illustrated in Figure 26C.

For single aperture profiles it was found that profiles could be evaluated at all perveance conditions by simply drawing a line at 10% of the beam beam current density above the charge exchange baseline as shown in Figure 26D. Using the intersection of this line with the profile envelope as the points at which to measure the half angle of a

conic frustrum was shown to enclose 90% of the beam current consistently.

The diameter of the ion beamlets emanating from a grid pair was also investigated. This was accomplished with a given single aperture grid pair by increasing the beam current until a sudden increase in accelerator impingement current was observed. The onset of this increase corresponded to the beam current and hence perveance at which the beamlet diameter was equal to the accelerator aperture diameter. The test was repeated with different accelerator aperture diameters to obtain the variation in beamlet diameter with perveance.

The increase in impingement current with beam current at the onset of direct impingement was less pronounced with the multiple aperture grid sets than it was with the single hole geometry; making a beam current determination at the transition point more arbitrary. To circumvent this difficulty and produce consistent results, the impingement current was recorded over the range of beam current (perveance) variation. Plotting impingement current against perveance and extrapolating the straight line portion of the curve, a baseline impingement current was obtained. The start of direct impingement was said to occur at the beam current where the actual curve had departed from the baseline by an amount equal to fifty percent of the baseline current. The beamlet diameters were therefore equated to the accelerator hole diameter at this perveance condition.

Results

The variation in ion beam half angle as a function of normalized perveance for the single aperture grids is presented in Figure 27 with non-dimensionalized grid separation distance as a parameter. Symbols used on this figure are defined in Figure 23. Normalized perveance defined as

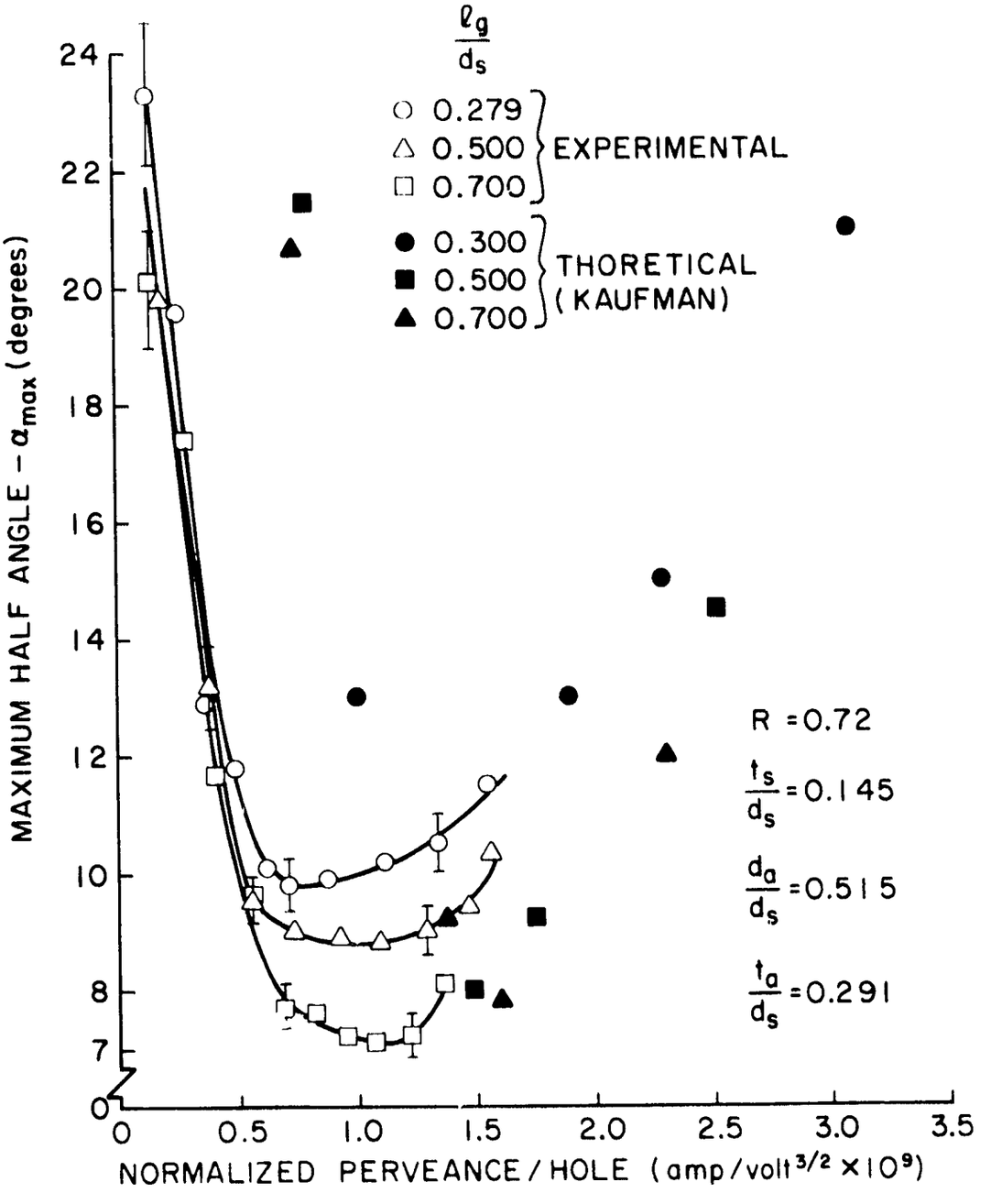

EFFECT OF GRID SEPARATION ON OPTICAL PERFORMANCE

SINGLE APERTURE GRIDS

FIGURE 27

$(J/V_t^{3/2})$ $(\ell_e/d_s)^2$ and determined by Child's law has a maximum value of 3.03×10^{-9} amp/volt $^{3/2}$ for singly ionized mercury. R in the figure is the ratio of net-to-total accelerating voltage. Open symbols shown on the figure correspond to experimental results and they are bracketed by error bars to indicate the accuracy of the results at various perveance levels. The numerical results obtained by Kaufman[17] for the single aperture case are shown for comparison as solid symbols. The single aperture experimental results are observed to follow the same general trends as those predicted by the computer program solutions, but the experimental curves are shifted to lower perveance values. The magnitude of the predicted minimum half angle agrees quite closely with that obtained experimentally. Unlike the theoretical solutions where this minimum occurs over a narrow perveance range, centered about a value of 1.5×10^{-9} amp/volt$^{3/2}$, the experimental results show a fairly broad minimum, located around a mean perveance of 1.0×10^{-9} amp/volt$^{3/2}$. It is also noteworthy that theoretical solutions could be obtained at perveances up close to the Child's law limit but the maximum perveance that could be achieved experimentally by increasing cathode emission and hence thruster ion density was considerably less.

Figure 28 shows the effect of the variation in accelerator grid aperture diameter on the half angle vs. perveance plot for the single aperture case. This figure shows that increasing the accelerator aperture diameter to a value approaching the screen aperture diameter facilitates operation at higher perveance conditions. The one data point at a perveance beyond the theoretical Child's law limit of 3.03×10^{-9} amp/volt$^{3/2}$ is noteworthy. This probably occurs because the plasma sheath position is not adequately modelled by the parameter ℓ_e used in the normalized perveance expression and defined in Figure 23

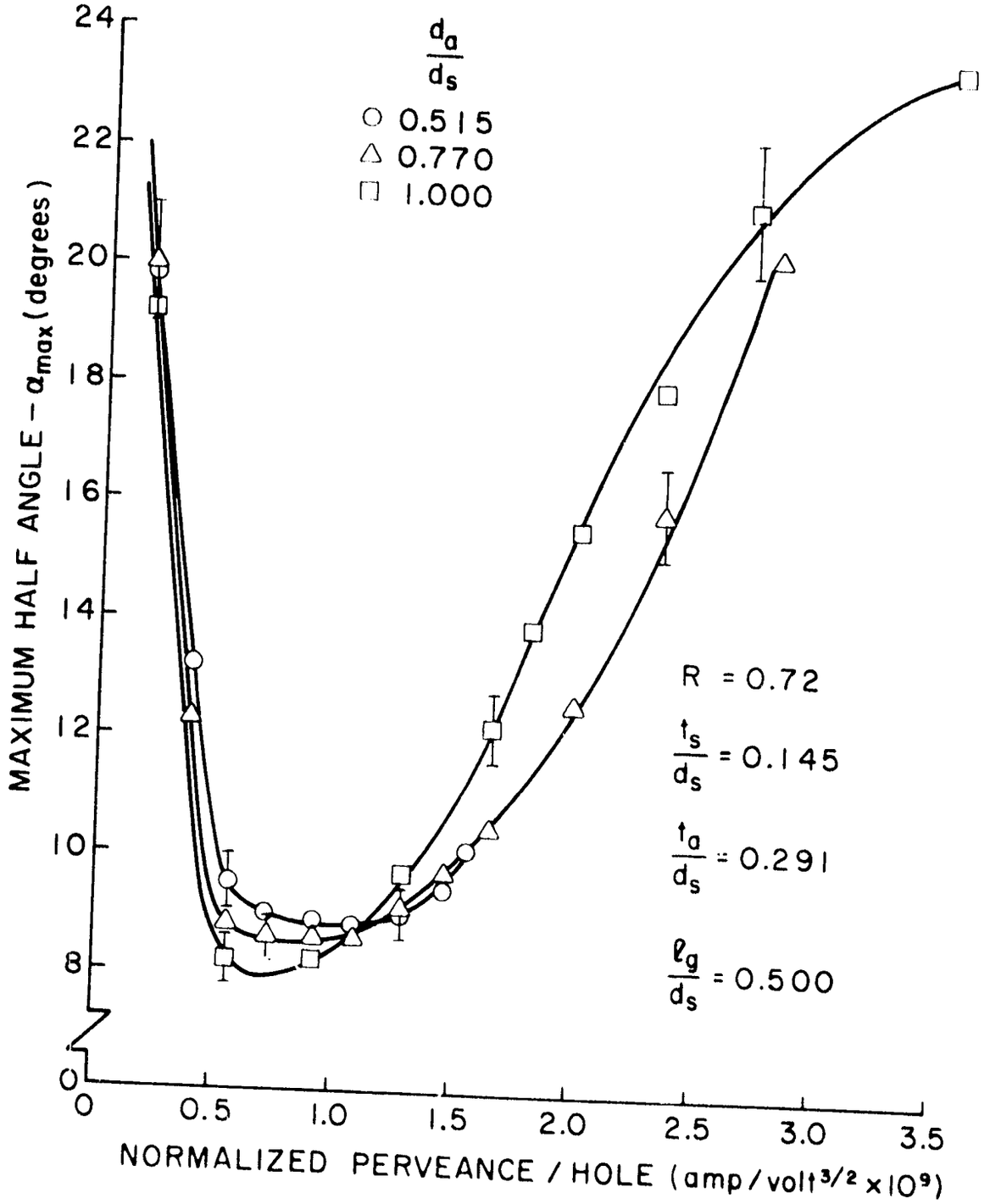

EFFECT OF ACCELERATOR APERATURE DIAMETER ON OPTICAL PERFORMANCE

SINGLE APERTURE GEOM.

FIGURE 3.3

Figure 29 shows the effect of screen grid thickness on the shapes of these curves is minimal for the single aperture case. The data presented in Figures 27 through 29 served the purposes of 1) verifying the adequacy of the computer ion optics solutions of reference [17] and 2) indicating what values of the geometrical variables would be of primary interest for the multiaperture experiments.

Results obtained with multiaperture grid sets which more closely model actual thruster grid sets are presented as Figures 30 through 32 as a function of the same variables and parameters as those used for the single aperture grid data. Interactions between adjacent holes which occur when the multiaperture grid sets are used, appear to result in no pronounced departures from the general trends found with the single hole geometries. Here again a fairly broad perveance range at the minimum half angle was observed to be centered about a normalized perveance value of about 1×10^{-9} amp/volt$^{3/2}$. The half angle did not reach such high values at low perveances as it did in the single aperture cases. This effect may be due however to errors in interpretation of the ion beam profiles at low perveance where the ion beam profiles were generally difficult to analyze.

Some general observations apparent from the multiple aperture work are:

1. Decreasing the grid separation ratio $\frac{g}{d_s}$ results in a dramatic increase in the magnitude of the minimum half angle but does not change the shape of the curves significantly.
2. Increasing the accelerator hole diameter at a constant $\frac{g}{d_s}$, results in a significant increase in the maximum obtainable perveance but does not change the minimum value of the half angle. An accelerator aperture to screen aperture diameter ratio of 0.5

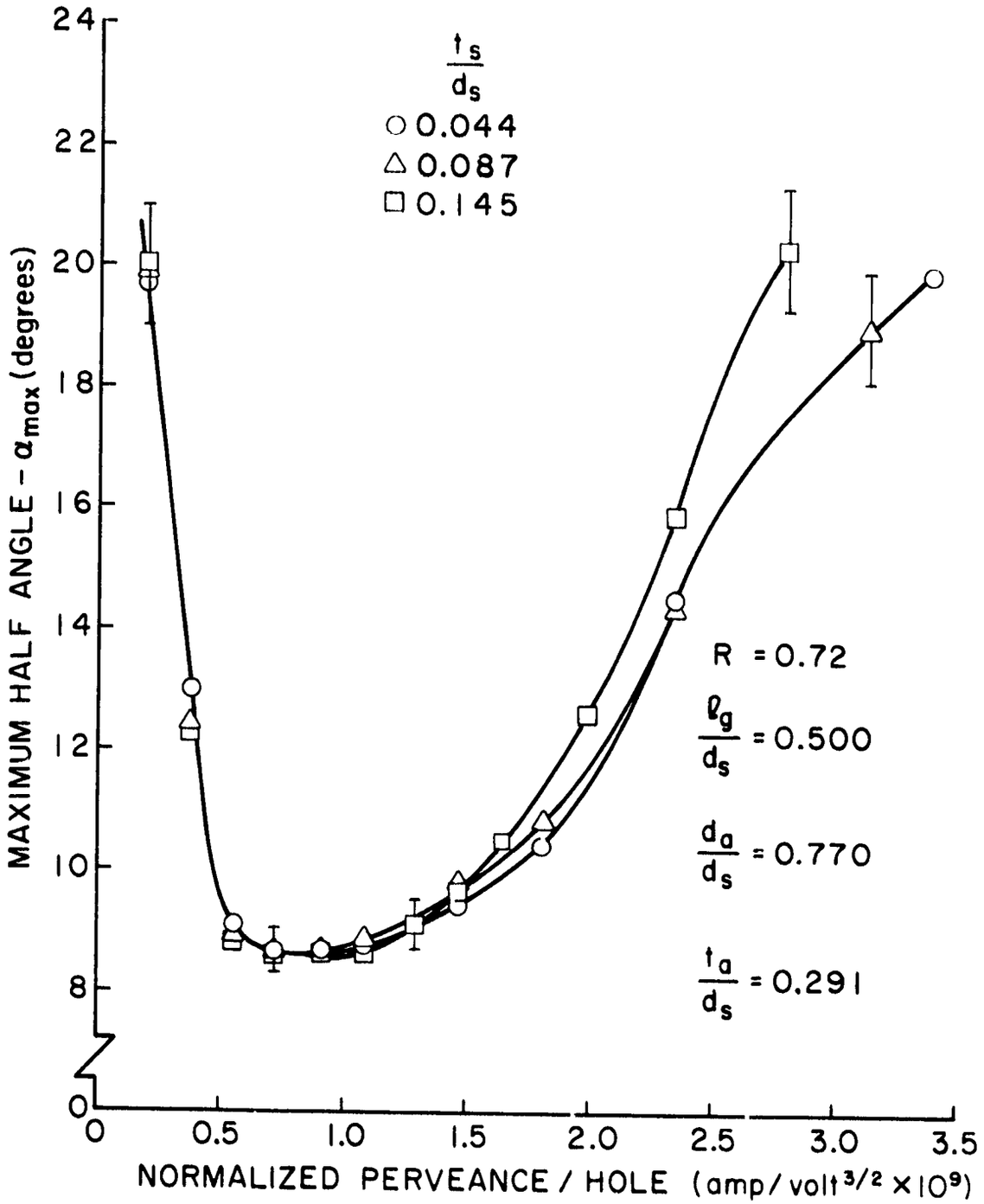

EFFECT OF SCREEN GRID THICKNESS ON OPTICAL PERFORMANCE

SINGLE APERTURE GRIDS

FIGURE 29

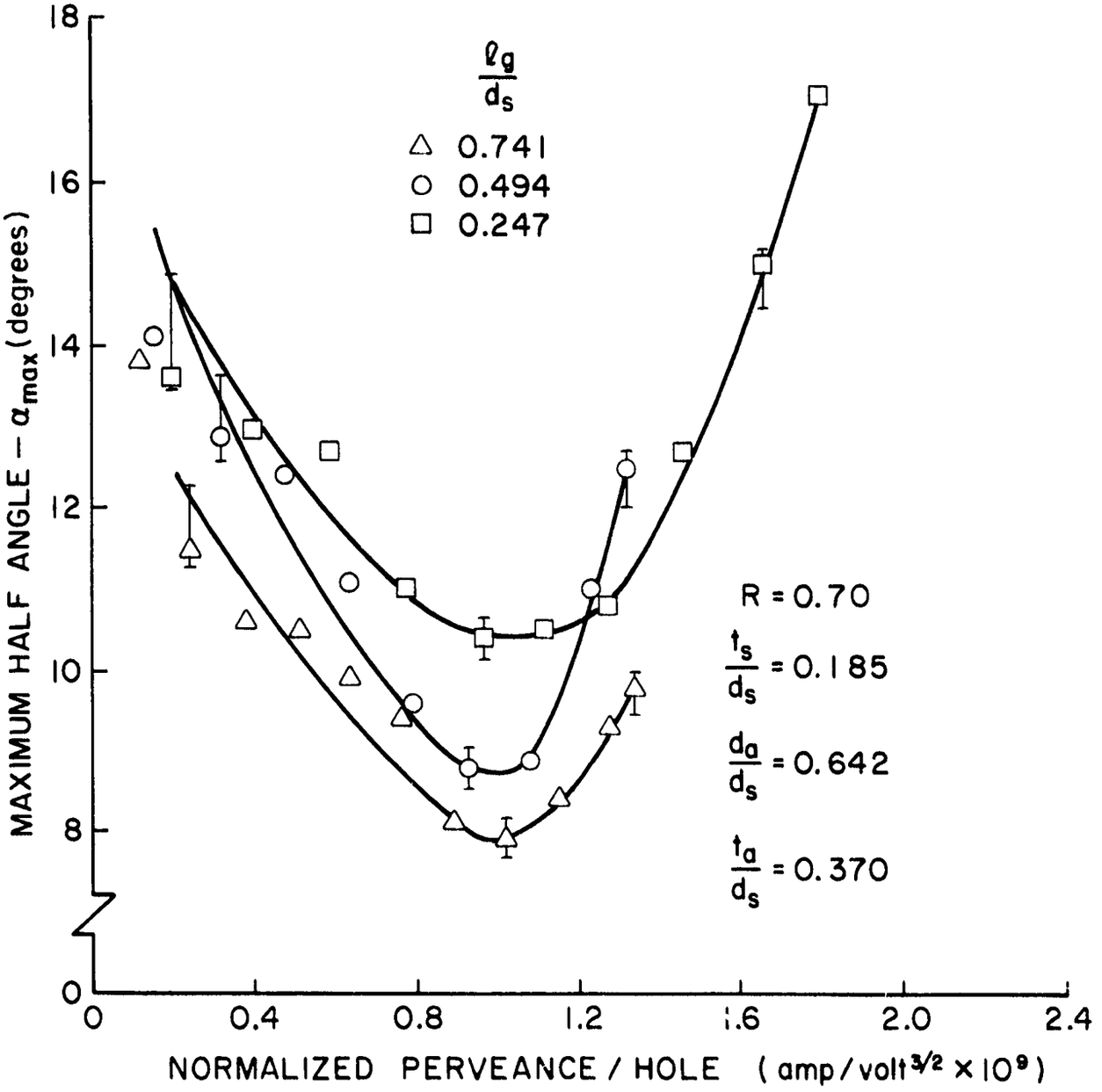

EFFECT OF GRID SEPARATION ON OPTICAL PERFORMANCE

MULTIAPERTURE GRIDS

FIGURE 30

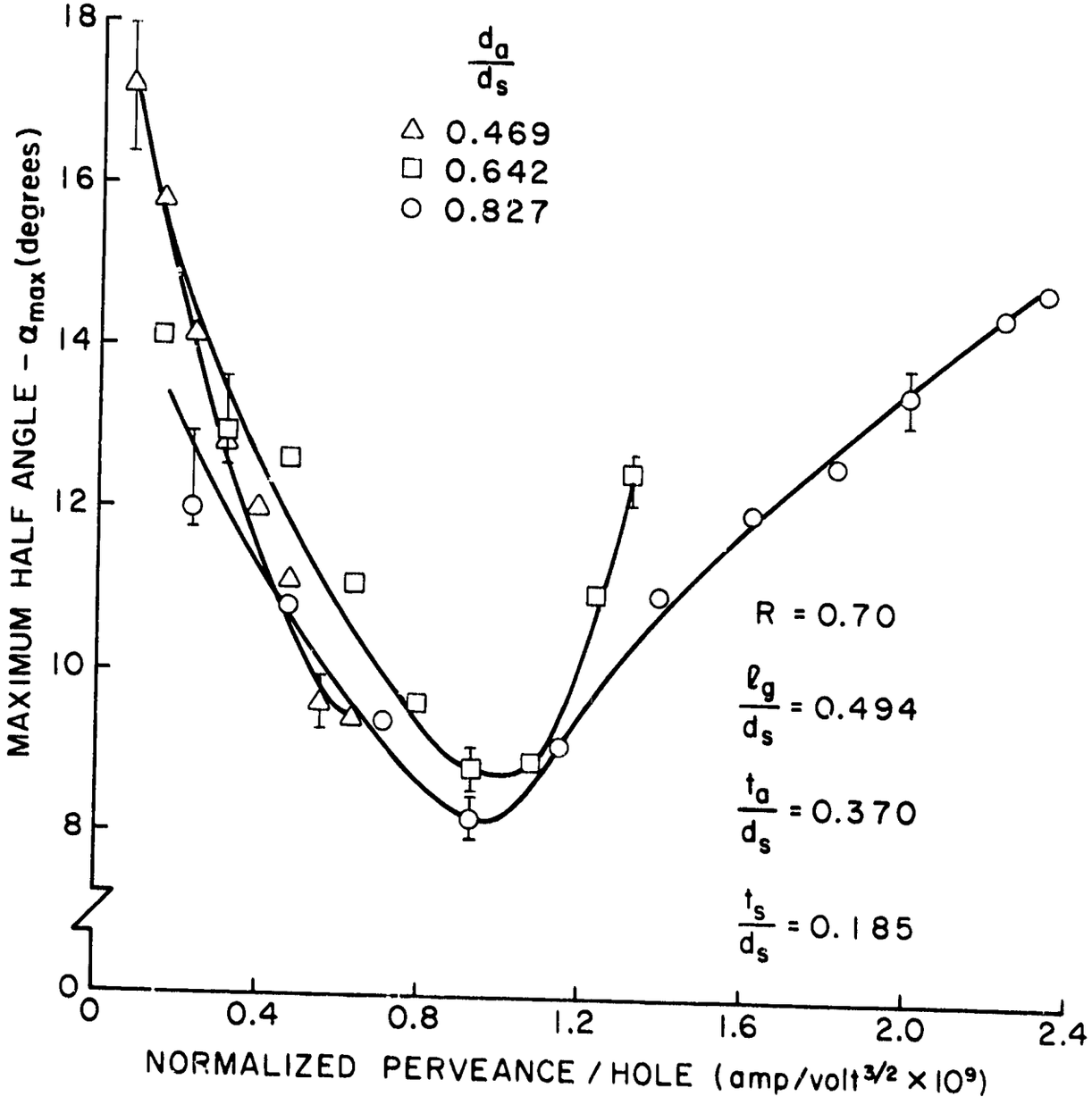

EFFECT OF ACCELERATOR APERTURE DIAMETER ON OPTICAL PERFORMANCE

MULTIAPERTURE GRIDS

FIGURE 31

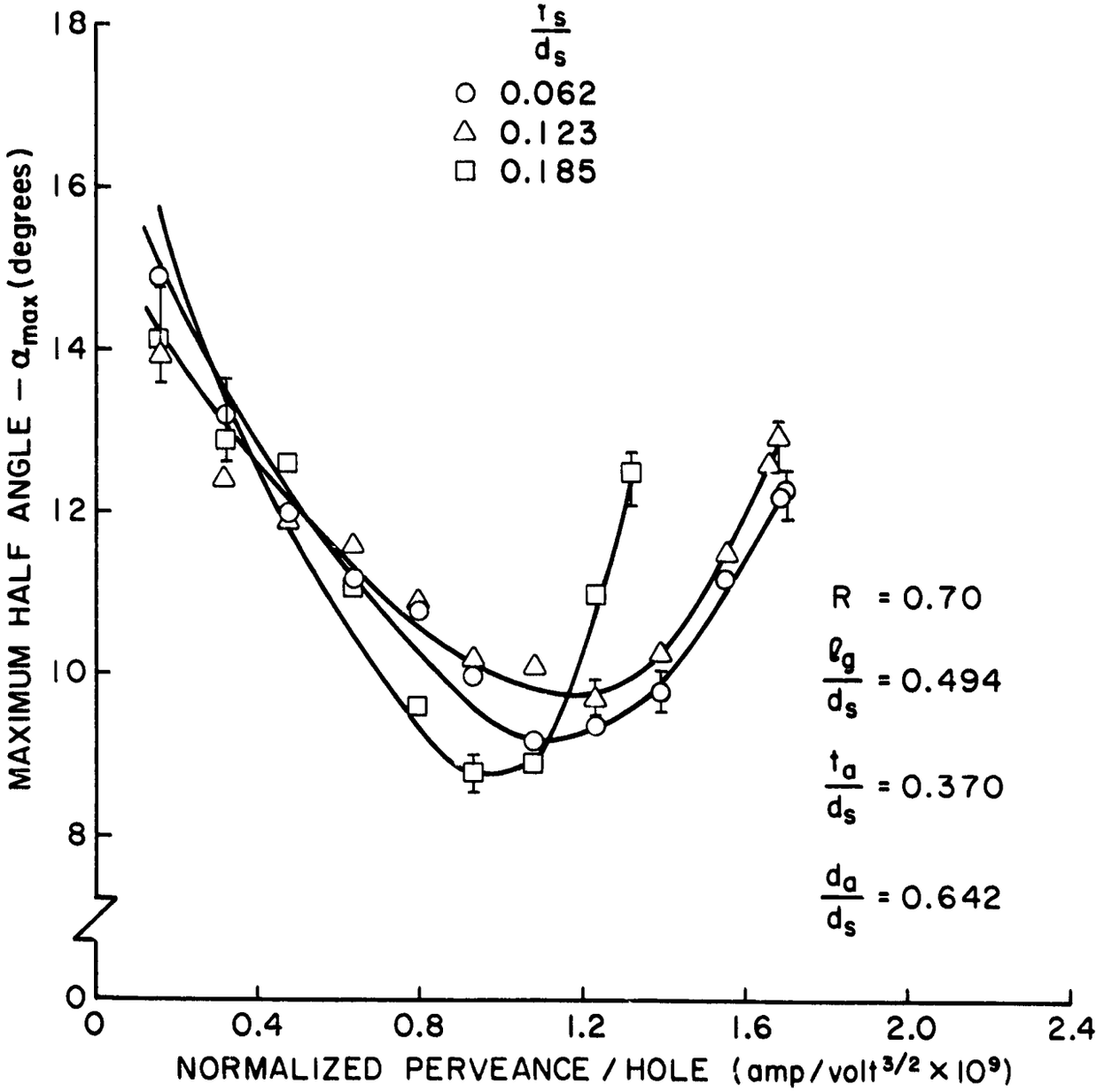

EFFECT OF SCREEN GRID THICKNESS ON OPTICAL PERFORMANCE

MULTIAPERTURE GRIDS

FIGURE 32

represents a limit below which the preveance capability of the grids is limited significantly.

3. Reducing the screen thickness for a constant $\frac{\ell_g}{d_s}$ and $\frac{d_a}{d_s}$, serves to broaden the minimum half angle region over a greater operating perveance range. An increase in the maximum obtainable perveance is also apparent, but a relatively small change is observed in the minimum half angles.

A point worth noting was that while a 30% reduction in $\frac{t_s}{d_s}$ from 0.185 to 0.123 substantially broadened the minimum half angle range and increased the maximum obtainable perveance, only a slight improvement was noticed in both of these trends as the screen thickness ratio was reduced an additional 50% to 0.062. This suggests reductions in screen thickness ratio below 0.12 are not effective. The reason for this apparent lower limit is associated with the position and shape of the plasma sheath relative to the screen grid. For thick grids, ion recombination at the inner wall of the screen hole acts to reduce the ion density in this region, which distorts the sheath shape, reducing focusing. However it is possible that if the screen is too thin, the sheath can no longer attach itself to it and takes up a detached position slightly downstream of the grid. This slight reduction in the actual value of ℓ_g, counteracts any focusing gains achieved by not having a distorted sheath edge.

Plots of the beam diameter ratio $\frac{d_b}{d_s}$ obtained with the single aperture configuration are presented in Figure 33. They exhibit correspondingly lower perveance values than those found in the computer solutions of Kaufman,[17] although the general trends agree. There is a marked difference, however, with the results for the multiple aperture grids shown in Figure 34. Unlike those of the single hole, the data spread for the three

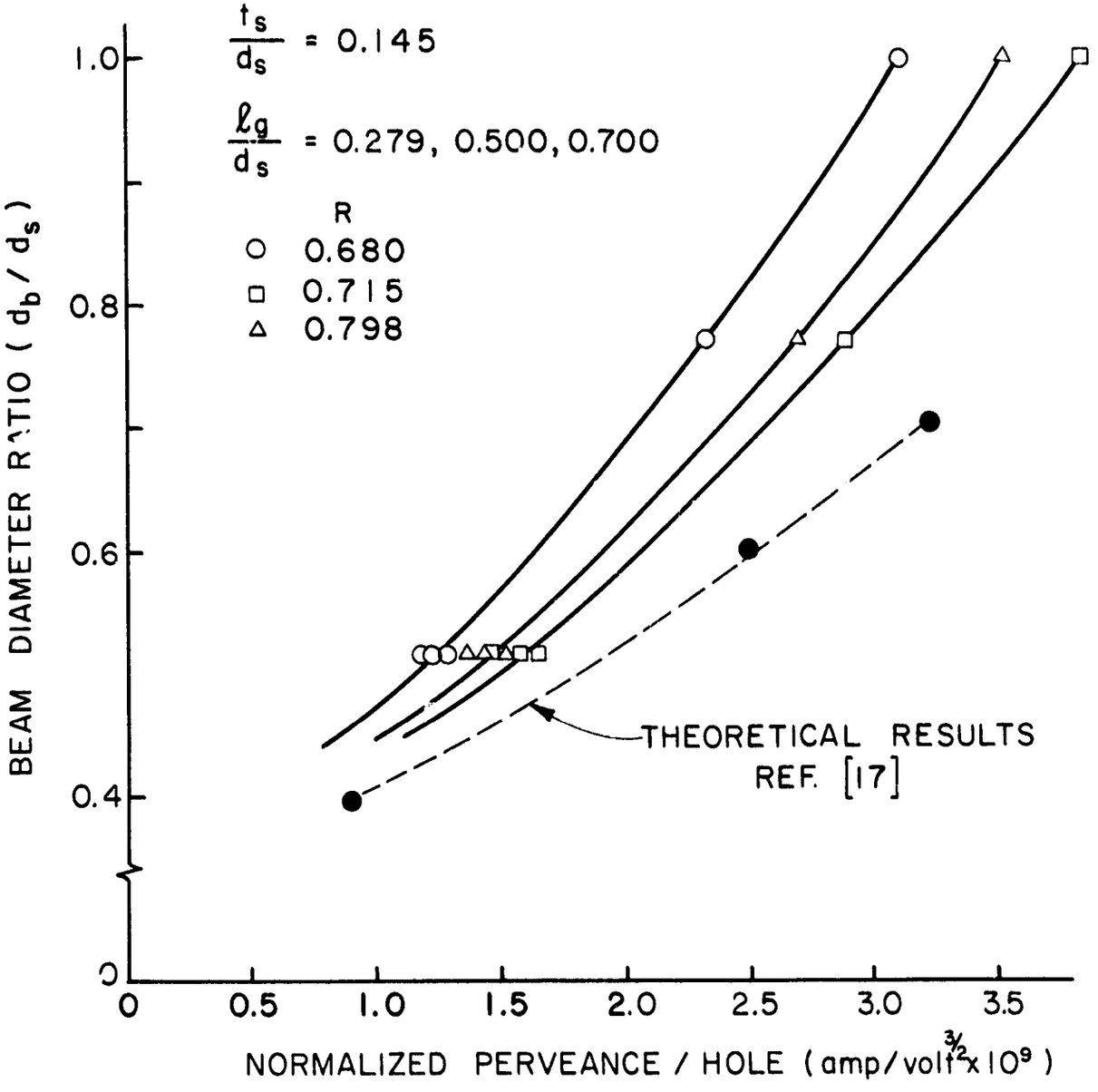

EFFECTS OF PERVEANCE AND NET-TO-TOTAL ACCELERATION VOLTAGE RATIO ON BEAMLET DIAMETER - SINGLE APERTURE GRIDS

FIGURE 33

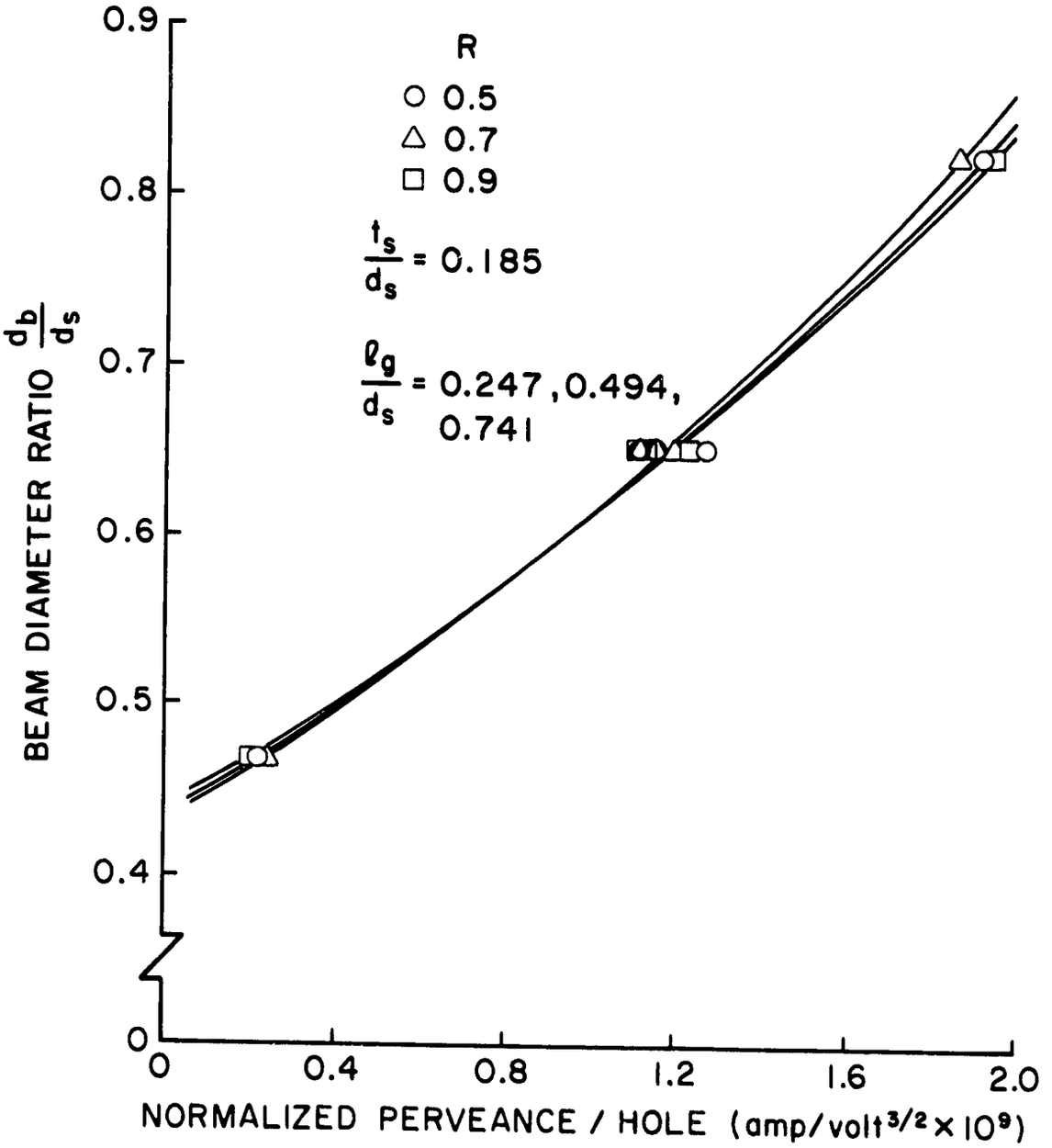

EFFECTS OF PERVEANCE AND NET-TO-TOTAL ACCELERATION VOLTAGE RATIO ON BEAMLET DIAMETER - MULTIAPERTURE GRIDS

FIGURE 34

different net-to-total accelerating voltage ratios used is minimal and the curves fall on essentially the same line. Also, the perveance values producing a given beam diameter are considerably lower for the multiaperture case. In both cases variation of the parameter $\frac{\ell_g}{d_s}$ resulted in minimal scattering of the data.

Conclusions

The computer solutions obtained by Kaufman for half angle variation agree qualitatively with experimental results. Minimum half angles predicted by the computer solutions also agree with those observed experimentally although the perveances at which these minima occur do not agree. For all the grid geometries studied--both single and multiple hole--the minimum half angle occurs consistently around a normalized perveance of 1×10^{-9} amp/volt$^{3/2}$. The magnitude of the minimum half angle of an ion beam is reduced primarily as a result of increases in the grid separation distance. The maximum obtainable preveance is increased primarily by increases in the acceleration aperture diameter to values near that of the screen grid. Reduction in screen grid thickness tend to broaden the perveance range over which the beam half angle is a minimum down to the point where the screen thickness is about 0.12 times the screen aperture diameter.

Charge exchange ion production within the ion beam makes absolute determination of the beam half angle difficult. A better understanding of the distribution of the charge exchange ion population needs to be ascertained from further experimental investigation in this area.

VISUAL OBSERVATIONS OF THE INTERIOR OF AN OPERATING HOLLOW CATHODE

The hollow cathodes used in ion thruster applications consist of a tantalum tube capped by a thoriated tungsten plate perforated by a single small hole at the tube centerline. The mechanism by which this device supplies electrons to sustain an arc discharge when mercury is flowing through it is not well understood. Previous studies have shown however that a plasma does exist within the tube[20] and this suggests processes within the tube, which are not generally observable, play a significant roll in cathode operation. In order to facilitate observation of the interior of an operating cathode and hence observe phenomena that could lead to an understanding of cathode operations a 6.4 mm dia. hollow cathode was equipped with a quartz window and tested in a vacuum bell jar facility.

Apparatus

The apparatus used in this study and shown schematically in Figure 35 consists of a 6.4 mm dia. hollow cathode supplied with an orifice plate having a 0.4 mm dia. orifice and fitted with a 1.6 mm thick by 1.27 cm diameter quartz window. Through this window the interior face of the orifice plate can be observed and photographed. The mercury flow rate through the cathode orifice was regulated by controlling the current to a standard SERT II vaporizer. The keeper was a wire loop positioned 1.5 mm from the cathode tip and the anode was a 3 cm diameter cylinder made from perforated stainless steel sheet metal. The cathode assembly was equipped with a tickler electrode to facilitate startup. The cathode itself was

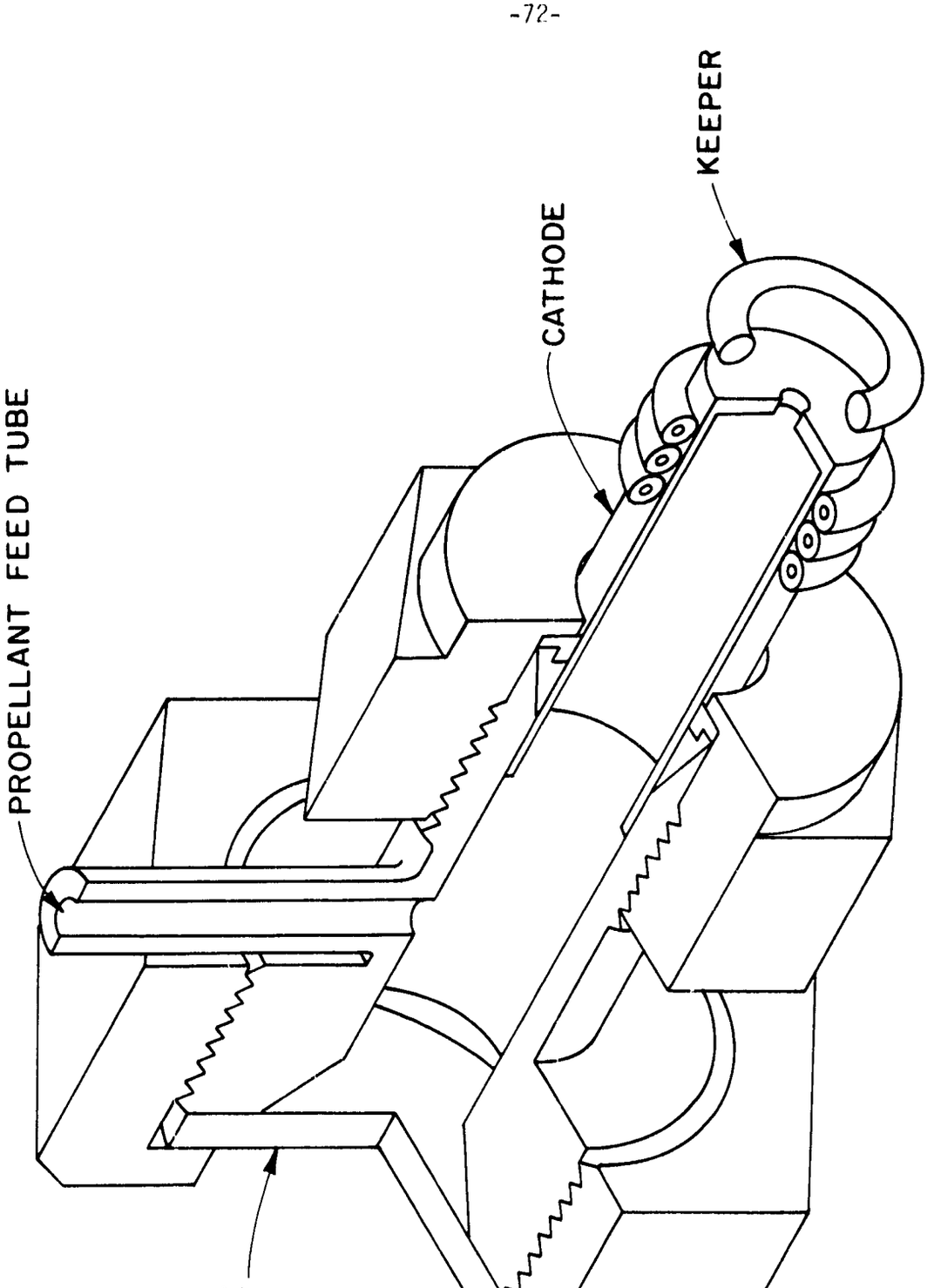

CATHODE SUPPORT AND VIEWING STRUCTURE

FIGURE 35

bare (no insert) and the interior surfaces were free of irregularities visible to the naked eye. The temperature at various locations on the interior face of the orifice plate was measured using an optical pyrometer.

Emissive Material Depletion

Low work function oxides, generally in the form of Chemical R-500*, are used inside a hollow cathode to facilitate startup and subsequent operation at acceptably low temperatures. There is evidence that this material may become depleted particularly if the cathode is operated at the high temperatures encountered at high arc current operating conditions. The phenomenological changes which accompany depletion are of interest and were observed in the following test.

A new cathode with no insert was treated with a very small amount of R-500 (diluted tenfold before being added by a damp fibre dobber through the opening left when the window was removed). This cathode was then operated for about 135 hours at a high arc current (7A) and the interior orifice plate face was photographed and surveyed with an optical pyrometer periodically to determine changes in its condition. Review of these data suggested the initial R-500 loading had been insufficient and had depleted after a few minutes of operation. A larger amount of R-500 was then added (undiluted from a damp fibre dobber). This addition caused a dramatic change in cathode operating parameters followed by a gradual return (over a 24 hour period) to those conditions existing before the final R-500 addition.

The effect of R-500 addition and depletion on cathode operating

* J. T. Baker Chemical Co., Phillipsburg, New Jersey.

parameters and cathode appearance is shown in Figure 36 and its accompanying captions. The captions show for example that the new cathode shown in the first column of photographs (probably without significant R-500 but with thorium present in an undisturbed state) operates at an interior orifice plate temperature of 1370°C to 1200°C at an arc voltage of 17v and a keeper voltage of 11v (the temperature range given is that observed from the edge of the orifice itself to the outer edge of the orifice plate). After the 135 hour operating period R-500 was added and the temperature dropped to 1190°C to 1090°C, the arc and keeper voltages to 11v and 4v respectively and the cathode appeared as shown in the second column. After another 24 hour operating period and R-500 depletion the temperature rose to 1520°C to 1500°C, the arc and keeper voltages rose to 40v and 14v respectively and the cathode appeared as shown in the third column. These final conditions and the cathode appearance were similar to those observed just before the R-500 was added (after the 135 hour operating period). The photographs were obtained through a red #29 wratten filter and a 1% neutral density wratten filter using Ektachrome EX-135 film. The photographs can be interpreted if one considers the strong spectral lines of the elements present and the transmissivity of the filters at the wave lengths of these lines. The strong spectral lines listed in Table IV were determined by viewing the discharge through a hand spectroscope, and it was found that the depleted cathode showed only the mercury lines while the treated cathode showed the additional lines characteristic of the barium that is an active ingredient of chemical R-500. A review of Table IV suggests the red filter should pass no significant radiation from the mercury. The red photographs should however show the location of excited barium neutrals and of course

Figure 36

Photographs* of the Interior of an Operating Hollow Cathode

Conditions Pertaining to Photographs

Cathode State	New Cathode (less than 1 hour of operation - R500 trace present)	Rejuvenated Cathode (R500 added after 135 hours of Operation)	Depleted Cathode (24 hours after R500 addition - 159 hours total operation)
Filter	#29 Red	#29 Red	#29 Red
Lens Opening	f22	f22	f22
Shutter Speed	1/60 sec	1/30 sec	1/125 sec
Arc Voltage	17v	11v	40v
Arc Current	7A	7A	7A
Keeper Voltage	11v	4v	14v
Temp Variation	1300°C to 1200°C	1190°C to 1090°C	1520°C to 1500°C
Filter	1" Neut. Density	1" Neut. Density	1" Neut. Density
Lens Opening	f5.6	f16	f11
Shutter Speed	1/30 sec	1/30 sec	1/30 sec
Arc Voltage	17v	11v	40v
Arc Current	7A	7A	7A
Keeper Voltage	11v	4v	14v
Temp Variation	1300°C to 1200°C	1190°C to 1090°C	1520°C to 1500°C

* Filters have been used in obtaining these prints to match the colors present in the original slides, as closely as possible.

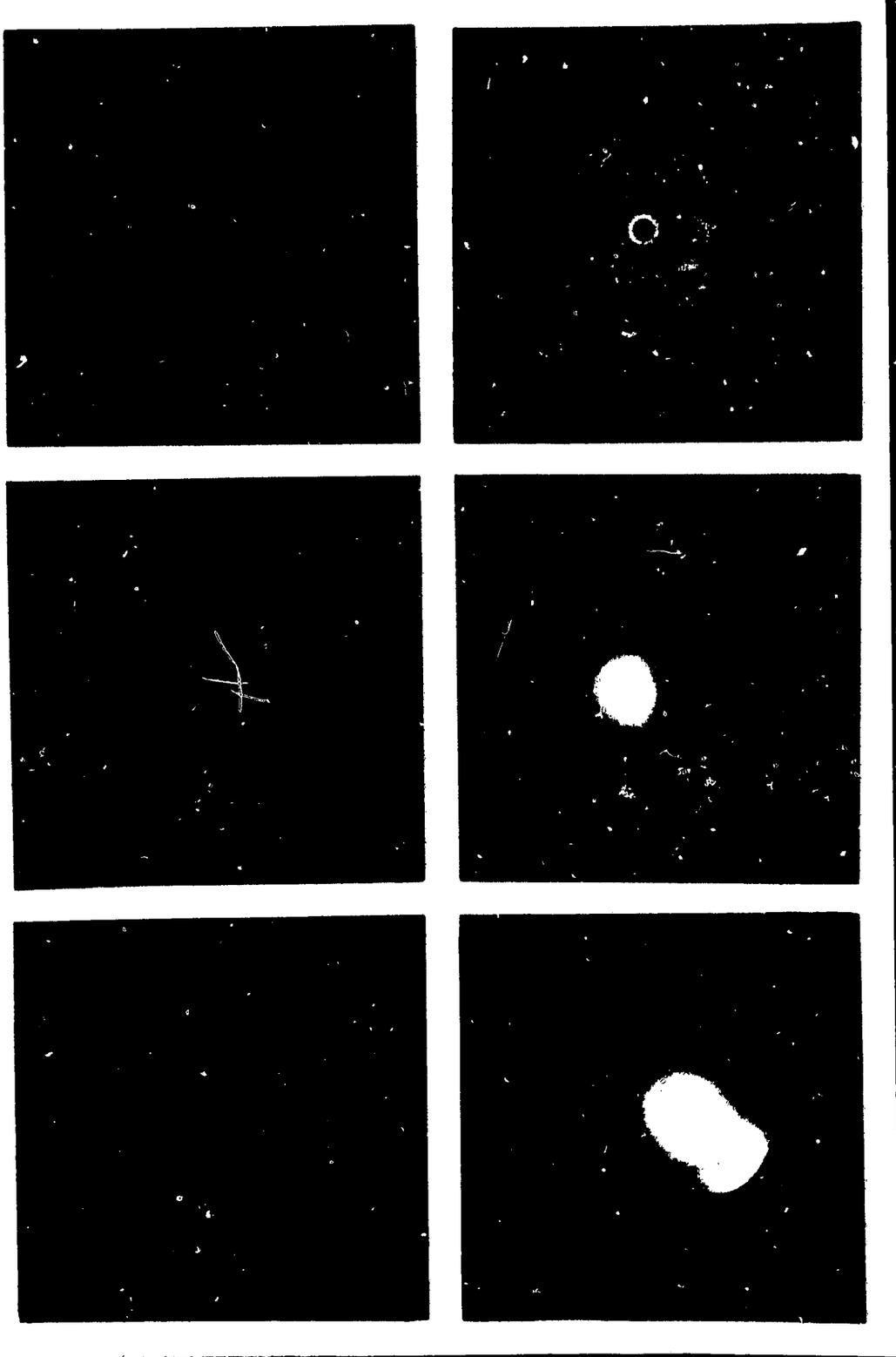

Table IV

Strong Spectral Lines for Barium and Mercury

Element	Wave lengths[21] (strong lines)	Relative Line Intensity[21]	Filter Transmissivities[22] Red #29	1% Neut. Den.
Barium	6675Å	500	89%	.9%
	6595Å	1000	88%	.9%
	6141Å	2000	10%	1.0%
Mercury	5769/5789Å	600	0%	.9%
	5460Å	2000	0%	.9%
	4797Å		0%	.8%
	4358Å	3000	0%	.6%

thermal radiation from the hot cathode surface. The neutral density filter photographs should on the other hand show the location of the excited mercury neutrals whose radiation tends to dominate in the plasma. When some barium is present it can be seen on the cathode centerline (red filter photographs 1 and 2) but when it has been depleted the orifice appears black (red filter photograph 3). The neutral density photographs show the continuum radiation from the orifice plate becoming so intense when the R-500 is depleted (column 3) that it tends to overpower the mercury radiation and show through as orange. The pattern of this orange radiation can also be seen on the original red filter photographs but it is not visible in the reproductions included here. This pattern is apparently related to a variation in surface texture of the orifice plate produced during manufacture.

These photographs suggest that barium ions are present in the cathode

region plasma when R-500 is present and this in turn would indicate barium migration takes place during cathode operation. An additional verification of barium migration was observed during the first few minutes of cathode operation after R-500 addition. Initially, intensely radiating spots were observed through a red filter at locations where the R-500 was added. Some of these spots appear in the second red photograph of Figure 36 for example. After about 20 minutes of cathode operation these spots had disappeared and the orifice plate appeared to radiate quite uniformly through a red filter.

Effect of Arc Current Variations

At one point during the photographic study of an operating cathode the arc power supply current output was oscillating between $\sim$ 0.5A to 2A on a period of about a minute. Observation of the interior orifice plate surface through a red filter during this time showed that the entire orifice plate heated up when the arc current was high and then when the current suddenly dropped to one half ampere the radiation persisted for a period of about the thermal time constant before it decayed. The shape of the radiation patterns and the nature of their decay with time is suggested in the following sketch where early patterns (solid lines) and later patterns (dotted lines) are identified. This observation leads one to the

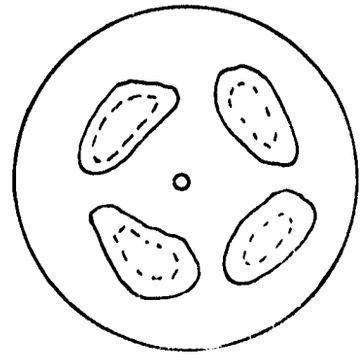

conclusion that the entire interior orifice plate participates in the emission process rather than some small localized spot such as the orifice region.

Cathode Emission Mechanisms

The Richardson-Dushman equation, which can be used to calculate thermionic electron emission from a surface, has generally yielded electron emission current densities based on measured external orifice plate temperatures that are too low to explain measured cathode emission currents. If one uses the internal orifice plate temperatures measured in this test series for an R-500 treated cathode (1100°C to 1200°C), a work function typical of a barium on tungsten surface (1.6 eV) and a Richardson equation coefficient of 0.015 x 10^6 A/m^2°K^2 the calculated emission current density is found to be 3.8 x 10^4 to 11 x 10^4 A/m^2. Since the entire orifice plate was suggested in the preceding section as participating in the emission process it is logical to use the interior surface area of the orifice plate as the emitting area and this leads to an emission current of 1.2 to 3.4A. Since the cathode was operating at 7A this model again appears to be inadequate. A second experiment performed with an internal heated emitter provides however a clue to the source of additional current. This test demonstrated that a heated emitter within a 6.4 mm dia. cathode could effect an arc current to an external anode which was two to three times the emission current of the emitter when the emitter was held at cathode potential. This two to three fold amplification of the emission current suggests the calculated thermionic emission current would be amplified to an arc current level of 2.4 to 10.6A. This calculated

current level does bracket the measured 7A current and this suggests the emission mechanism in a hollow cathode involves thermionic emission coupled with a plasma amplification effect. As barium depletion occurs and the plate temperature rises to 1500°C to 1600°C this model suggests the surface work function would have to increase to about 2 eV to effect the 7A arc current assuming the thoriated tungsten Richardson coefficient of 0.04×10^6 $A/m^2(°K)^2$. This is reasonably close to the 2.7 eV work function of thoriated tungsten.

COLD CATHODE STARTUP TESTS

Cathodes which can be started reliably from cold conditions should facilitate a reduction in the propellant loss during startup. A preliminary study of means of achieving mercury hollow cathode startup from temperatures below 100°C was therefore conducted. The methods used to approach this task are described and tests conducted with 6.35 and 3.2 mm cathodes are detailed in this section. Cathode starting performance using internal and external electrodes and flow variation was determined. Ranges of cathode starting parameters are discussed using these configurations.

General Approaches to Cathode Starting

There are several methods that are available for initiating cathode operation. Briefly, the basic methods are:

1. Lower the work function: This approach is generally accomplished by materials selection. Low work function materials are provided on the surfaces of the cathode or impregnated in pores within the cathode components to insure the availability of this active material throughout the desired life of the cathode.

2. Increase the voltage stress: There are several alternatives to this approach. Shaping and positioning of the electrodes can significantly increase the voltage stresses. Movable electrodes can also be used. Increasing the applied voltage to existing electrodes as well as introducing high voltage pulses on auxiliary (or tickler) electrodes have been used. High frequency alternating potentials can also be applied.

3. Decrease the breakdown potential: Higher cathode flow rates or mechanical obstruction of the normal flow serves to decrease the breakdown potential by increasing the gas pressure in the propellant flow field.

4. Increase the temperature: For the purposes of these tests the cathode was to be cold, but it was assumed under this ground rule that small metal emitters that could be heated rapidly to emissive temperatures at low power levels would be acceptable.

Apparatus and Procedure

A 6.35 mm diameter hollow cathode having a 1 mm diameter orifice was modified to facilitate evaluation of several of the approaches described above. Figure 37 is a cutaway sketch of the first of the configurations tested. The emitter coil and spike axial anode were operated as a diode pair at various bias conditions and both electrodes were also operated and biased independently. Figure 38 is a cutaway of the second configuration tested. The axial, 0.25 mm diameter, 10 mm long tungsten emitter was operated using the co-axial cathode wall as the anode. As both of the figures suggest the cathodes were mounted on a fitting containing a quartz window to allow viewing the internal cathode surfaces and electrodes during testing. No insert was used but an R-500 coating was applied to the inside face of the orifice plate. An external keeper was used with both of these configurations as was a tickler electrode on which a 12 kv potential spike could be applied. These configurations allowed preliminary testing of a large number of startup concepts without altering the cathode emission surfaces as a result of exposure to air.

The general test procedure required stabilization of the flow rate (vaporizer temperature) while keeping all cathode hardware above the condensation temperature of mercury. This could be quite accurately accomplished by eliminating visible condensation from the internal cathode and window surfaces. The keeper potential was set at 400 volts and if an

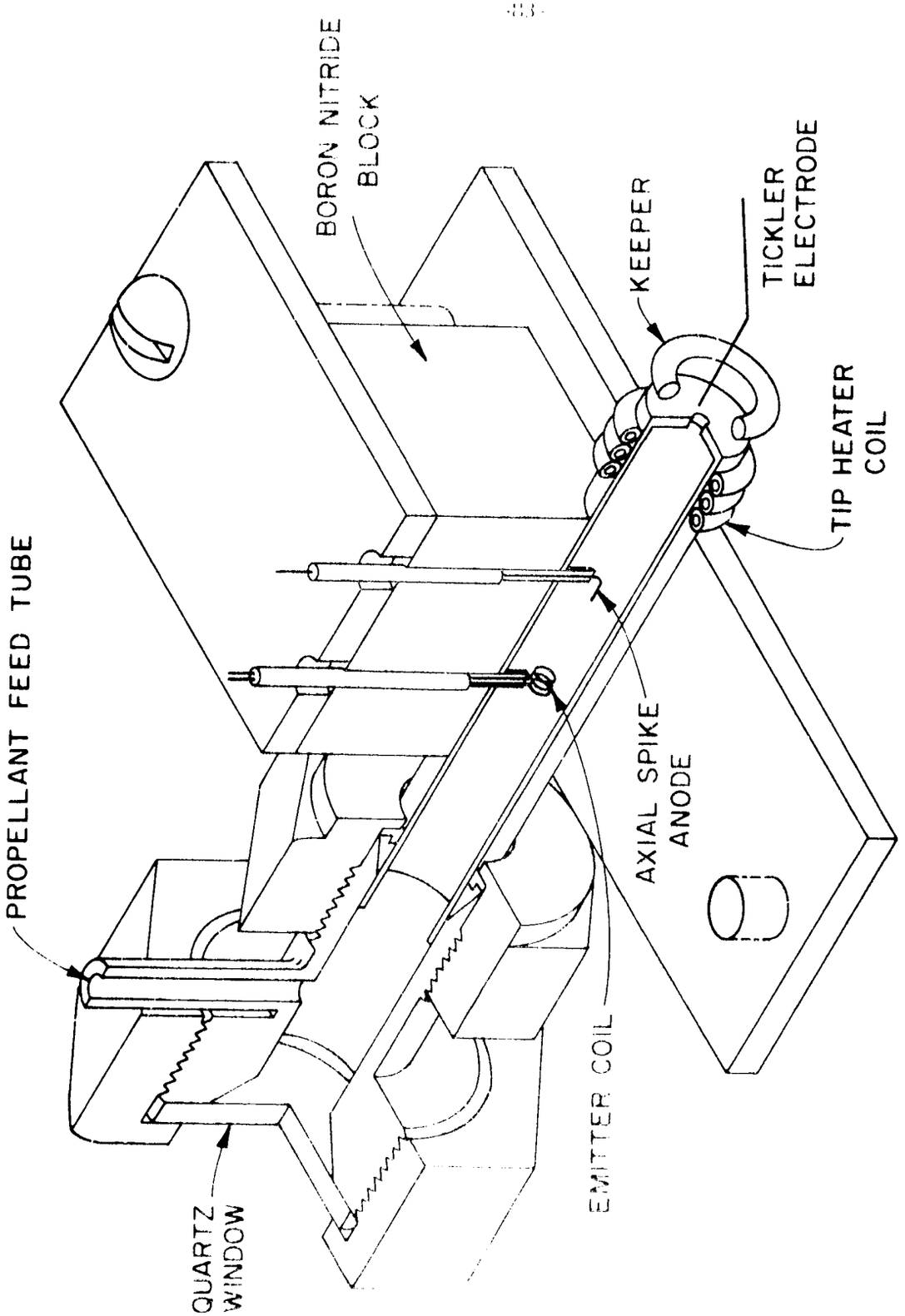
BORON NITRIDE
BLOCK
KEEPER
TICKLER
ELECTRODE
TIP HEATER
COIL
PROPELLANT FEED TUBE
AXIAL SPIKE
ANODE
EMITTER COIL
QUARTZ
WINDOW

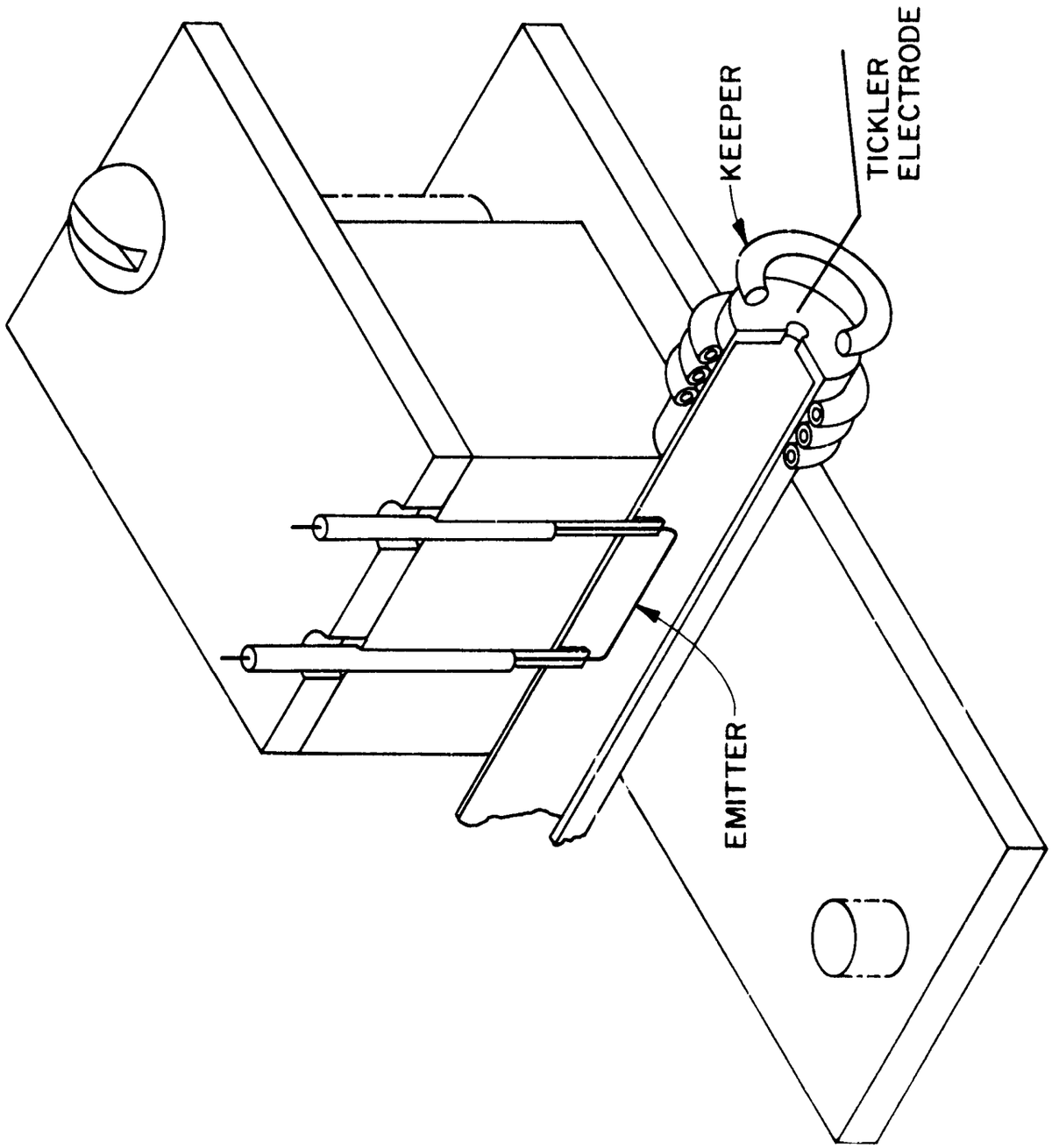

COLD CATHODE STARTUP TEST CONFIGURATION

FIGURE 33

internal emitter was used it was set at a power level that provided one amp internal emission. Cathode starting tests were then conducted, and a tentative best starting technique was selected by making comparisons of the results.

Final tests were then performed on the enclosed keeper 3.2 mm dia. cathode assembly shown in Figure 39. This configuration allowed testing of the tickler concept and an axially inserted internal electron emitter. Since the primary interest of the program was the 3.2 mm enclosed keeper cathode, tests conducted both the 6.35 mm and 3.2 mm dia. cathodes covered the 187 to 4 mA flow rate range considered typical of the 3.2 mm cathode.

Results and Discussion

The tests on the configuration shown in Figure 37 were brief and consistent. Biasing the internal spike anode positive with respect to the cathode resulted in immediate vaporization of the anode. Using this anode as an internal tickler resulted in rapid starts followed by the need for spike anode replacement. The emitter coil produced diode operation when heated and biased negative with respect to the cathode wall and startups were achieved. Operation of the internal emitter was sporadic, however, with either very low current, high voltage (90V) discharges or heavy discharges at under 10 volts occurring. The coils of this emitter were very difficult to center with respect to the cathode wall and this is considered to be the probable cause of the inconsistent results.

The configuration shown in Figure 38 gave excellent starting characteristics during the initial test and it was selected as the internal arrangement for the primary series of tests. The preliminary tests had shown that reliable starts could readily be [illegible] both the internal axial

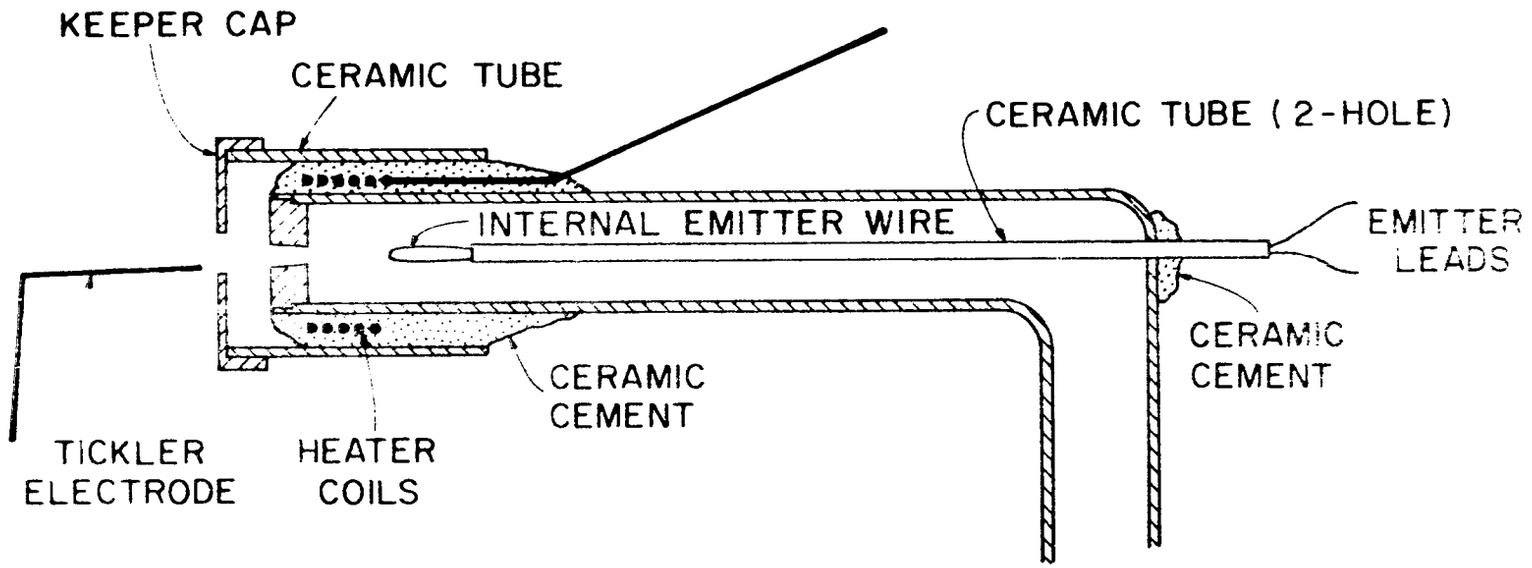
KEEPER CAP
CERAMIC TUBE
CERAMIC TUBE (2-HOLE)
INTERNAL EMITTER WIRE
EMITTER LEADS
CERAMIC CEMENT
CERAMIC CEMENT
TICKLER ELECTRODE
HEATER COILS

emitter and the external tickler at cathode flow rates greater than 200 mA, and it was therefore decided that the most meaningful comparisons of these startup techniques would be obtained at flow rates below this value.

The tests were begun by establishing the desired flow rate and then raising the cathode temperature above the propellant condensation limit. This limit was found to be at indicated temperatures ranging from 135 to 160°C. This band was inferred by observing droplet disappearance and vacuum system pressure surges which occurred when the vaporization temperature was reached. Tests conducted with non-condensable propellents showed that room temperature (~20°C) starts could be achieved routinely, but temperatures above the condensation limit were required before startup could be achieved with mercury.

When the internal emitter was used for startup, emitter heater power was switched on to the preset value to start the cathode. After the keeper discharge lit (rarely longer than the time constant for emission from the internal cathode) the emitter heater power was shut off. At cathode flow rates less than 200 mA the cathode was self-extinguishing at keeper currents in the neighborhood of 0.2A without internal emission. After extinction, startup was reinitiated immediately and these cycles were continued as the tip temperature slowly rose from 150°C to 250°C. At 250°C starting cycles were terminated until the tip temperature had cooled to 150°C and the starting cycles were then repeated. These startup tests were conducted for flow rates of 147, 140, 95, 45, 30, 10 and 4 mA equivalent. At all of the flow rates the cathode started every time the internal emitter was turned on if the emission level was at least one amp.

The effect of tip heater power was briefly investigated at flow rates below 10 mA. At tip temperatures above 1000°C operation could be sustained

occasionally but the discharge was not stable without internal emission. Figure 40A shows the variation of keeper potential with internal emission for several flow rates when the internal emitter was biased 10 volts negative. As the flow rate was decreased, the internal emission required to maintain the keeper voltage at acceptably low values increased. Each flow rate has a distinct minimum keeper voltage (horizontal asymptote) at a given internal bias. Figure 40B shows the effect of internal emission on keeper voltage for 10 and 30 volts internal bias at the lowest flow rate tested (4 mA). The keeper voltage decrease with changing internal bias was greatest at the low flow rate and was hardly noticeable at higher flow rates. In all cases, starting was critically dependent on sufficient internal emission. Although at least one amp internal emission was required to start the keeper discharge, operation of the cathode could be sustained at any flow rate tested at an internal emission of 150 mA.

The capacity of the keeper power supply is, of course, critical to startup under many cathode conditions. The 400 volt starting potential was low enough that cathode ignition would not occur reliably using the tickler electrode at flow rates below about 30 mA. This condition existed because there was not enough energy stored in the circuit to sustain the discharge. Keeper potentials of 800 to 1200 volts were sufficient however to maintain operation using a tickler start at all of the flow rates investigated.

Two other interesting effects were observed during the starting tests. 1) During high temperature operation, barium apparently migrated to the non-operating internal emitter. This was postulated from the next emitter start attempt which was invariably an "instant on" but with rapidly decreasing emission at a very low emitter power level. 2) Near the mercury

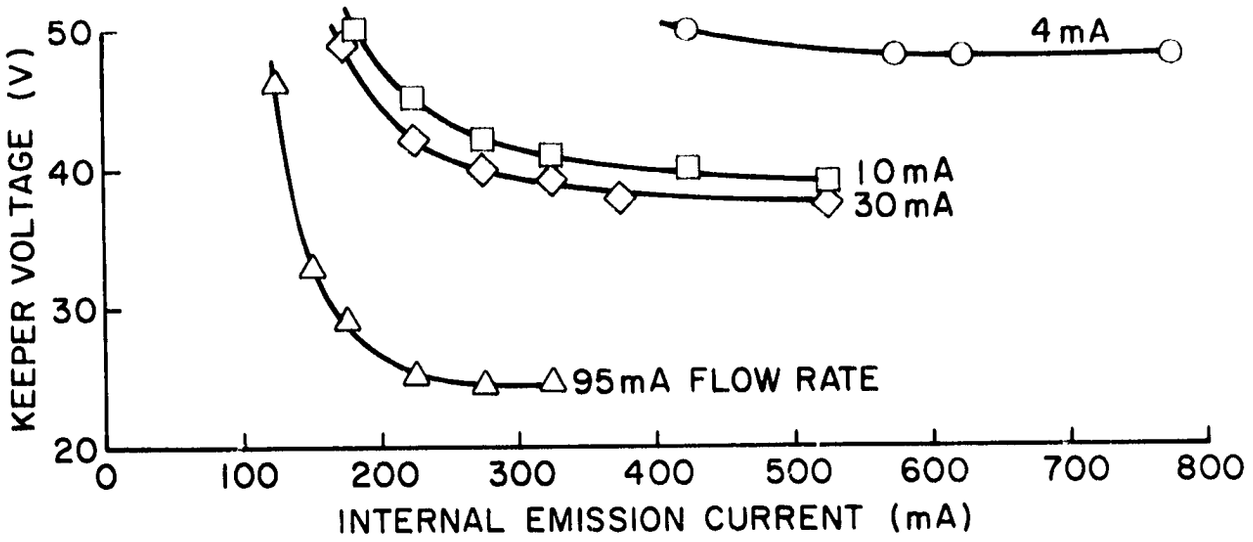

A. AT 10 V INTERNAL BIAS.

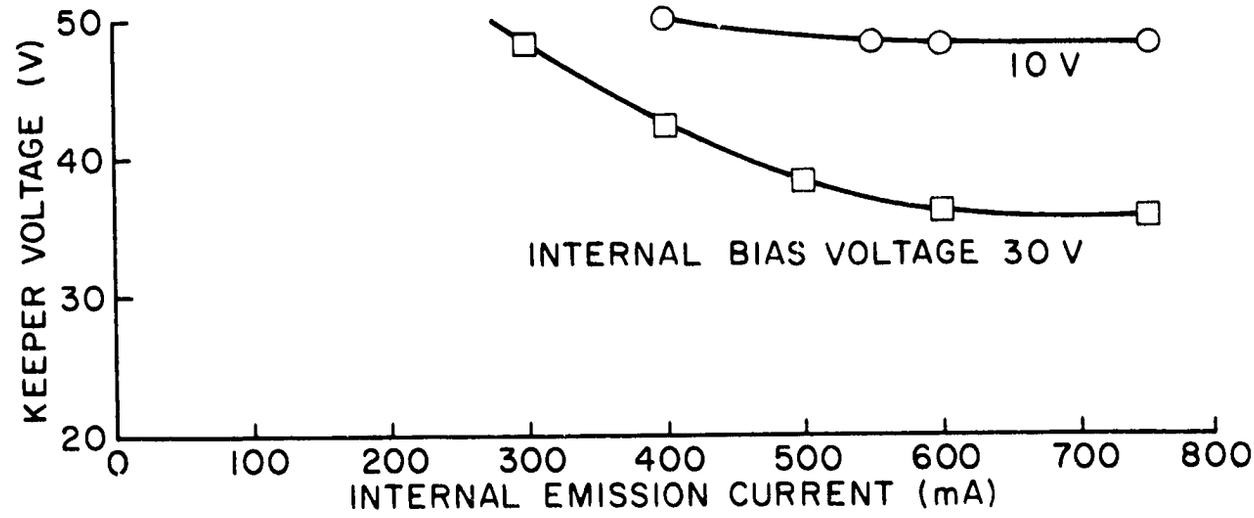

B. AT 4 mA FLOW RATE

EFFECTS OF INTERNAL EMISSION ON KEEPER VOLTAGE

FIGURE 40

condensation limit, the internal emitter, due to its low mass and lesser thermal lag, collected mercury. This was postulated from the next emitter start attempt which would be an "instant on" start with a one decade pressure pulse of very short duration seen on the vacuum instrumentation.

A 3.2 mm diameter enclosed keeper cathode was also tested. The cathode was operated, as supplied, with no insert and free of emissive material. At mercury flow rates of about 100 mA and keeper potentials of 500 volts, startup from cathode temperatures just above the condensation limit were demonstrated using a 0.25 mm diameter high voltage tickler. The tickler was positioned at the edge of the keeper orifice, 1 mm downstream with the axis of the tickler wire parallel to the cathode axis. (See Figure 39). Attempts to achieve startup at lower flow rates or temperatures were generally not successful. Increasing the keeper potential above 500 volts resulted in breakdown through the aluminum oxide keeper support tube. The 3.2 mm cathode support elbow was modified to allow the introduction of an internal emitter as shown in Figure 39. The axial tube mounting method was required because of the small bore of this cathode. Because of the closely-spaced geometry, the alumina emitter supports fused during each run. Operation could not be sustained for sufficient periods to allow data to be taken. Additional operation with the 3.2 mm cathode and internal emitter was abandoned. The engineering difficulty associated with implementing the emitter in this size cathode was beyond the scope of the present effort.

Lifetime Observations

Although extended life tests were not included in this effort, the cycling capabilities of the internal emitter were of sufficient interest

to log the number of starts. After the preliminary tests were conducted and the procedures described previously were established, a new internal emitter was installed for the remainder of the tests. The emitter was used to make repeated cathode starts during the periods when the flow rates were being stabilized and measured. During the course of this program a single emitter accumulated 5100 starts. Failure of the emitter occurred during a Monday morning startup at a power level 1/4 to 1/3 of the normal operating power. None of the characteristics of the 0.25 mm diameter tungsten emitter had been observed to change prior to this failure. The primary significance of the cycle testing is that an unoptimized, first-try configuration achieved over 5000 cycles when operated in a vacuum system that was shut down every night over the ten day period of the tests.

Conclusions

Cathode starts can be achieved at temperature levels down to the condensation temperature of the mercury propellant prevailing at hollow cathode pressures (135 to 160°C). The most successful means of starting a 6.35 mm diameter cathode was through the use of an internal 0.25 mm diameter, 10 mm long tungsten emitter which was biased negative with respect to the cathode wall. Successful starting and operation was achieved at propellant flow rates down to 4 mA equivalent.

An external high voltage (12 kV) tickler was the next best starting method for this cathode and the only method that worked successfully in the 3.2 mm diameter cathode. Below a 30 mA flow rate limit, higher keeper potentials were required to sustain a tickler initiated start.

ION THRUSTER HOLLOW CATHODE PLASMA CHARACTERISTICS

The plasma inside an operating 0.32 cm diameter hollow cathode has been probed by Fearn, Philip and Pye.[20] In order to verify their results and also to determine if the probe used in their study altered the characteristics of the plasma in their rather small cathode a similar test was conducted under this grant using a larger diameter cathode. A 0.63 cm diameter cathode having a 0.38 mm diameter orifice was outfitted with a stationary Langmuir probe located on the cathode axis in the manner suggested by Figure 41. The cathode itself was supported by a structure provided by a quartz window in the manner suggested by Figure 35. The interior side of the cathode orifice plate was coated with chemical R-500 for the test, but no insert was installed within the cathode.

The Langmuir probe was 0.13 mm in diameter and 0.46 cm long and was made of tungsten wire. It was biased using a battery circuit and the bias voltage and probe current (sensed across a 100Ω resistor) were fed to an X-Y recorder. Langmuir probe data were analyzed using least squares exponential curve fits to the data in both the electron decelerating and accelerating voltage regions of the probe traces. A thin sheath analysis was used in spite of the fact that the sheath thickness may be comparable to the probe diameter at some operating conditions. This assumption while it may introduce as much as two-fold error in electron density should not affect electron temperature or plasma potential significantly.

Results

As data were collected and the time the probe had been exposed to the plasma increased the probe characteristics were observed to change presumably

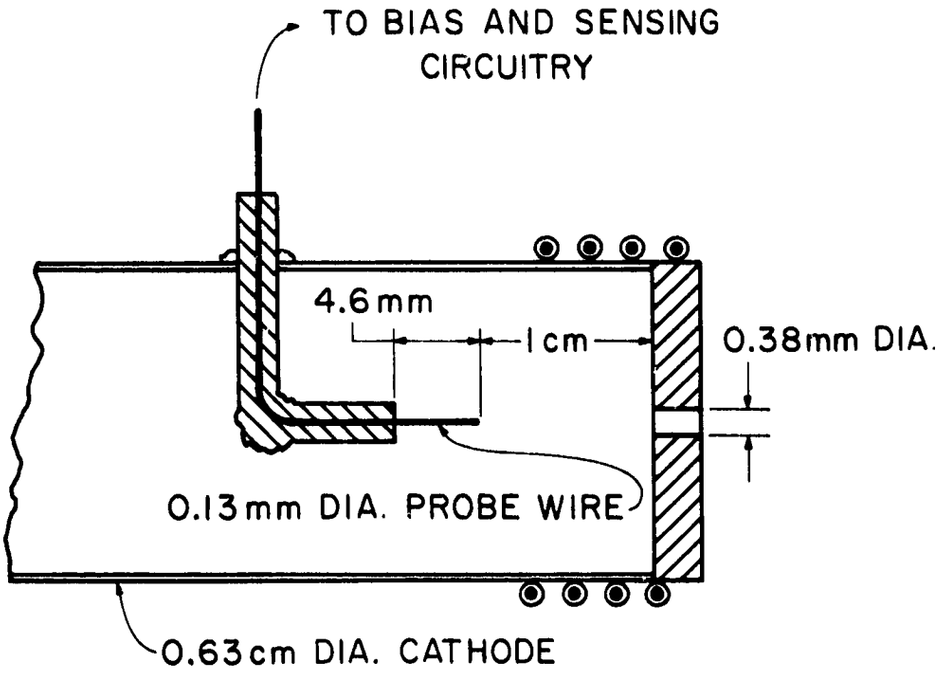

CATHODE LANGMUIR PROBE

FIGURE 41

because of probe contamination. Attempts to clean the probe by biasing it to either +45V or -45V using a battery were not successful although the probe was observed to be heated to incandescence by electron bombardment when it was biased +45V. This contamination appeared to occur more rapidly as arc current was increased and was presumably caused by constituents of the R-500 mix which was present. The contamination problems prevented extended operation of the cathode and accurate determination of mercury flow rates but some data could be collected before contamination became severe. Figure 42 shows for example the variations in plasma properties with arc current determined from Langmuir probe traces before contamination became significant for an approximate mercury flow rate of 100 mA. The magnitude of the electron densities and temperatures are observed to be in good agreement with those measured by Fearn et al.[20] The trends shown are considered qualitatively correct.

Conclusions

In view of the fact that essentially identical plasma properties have been measured in both 3.2 mm and 6.4 mm dia. cathodes it is concluded that the Debye shielding distance in an operating hollow cathode is sufficiently small to facilitate the collection of meaningful Langmuir probe data. Probe contamination due possibly to the constituents in the emissive mix present can introduce significant errors into the measurements. The plasma potential, electron temperature and electron density within a hollow cathode lie typically in the range of 4V, 0.5eV and $10^{10}cm^{-3}$ respectively.

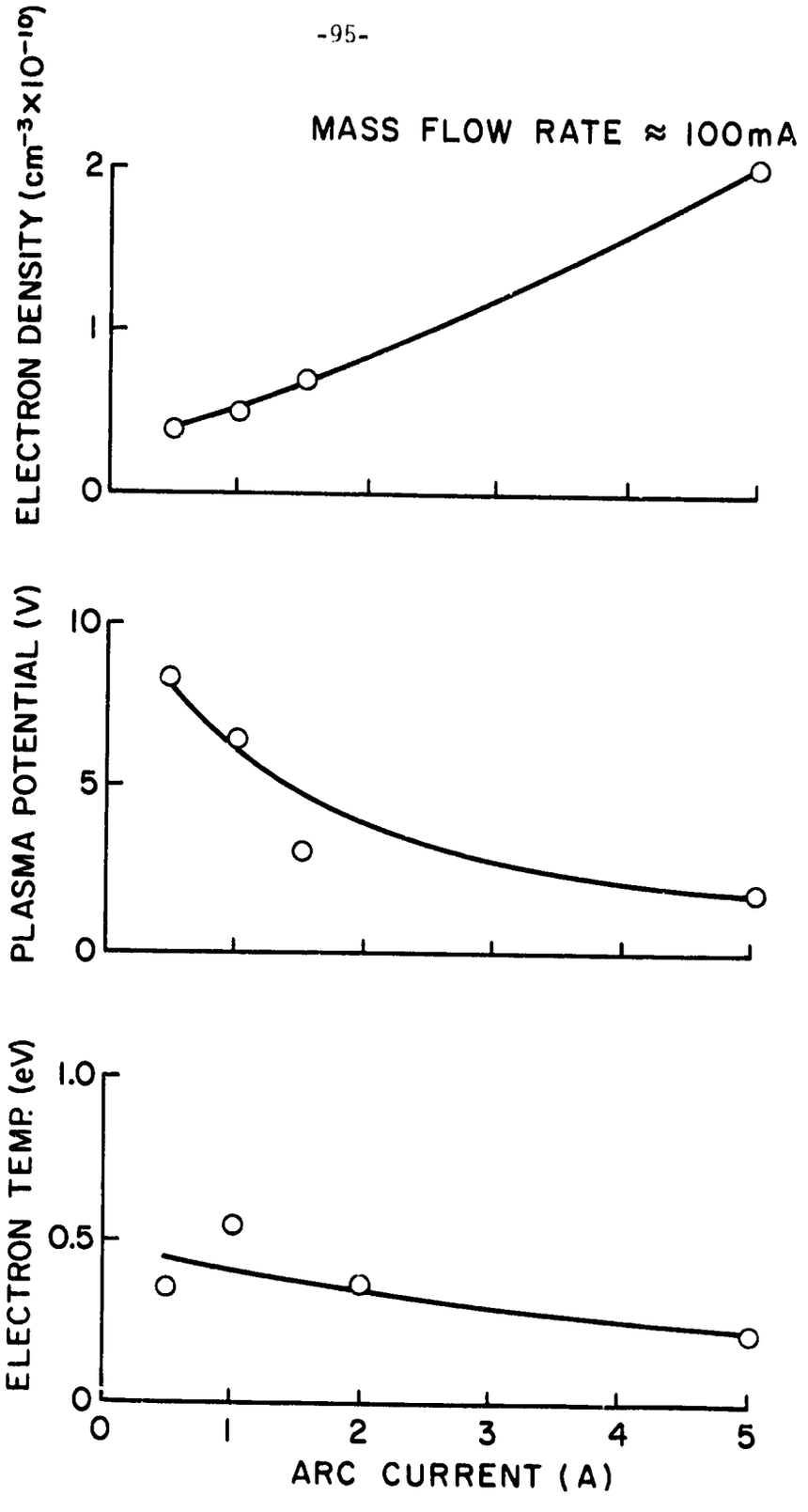

CATHODE INTERIOR PLASMA PROPERTIES

FIGURE 42

HOLLOW CATHODE STEPPED ORIFICE STUDY

It has been postulated that electron emission occurs as a result of a surface emission mechanism on the interior of an ion thruster hollow cathode operated on mercury; that the emission current density has a constant value in the range 20 to 50 A/cm^2; and that the emission occurs in the vicinity of the cathode orifice.[20] As emission current is increased then this mechanism simply requires an increase in the emitting surface area. Fearn, Philip and Pye[20] conducted an experiment utilizing a cathode orifice that was stepped to a larger diameter part way through the orifice plate. They found this step introduced a corresponding transition in the emission current/voltage characteristic of the cathode. In order to verify this experiment and to observe visually the existence and motion of this emitting surface as arc current is increased a similar experiment was conducted. A cathode having the two step orifice configuration shown in Figure 43 was constructed and installed on a fixture containing a quartz window in the manner suggested in Figure 35. The cathode interior was not provided with a cathode insert but was coated with R500.

Results

Figure 44 presents plots of arc current vs. arc voltage obtained in a stepped orifice cathode operating at three different mass flow rates. The data were obtained by slowly increasing the voltage applied to the anode and plotting the output on an X-Y recorder. Each set of data was collected at a keeper current of 0.2A. The arrow at the end of each curve indicate the tendency of curve when the voltage at the final point shown was reached. For the higher flow rate data shown on Figure 44 the discharge underwent a transition to a low voltage and high current value at the value of the voltage

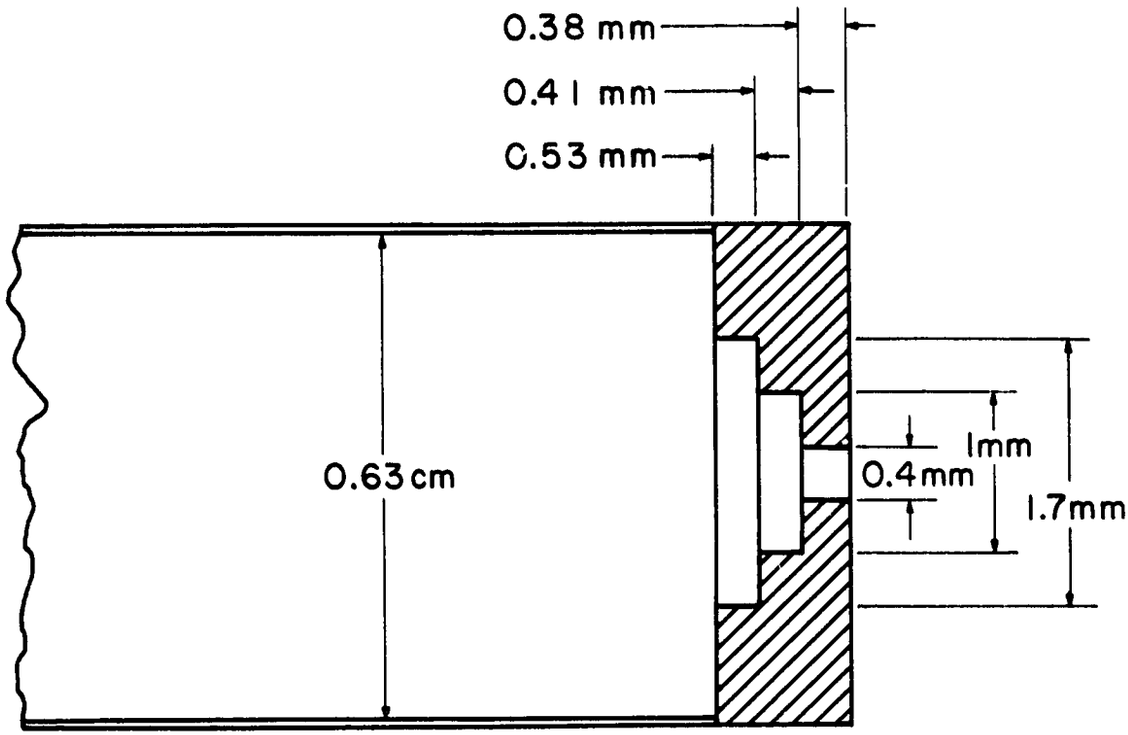

STEPPED ORIFICE CATHODE

FIGURE 43

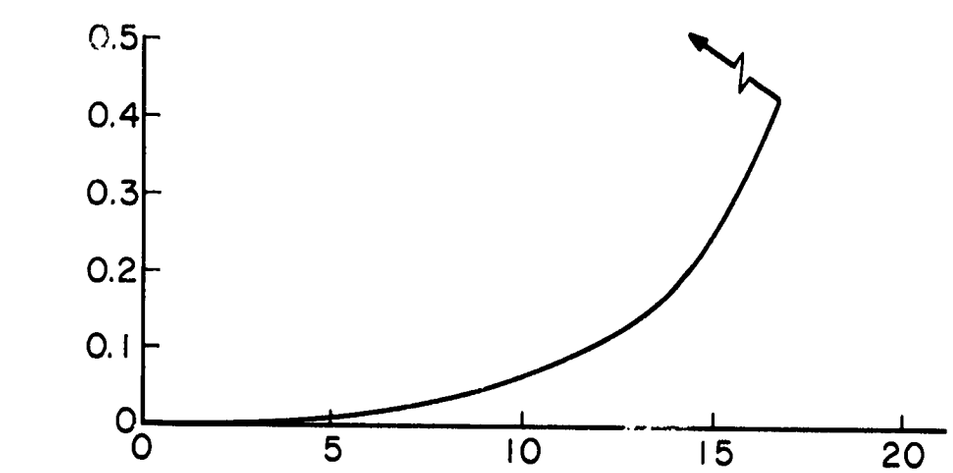

A. HIGH FLOW RATE (250 mA)

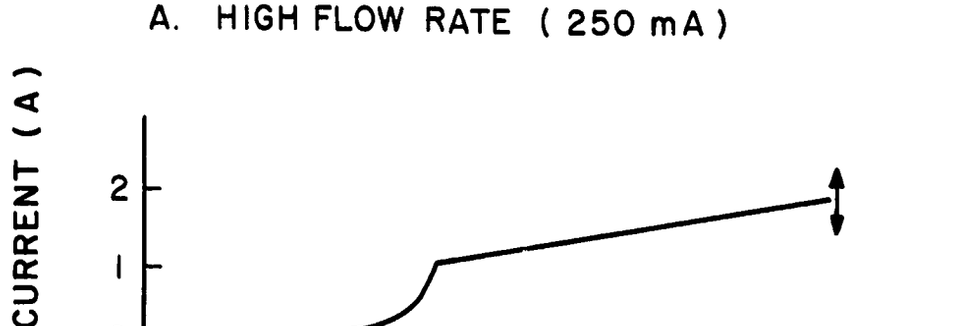

B. INTERMEDIATE FLOW RATE (77 mA)

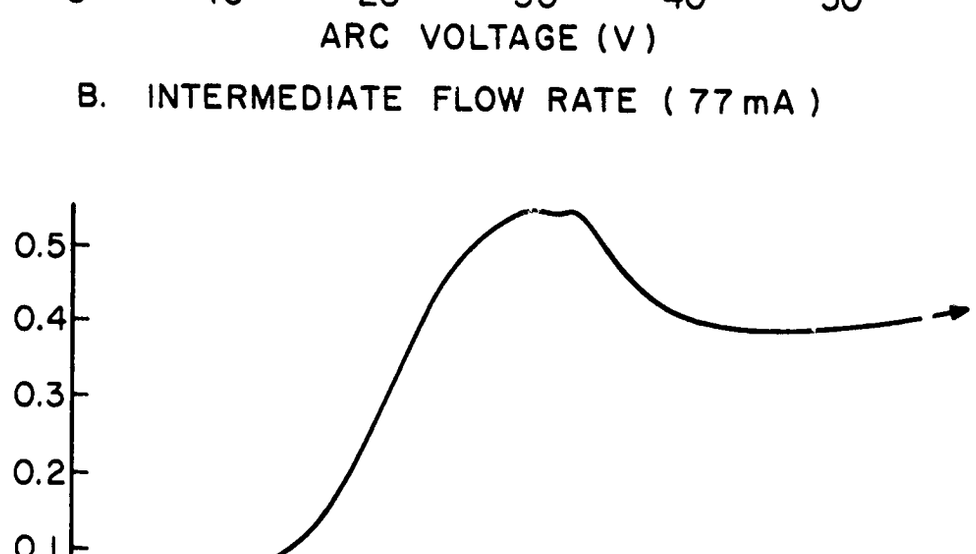

C. LOW FLOW RATE (23 mA)

STEPPED ORIFICE CATHODE ARC CURRENT/VOLTAGE CHARACTERISTICS

FIGURE 44

and current being determined by the current limiting characteristic of the arc power supply. At the intermediate flow (Figure 44B) the arrow indicates the occurrence of an oscillation with a character again determined by the power supply. At the low flow rate (Figure 44C) the arc current continued to increase gradually with increases in arc voltage. The break in the curve of Figure 44B and the peak arc current condition of Figure 44C were characterized by a transition in the external discharge. At voltages above these values the plasma was observed to radiate throughout the bell jar whereas at lower voltages the plasma was observed only in the region between the anode and cathode. The data of Figure 44 show no evidence of any transition in the emission current voltage characteristics that might be associated with movement of an emitting surface to the geometrical steps in the orifice.

Observation of the plasma within the hollow cathode through red and neutral density filters indicated the intensity of radiation from the plasma increased with arc current, but there was no evidence of an emitting surface that increased in area over the cathode orifice region as arc current was increased.

Conclusion

Arc voltage/current characteristics and visual observations of the interior of an operating stepped orifice cathode do not support the theory of a constant current density emitting surface which exhibits an increase in area as arc current is increased.

APPENDIX A

SINGLE AND DOUBLE ION BEAM CURRENT DETERMINATION

John R. Beattie

Nomenclature

A_o = grid viewing area ($\theta = 0$), m^2

A_p = probe aperture area, m^2

A_θ = grid viewing area ($\theta \neq 0$), m^2

$f(\theta)$ = correction factor

$i(r,\theta)$ = probe current, A

$I(r)$ = current crossing measurement plane, A

$j(r)$ = current density at grids, Am^{-2}

$J(R,\theta)$ = current density at measurement plane, Am^{-2}

L = distance from grids to measurement plane, m

r = radial coordinate measured from beam centerline, m

r_g = grid radius, m

R = radial coordinate measured from center of circular viewing area, m

θ = probe pitch angle, ^{o}

= dispersion angle, ^{o}

θ_{max} = positive dispersion angle, ^{o}

θ_{min} = negative dispersion angle, ^{o}

ϕ = probe acceptance half-angle, ^{o}

Introduction

The determination of the single and double ion beam currents requires viewing a point on the grids from several different angles since the ions leaving the accelerator system follow trajectories which are not parallel. That is, the single and double ion dispersion profiles must be determined as a function of the thruster radius and this can be accomplished by the use of an articulating $\vec{E} \times \vec{B}$ momentum analyzer.[2] This appendix presents the derivation of the equations which are used to transform the momentum analyzer output into integrated single and double ion beam current components.

Beam Current Equations

The $\vec{E} \times \vec{B}$ momentum analyzer probe is used to measure the current leaving a small area of the grids as a function of the dispersion angle θ. The probe is pointed at a fixed area of the grids at different angles and the current due to ions leaving this area at each of the angles is detected by the probe. When the probe is positioned at $\theta = 0$ the viewing area is circular as illustrated in Figure A1-B. With the probe at any other angle θ the viewing area is elliptical as indicated in Figure A1-C. To account for the associated area change the current density at the analyzer plane is weighted by a factor $f(\theta)$ which is equal to the ratio of the circular to elliptical areas. For simplicity in the derivation which follows, the probe entrance aperture plane is assumed to remain a fixed distance L from the plane of the grids as illustrated in Figure A1-A.

The ion current density at the measurement plane $J(R,\theta)$ is calculated from the probe current $i(r,\theta)$ and the probe aperture area A_p

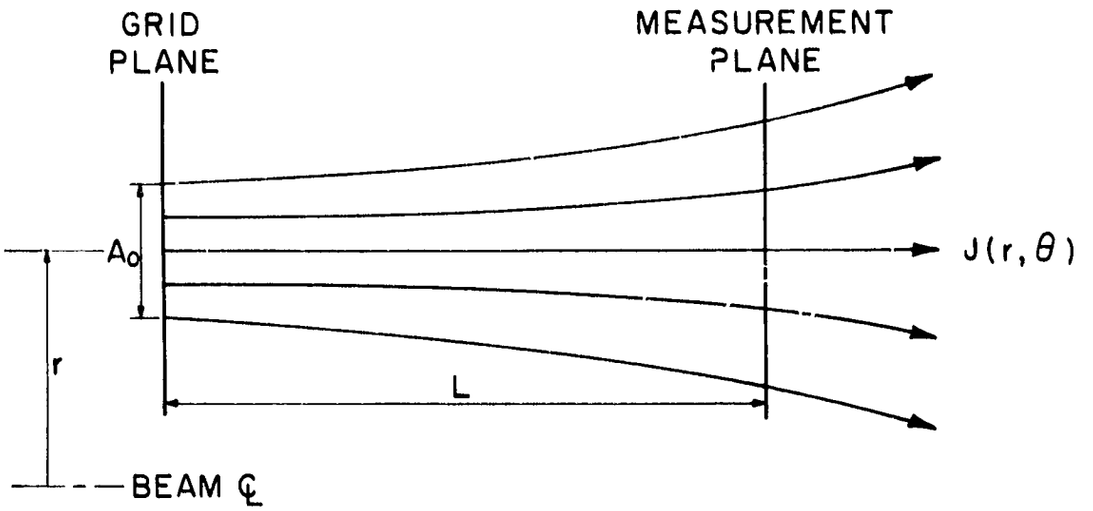

A. ION TRAJECTORIES

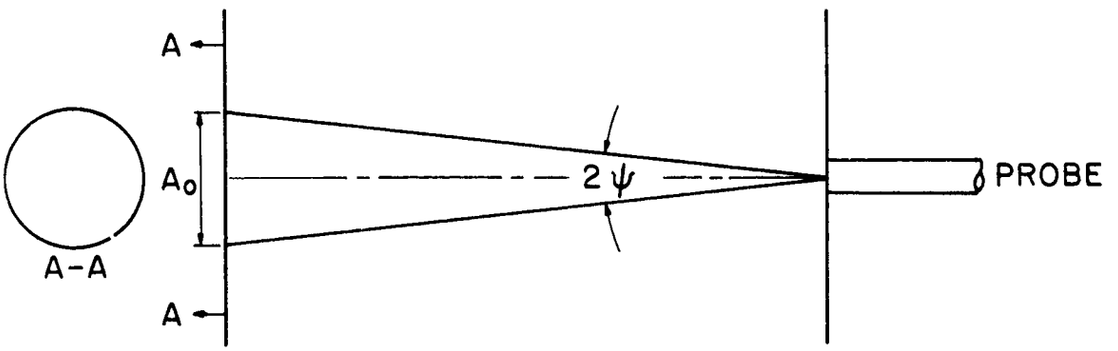

B. VIEWING AREA, $\theta = 0$

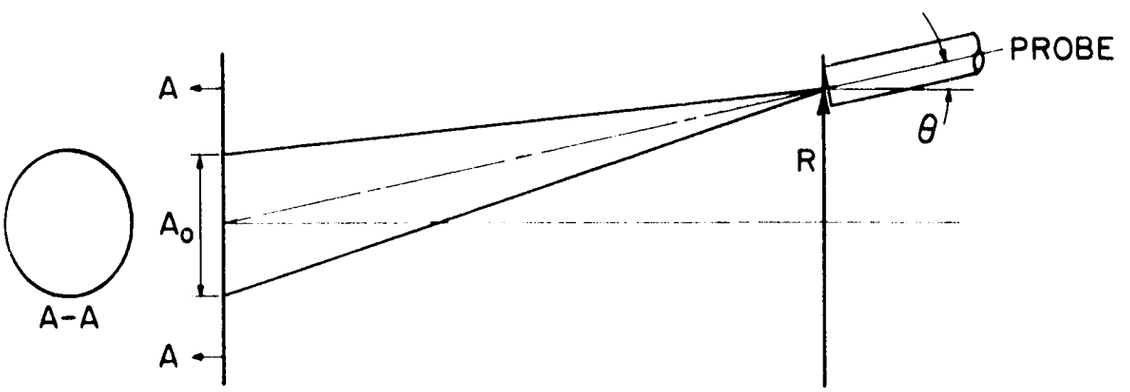

C. VIEWING AREA, $\theta \neq 0$

$\vec{E} \times \vec{B}$ PROBE ARRANGLMENT

FIGURE A1

by the relationship

$$J(R,\theta) = \frac{i(r,\theta)f(\theta)}{A_p} \tag{A1}$$

The current crossing the measurement plane as a result of ion injection from a circular region on the grids at a radius r is obtained by integrating this current density over the signal area at the measurement plane

$$\begin{aligned} I(r) &= \int \vec{J}(R,\theta) \cdot \vec{n} dA \\ &= \int J(R,\theta) \cos\theta \, dA \end{aligned} \tag{A2}$$

where

$$dA = 2\pi R dR \ .$$

From Figure A1 we see

$$R = L \tan\theta$$

and

$$dA = 2\pi L^2 \sec^2\theta |\tan\theta| d\theta \ . \tag{A3}$$

Since the dispersion profiles are generally not symmetrical about $\theta = 0$, the integration is carried from $\theta = \theta_{min}$ to $\theta = \theta_{max}$ and the result is divided by two to obtain the current I(r).

The ion current density at the grids is obtained by dividing the current crossing the measurement plane by the area from which the current left. That is,

$$j(r) = I(r)/A_0 \tag{A4}$$

The ion current can be obtained by integrating the current density over the grid area by use of the expression

$$I_B = \int_o^{r_g} 2\pi r j(r) dr \qquad (A5)$$

where r_g is the grid radius. Implicit in Equation A5 is the assumption of azimuthal symmetry. Combining equations A1, A2, A3, A4, and A5 gives the integral equation for the beam current

$$I_B = \frac{2\pi^2 L^2}{A_p A_o} \int_o^{r_g} \int_{\theta_{min}}^{\theta_{max}} ri(r,\theta) f(\theta) |\sin \theta| \sec^2 \theta \, d\theta dr \qquad (A6)$$

The function $f(\theta)$ can be derived by use of Figures A1 and A2. The circular viewing area A_o is given by

$$A_o = \pi L^2 \tan^2 \psi \quad . \qquad (A7)$$

The elliptical area A_θ is

$$A_\theta = \frac{\pi L^2 \tan \psi \left[\tan (\theta + \psi) - \tan (\theta - \psi)\right]}{2 \cos \left\{\sin^{-1} \left[\frac{\tan (\theta+\psi) + \tan (\theta-\psi)}{2}\right]\right\}} \quad . \qquad (A8)$$

Equation A8 can be simplified by use of the following approximate relation which introduces an error of less than 1% for dispersion angles less than about 25^o

$$A_\theta \doteq \frac{\pi L^2 \tan \psi \left[\tan (\theta+\psi) - \tan (\theta-\psi)\right]}{2 \cos \theta} \quad . \qquad (A9)$$

The correction $f(\theta)$ is obtained by combining Equations A7 and A9 to give

$$f(\theta) = A_o / A_\theta$$

$$\doteq \frac{2 \cos \theta \tan \psi}{\tan (\theta+\psi) - \tan (\theta-\psi)} \quad . \qquad (A10)$$

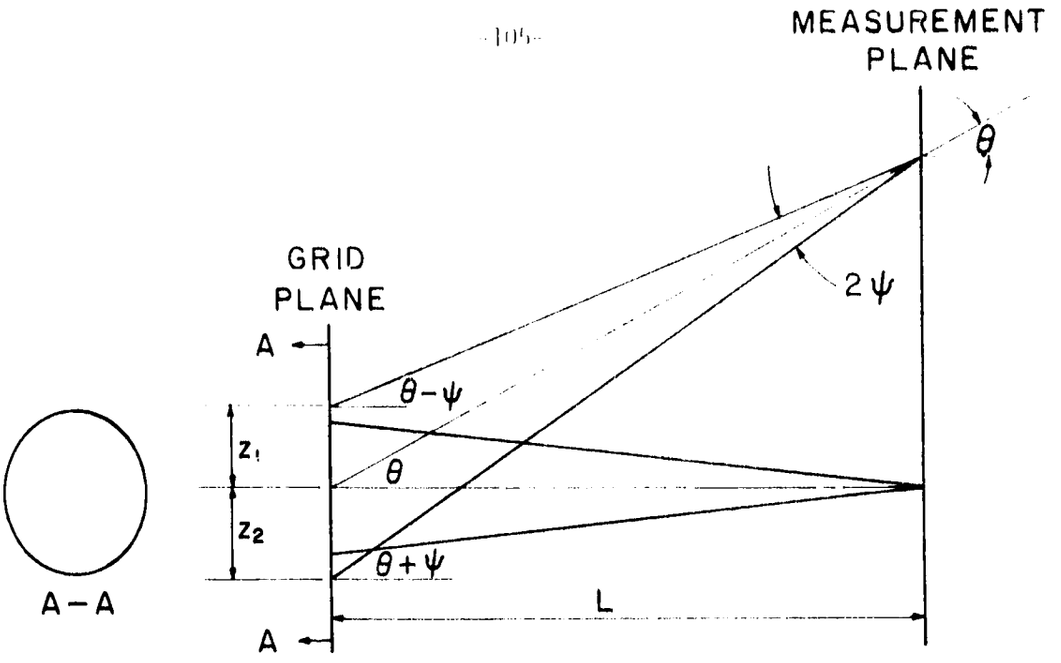

$$z_1 = L \tan\theta - L \tan(\theta - \psi)$$

$$z_2 = L \tan(\theta + \psi) - L \tan\theta$$

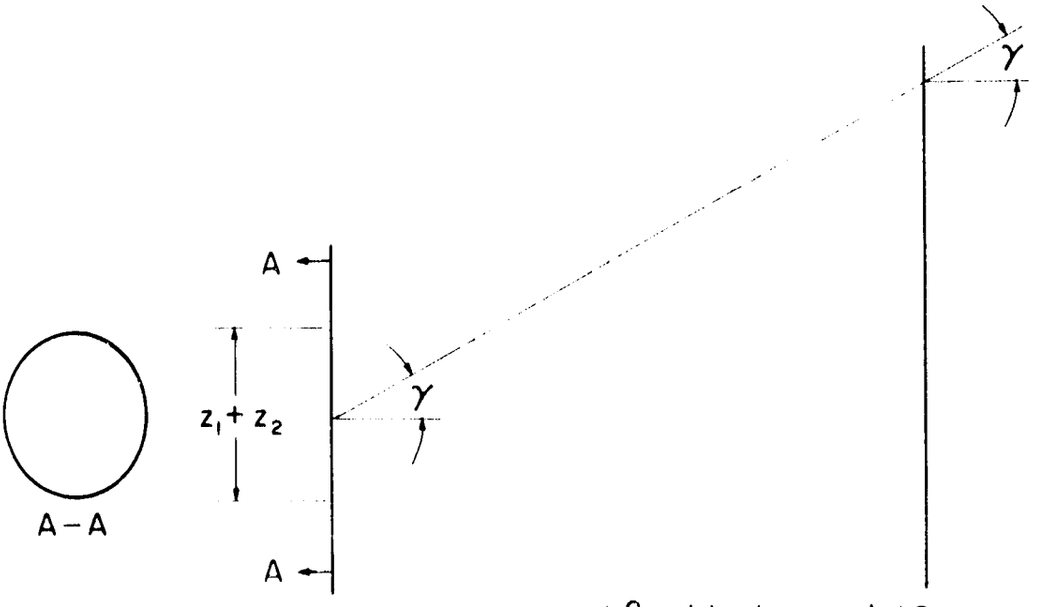

$$\sin\gamma = \frac{L \tan(\theta - \psi) + (z_1 + z_2)/2}{L}$$

$$= \frac{\tan(\theta + \psi) + \tan(\theta - \psi)}{2}$$

ELLIPTICAL VIEWING AREA GEOMETRY

FIGURE A.7

Data Acquisition and Reduction Technique

Analyzer probe current data $i(r,\theta)$ were obtained in the following manner. The analyzer plate voltage was adjusted to allow detection of the desired ion current component. The probe pitch angle θ was set to within 0.05° of the desired value with a stepper motor and the probe was swept vertically through the ion beam from $r = -r_g$ to $r = r_g$ by means of a motorized drive assembly. The output of a linear potentiometer was used to monitor the vertical position of the probe and this signal along with the analyzer output was recorded on an X - Y plotter. The probe pitch angle was then increased by a 5° increment and the procedure repeated. Since the beam is assumed axisymmetric, the probe angle can always be of the same sign and the positive or negative dispersion angles are determined by $r > 0$ or $r < 0$. This reduces the number of off-axis probe pitch angles by one half which reduces the data acquisition considerably.

Data reduction consists of digitizing the plotted data for input to a digital computer program which performs the double integration of Equation A6 by numerical means first for the doubly charged ion data and then for the singly charged ion data. The ratio of these two currents is then the double-to-single ion current ratio. Ion dispersion profiles are also determined using Equation A1 for the single and double ion data.

APPENDIX B

LANGMUIR PROBE ANALYSIS

John R. Beattie

The Langmuir probe data presented in this report were analyzed by the numerical procedure of Reference [10]. These results generally indicate higher Maxwellian electron temperatures and lower primary to Maxwellian electron density ratios than earlier results which were obtained by graphical methods.[23] The purpose of this appendix is to explain these discrepancies and to point out the large errors the graphical procedure can introduce when the electron temperature is greater than about 4eV.

In the retarding field portion of the Langmuir probe trace the two-group plasma assumption predicts the following current-voltage relationship[10]

$$I = B_1 + B_2 V + B_3 \exp(B_4 V) \tag{B1}$$

where I is the probe electron current, V the probe voltage, and the constants B_i are determined by the plasma properties. Introducing these properties, the expression above can be rewritten in the following nondimensional form

$$\frac{I}{I_{sat}} = \frac{n_p}{n_m}\sqrt{\frac{\pi}{4T_m \epsilon_p}}\,(\epsilon_p - \phi_p + V) + \exp\left(\frac{V - \phi_p}{T_m}\right) \tag{B2}$$

where n_p and n_m are the primary and Maxwellian electron densities, ϵ_p and T_m the primary electron energy and Maxwellian electron temperature, ϕ_p the plasma potential, and I_{sat} the Maxwellian electron saturation current. Representative values of the properties n_p/n_m,

ε_p, and ϕ_p are presented in Table B1 for a mercury electron-bombardment thruster. Using these values, Equation B2 was used to calculate

TABLE B1. ASSUMED PLASMA PROPERTIES

Property	Assumed Value
n_p/n_m	5%
ε_p	30eV
ϕ_p	40V

dimensionless current as a function of probe voltage for various electron temperatures. The results are presented in Figure B1 which indicates the variation of total and primary electron current with probe voltage for three values of the Maxwellian electron temperature. Figure B1-A corresponds to a fairly low electron temperature of 2eV and we see the primary and total current lines are tangent (i.e., the Maxwellian current is very small) over a large voltage range. Graphical analysis of these data should therefore yield good results. Figure B1-B is for an electron temperature of 6eV and we see at this higher temperature the two curves are never tangent. Analysis of these data by the graphical technique would result in erroneous plasma properties since the method requires the primary current line to be tangent to the total current line. To estimate the amount of error one might expect, the dashed curve labeled A-A in Figure B1-B was drawn tangent to the total current line in such a manner as to give the correct primary electron energy. Analysis of these data using the line A-A as the primary current resulted in errors in the primary

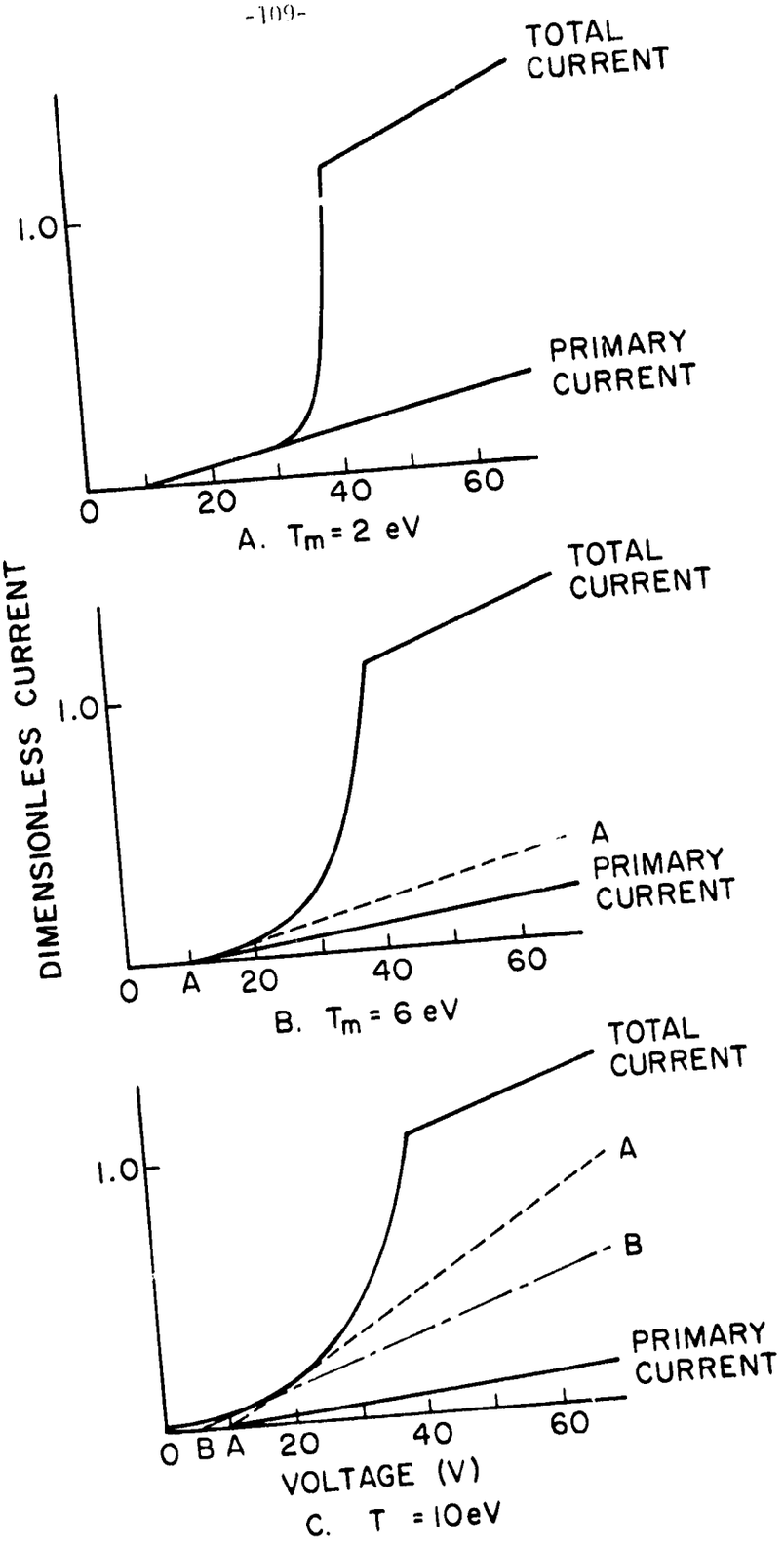

ANALYTICALLY GENERATED LANGMUIR PROBE TRACES

FIGURE 61

electron number density, Maxwellian electron temperature and density of 160%, 20%, and 1%, respectively. Figure B1-C indicates how the problem becomes even more severe when the electron temperature is increased to 10 eV. The line labeled A-A in this figure is drawn tangent to the total current curve and gives the correct primary electron energy. However, in the accelerating field region of the trace the slope of line A-A is greater than the slope of the total current curve--a condition which is not reasonable physically. In order to obtain a realistic solution in the accelerating field region and still satisfy the tangency condition, a primary current line such a B-B might be used but this also introduces an error in the primary electron energy. Graphical analysis of Figure B1-C using the line B-B as the primary electron current resulted in errors in the primary electron energy and density, and Maxwellian electron temperature and density of 13%, 307%, 35%, and 9%, respectively.

The numerical procedure [10] for analyzing Langmuir probe data does not impose the tangency condition of the graphical method and, as a result, does not introduce the large errors described above. For comparison purposes the total current curves of Figure B1 were digitized and analyzed by the numerical procedure. The plasma properties determined in this manner were found to be in error by less than 15% in the worst case.

The curves of Figure B1 indicate the graphical procedure will introduce significant errors in the plasma properties when the Maxwellian electron temperature is greater than about 4eV. The error introduced will in general result in higher primary electron densities and lower Maxwellian electron temperatures than the true values.

REFERENCES

1. Kerslake, W. R., et al, "SERT II: Mission, Thruster Performance, and In-Flight Thrust Measurements," Journal of Spacecraft and Rockets, Vol. 8, No. 3, March 1971, pp 213-224.

2. Vahrenkamp, R. P., "Measurement of Double Charged Ions in the Beam of a 30-cm Mercury Bombardment Thruster," AIAA Paper No. 73-1057, October 31 - November 2, 1973.

3. Peters, R. R. and P. J. Wilbur, "Double Ion Production in Mercury Thrusters," AIAA Paper 75-398, March 19-21, 1975.

4. Kieffer, L. J., "Electron Impact Ionization Cross Section Data for Atoms, Atomic Ions, and Diatomic Molecules," Rev. Mod. Physics, Vol. 38, No. 1, pp. 15 - 23, 1966.

5. Shpenik, O. B. and Azpesochnyi, I. P., "Excitation Cross Sections near the Threshold for Electron Atom Collisions," Optics and Spect., Vol. 23, pp. 7-10, 1967.

6. Kupriyanov, S. E. and Z. Z. Latypov, "Ionization of Positive Ions by Electrons," Soviet Physics JETP, Vol. 19, No. 3, pp. 558-559, Sept. 1964.

7. McConnel, J. C. and B. L. Moisewitsch, "Excitation of Mercury by Electrons," J. Phys. B., Vol. 1, No. 3, pp. 409-412, 1968.

8. Gryzinski, Michal, "Classical Theory of Atomic Collisions. I. Theory of Inelastic Collision," Phys. Rev., Vol. 138, No. 2A, p. A341, April 19, 1965.

9. Wilbur, P. J., "An Experimental Investigation of a Hollow Cathode Discharge," NASA CR-120847, December, 1971.

10. Beattie, J. R., "Numerical Procedure for Analyzing Langmuir Probe Data," AIAA Journal, Vol. 13, No. 7, July 1975, pp. 950-952.

11. Wilbur, P. J., "15 cm Diameter Ion Thruster Research," NASA CR-134755, December, 1974.

12. Beattie, J. R., and P. J. Wilbur, "15 cm Cusped Magnetic Field Mercury Ion Thruster Research," AIAA Paper No. 75-429, March 19-21, 1975.

13. Knauer, W., R. L. Poeschel, and J. W. Ward, "Radial Field Kaufman Thruster," Journal of Spacecraft and Rockets, Vol. 7, No. 3, March 1970, pp. 248-251.

14. Kaufman, H. R., "Experimental Investigations of Argon and Xenon Ion Sources," NASA CR-134845, June, 1975.

15. Wilbur, P. J., "Experimental Investigation of a Throttlable 15 cm Hollow Cathode Ion Thruster," NASA CR-121038, December, 1972.

16. Kaufman, Harold R., "Ion-Thruster Propellant Utilization," NASA TN D-6591, December, 1971.

17. Kaufman, Harold R., "Accelerator-System Solutions for Electron-Bombardment Ion Sources," AIAA Paper 75-430, March 19-21, 1975.

18. Masek, T. D., "Plasma Properties and Performance of Mercury Ion Thrusters," AIAA Paper No. 69-256, March 3-5, 1969.

19. Kaufman, Harold, "Charge-Exchange Plasma Generated by an Ion Thruster, NASA CR-134844, June 1975.

20. Fearn, D. G., C. M. Philip, J. W. Pye, "The Development of Hollow Cathodes, Vaporizers and Isolaters for Use in Mercury Ion Thrusters," appears in "Bericht das DGLR-Symposium Elektrische Antriebssysteme" 22/23 Juni 1971, Braunschweig, West Germany, pp. 61-83.

21. Anon., "Handbook of Chemistry and Physics," 36th Edition, pp. 2654-2658, Chemical Rubber Publishing Co., 1954-1955.

22. Anon., "Handbook of Chemistry and Physics," 36th Edition, pp. 2722-2733, Chemical Rubber Publishing Co., 1954-1955.

23. Strickfaden, W. B., and K. L. Geiler, "Probe Measurements of Discharge in an Operating Electron Bombardment Engine," AIAA Journal, Vol. 1, No. 8, August, 1963, pp. 1815-1823.